Video-Based Particle Image Velocimetry of Laboratory Rip Currents

by

Liang He and Jack A. Puleo

RESEARCH REPORT NO. CACR-06-05
December, 2006

Center for Applied Coastal Research
Ocean Engineering Laboratory
University of Delaware
Newark, DE 19716

TABLE OF CONTENTS

LIST OF TABLES

LIST OF FIGURES

ABSTRACT

Accurate field measurements of rip currents are difficult due to their evanescent characteristics. In this study, Particle Image Velocimetry (PIV) is presented to quantify the horizontal flow structure of laboratory rip currents. PIV is a whole-flow-field technique providing instantaneous velocity vector measurements in a flow cross section. It has been widely applied to hydrodynamic and aerodynamics flow field experiment visualization.

Time-domain and frequency-domain based cross-correlation algorithms are discussed and compared. A multi-grid iterative FFT-based algorithm is selected in favor of its time efficiency and robustness. Lens calibration to remove the edge distortion effect and image rectification to cast the pixel-based image into real world coordinate is conducted before the PIV processing of each image. Proposed post-processing intending to smooth out the spurious vectors is tested on synthetic images.

As the first attempt to apply PIV in laboratory generated rip currents, PIV is validated by ADV measurement using a bar-incised rip channel. The results indicate that the two measurements compare favorably. The rip current flow features can be captured by the image processing technique of PIV.

Finally, the variability of rip current dynamics is investigated by changing basin geometry and incoming wave conditions. On all three geometries with different level of rip channel incision, the rip current strength approximately increases and then decreases with increased incoming wave height (from 0.03 m to 0.05 m to 0.07m) as the wave field is the predominant driving force of rips. As the rip channel is incised from

1/3 to 2/3 and further down to full channel, the rip current feedback system roughly changes from positive to negative. These above complex trends are shown in the spatial distribution of both mean and maximum offshore velocity. Vorticity and shear rate field are also investigated taking advantage of PIV's dense measurements.

Chapter 1

INTRODUCTION

Since Shepard [1936] first separated the concept of rip currents from undertow, their generation mechanism, flow patterns and internal structure have triggered significant scientific interest. Defined as a narrow, agitated and often sediment-laden current heading offshore, rip currents not only contribute to ever-changing near-shore bathymetry, but pose danger to beach goers. Additionally, because of their intrinsic complexity and evanescent characteristics, much effort and a variety of approaches have been employed to investigate them. Theoretical studies have exploited dynamic behaviors within rip channels such as the presence of highly unsteady eddies, strong vorticity and wave-current interaction [Noda, 1974; Chen *et al.*, 1999; Yu and Slinn, 2003]. Rip currents have also been investigated by using numerical models such as the Quasi-3D circulation model SHORECIRC [Haas and Svendsen, 2000; Haller *et al.*, 2002] with reasonable agreement between prediction and measurements. Field experiments have shown that rip currents can persist as long as several weeks or months and can have energy variations and pulsations on very low frequency time scales [MacMahan *et al.,* 2004]. Furthermore, laboratory experiments for investigating rip current flow features have been undertaken [Haller and Dalrymple, 2001; Kennedy and Dalrymple, 2001; Haas and Svendsen, 2002; Haller *et al.*, 2002], demonstrating that the presence of a gap in otherwise alongshore uniform sand bar dominates the nearshore circulation.

Field and laboratory data suggest that rip current strength increases with increasing wave energy and decreasing water depth [MacMahan *et al.*, 2005]. The maximum mean current is present in the surf zone, where the maximum forcing occurs due to the dissipation of waves [MacMahan *et al.*, 2005]. In most of the earlier field and

laboratory studies, instruments were fixed at limited positions leading to a sparse representation of the velocity field. To overcome some of these resolution issues, Schmidt *et al.* [2003] used Lagrangian Global Positioning System (GPS)-tracked drifting buoys to capture nearshore circulation and rip current motions in the field. Mean alongshore velocity obtained from drifters compared well with nearby electromagnetic current meters. They also observed eddy-like drifter paths near the confluence of the feeder current and rip current before they were transported offshore. In a laboratory effort, Kennedy and Thomas [2004] obtained rip current flow patterns over a channel-incised sand bar using particle tracking velocimetry (PTV) of surface floats. They showed the circulation to be unsteady with changes apparent at many length and time scales. When data from the Lagrangian drifters and supplementary current meters were compared, Stokes drift was found to be the major component of drifter velocity. They also pointed out that the drifter method poses difficulty in obtaining time-varying properties at given locations arising from the Lagrangian nature. Due to the limitation of the drifter recognition ability, drifters could only be distributed sparsely and the tracking technique sometimes required manual interpretation.

Limited Lagrangian measurement corresponds to PTV because it is impractical to have more than one tracer per area of interest. If smaller tracers can be dispersed on the water surface with a higher density, it is possible to obtain reliable and dense Eulerian surface flow velocities through particle image velocimetry (PIV) rather than particle tracking. Video-based PIV is a technique that analyzes fluid experiment imagery and quantifies the circulation pattern of the whole flow field with the assistance of seeding particles [Bowen, 1969; Adrian, 1991; Stevens and Coates, 1994; Willert and Gharib, 1991; Adrian, 2005]. PIV has some inherent advantages over other flow measurement alternatives including large spatial coverage, high resolution, unobtrusiveness of the flow, and a low experiment budget. PIV also has some disadvantages such as the ability to quantify only two-dimensional flow field of a

transection plane illuminated by a laser sheet or surface velocity in this study. It should be noted, however, that stereo-PIV has been performed using multiple cameras to yield three dimensional flow fields [e.g., Lawson *et al.*, 1997]. PIV is a powerful tool for diagnostic investigation of complex flow and has been widely applied to turbine, thermo-engine and channel flow in micro- and macro-scale aerodynamic and hydrodynamic flow experiments [see Adrian 2005 for a review]. In terms of nearshore currents, PIV has been used to quantify swash and surf zone flow fields on intermediate and shallow sloping beaches [Puleo *et al.,* 2003; Holland *et al.*, 2001]. Video-based PIV has recently been used to study the development of rip currents in the field [Holland *et al.,* 2004]. However, to our knowledge, PIV has not been used to investigate surface flow fields associated with laboratory-scale rip currents.

Previous observation has made it clear that the existence and relative strength of rip currents are related to the forcing provided by the incident wave field. The influence of water depth variability (due to tides and bathymetry) is slightly less direct, since it is first manifested in the waves, which in turn drive the rips. It is apparent, however, that bathymetry tends to control the location and spacing of the rips and the tidal cycle will modulate the strength of the flow [Aagaard *et al.*, 1997; Brander, 1999; Brander and Short, 2000]. Previous research on rip currents conducted in the wave basin at University of Delaware used topography, where the rip channel was incised down to background slope [Kennedy and Thomas, 2004]. Because in the field, topography is ever-changing and usually the rip channel is not this drastic, the aforementioned geometry is probably not sufficiently representative of the real world.

The purpose of this study is to investigate the potential in using PIV for quantifying surface flow patterns in laboratory-generated rip currents on a barred beach. After PIV has been validated for its ability and reliability to quantify the surface flow field, variable rip channel geometries are constructed to investigate the influence of topography on current dynamics. Chapter 2 describes the PIV technique, cross-

correlation algorithms, lens calibration, laboratory calibration and image rectification, image pre-processing, vector field post-processing and error analysis. In chapter 3, rip currents over the previously studied full channel incision are investigated and PIV data is validated with ADV data. The repeatability of PIV's ability to quantify the same processes is tested, time-averaged and other statistical properties are also calculated to verify PIV as a robust measurement technique. In chapter 4, the variability of rip current dynamics is investigated corresponding to different basin topographies, offshore flow strength in focused area within the channel under different wave and topographical conditions is compared. Vector field, shear stress and vorticity field are all addressed relative to different incident wave conditions and bathymetry. Chapter 5 gives the summary of the findings of this study.

Chapter 2

CORRELATION BASED PIV TECHNIQUE

2.1 Introduction

PIV is a whole-flow-field technique providing instantaneous velocity vector measurements in a flow cross section. It requires four basic requirements in laboratory studies: An optical transparent test section containing flow seeded with tracing particles; A light source to illuminate the region of interest (plane or volume); recording hardware consisting of a CCD camera and a computer with suitable software to process the recorded images and extract velocity information from the tracer particle positions. Normally, there are three implementations of PIV: single exposure double image (cross-correlation based), double exposure single image (auto-correlation based) and multiple exposure single image (auto-correlation based). Cross-correlation based PIV is most commonly applied and also used in present study.

In contrast to particle tracking velocimetry (PTV), which is regarded as direct descendent of flow visualization using tracer particles, correlation–based PIV does not require the matching of individual images belonging to a pair. Instead of determining the displacement of individual particles, correlation-based PIV determines the average motion of small groups of particles contained within small regions known as interrogation windows. This process of averaging over multiple particle pairs within an interrogation spot makes the technique remarkably noise tolerant and robust in comparison to PTV.

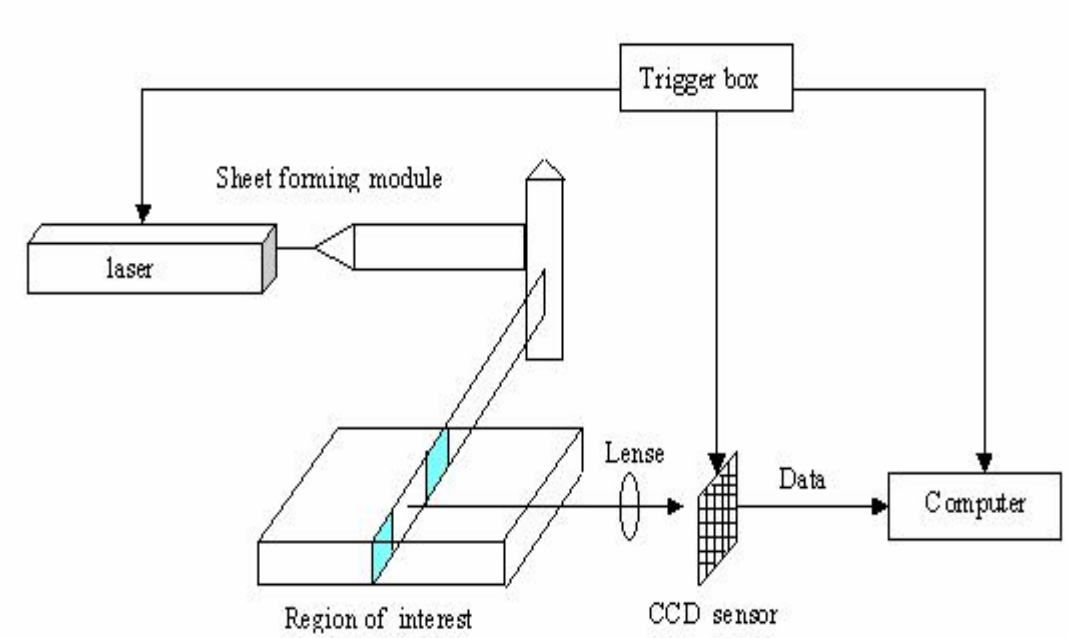

Figure 2.1: Basic laboratory set up for a complete PIV system

In field experiments, artificial seeding is not practical. Instead, image texture resulting from naturally occurring foam patterns is tracked with our PIV technique in an analogous way with pattern matching in a densely seeded flow [Holland *et al.*, 2001]. The surf zone and swash region contain a great deal of visual texture, namely distinct image intensity patterns resulting from surface foam, so determination of swash flow velocity vectors using PIV techniques is feasible.

Standard laboratory PIV requires a laser light sheet to illuminate the artificial, often reflective, seeding particles within the fluid transection. In our surface PIV measurements, no laser sheet is required. Nevertheless, proper lighting is still an issue. Reflections from varied imagery illumination in the presence of breaking waves can pose problems that negatively impact the image quality and care must be taken to reduce reflections and provide a nearly uniform light source.

Many PIV correlation algorithms have been used either in the time or frequency domain. The time domain cross-correlation algorithms are conventional

approaches, which are robust to the image noise but suffer from the computation load. The common ones are Maximum Cross-Correlation Method (MCC), Error Correlation method (ECOR), Minimum Absolute Deviation (MAD) method and a similar Minimum Quadratic Deviation (MQD). FFT-based correlation algorithm is usually more computational efficient but having a hard time dealing with poor quality images. Variable in formulation, the purpose of all algorithms is to find correspondent regions between two images taken sequentially and then obtain the offset and velocity of a particle or a pixel.

Investigations have been conducted to enhance the performance of PIV through selecting more accurate and efficient correlation algorithms, minimizing optical imagery noise to optimize input image quality by pre-processing, and adding post-processing procedures to remove PIV anomalies [Adrian, 1991; Grant, 1997; Raffel *et al.*, 1998; Hart, 1999; Melling, 1997].

2.2 Description of Correlation based PIV

2.2.1 Region of Interest

Acquired images are partitioned into square sub-regions where the average velocity of the group of pixels within each sub-region is determined. To better illustrate this, consider two almost identical synthetic images separated by a time lag, Δt (Figure 2.2), with one region in the first image shifted down and to the right in the second image. First, a small window, *I*, centered on the grid point, (x_0, y_0) is chosen, which numerically is a square matrix composed of intensity data at each pixel. *I* is called the interrogation window and has a size $(2i+1)\times(2i+1)$, where *i* is defined as the half width of *I*. Then, a larger search region *R*, $(2s+1)\times(2s+1)$, still centered on (x_0, y_0) is defined, where *s* denotes the maximum possible offset in pixels. Finally, within the search region, a search window, *S*, the same size as *I,* is chosen. *S* is sequentially moved across and downward on a pixel-by-pixel basis within the search region. A matching algorithm is performed at

each shift (Section 2.2.2), where the search window with the most similar pattern returns the horizontal pixel shift of I from (x_0, y_0), which when divided by the image to world coordinate ratio and Δt yields the velocity vector.

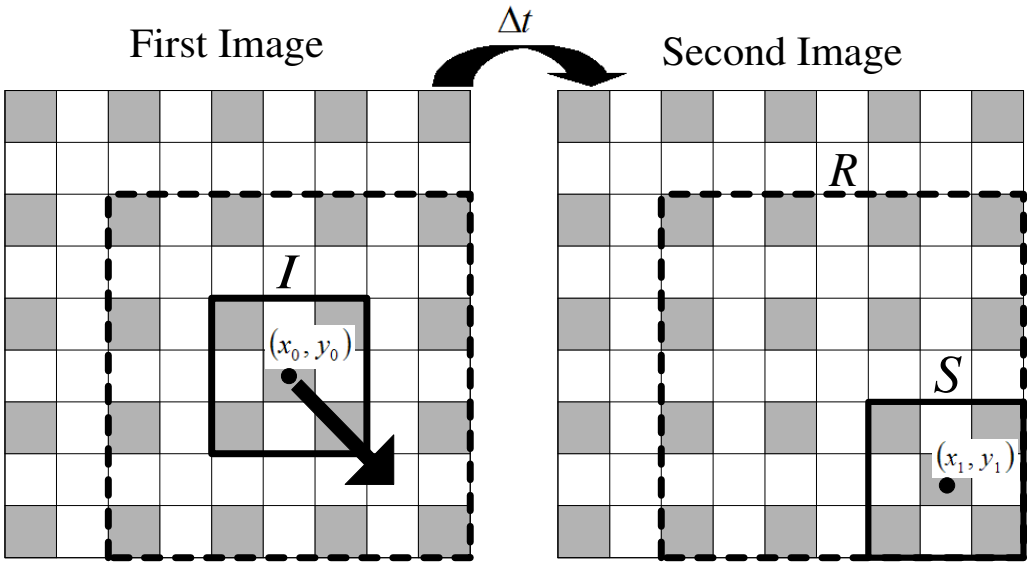

Figure 2.2: Schematic illustration of PIV matching with interrogation window I (solid square) in the first image, search region R (dashed square) and search window S in the second image, offset vector goes from (x_0, y_0) to (x_1, y_1)

2.2.2 Alternative Cross-correlation Algorithm

There are a variety of matching algorithms used in PIV. The most commonly used are maximum cross-correlation, error correlation, minimum absolute deviation and FFT-based correlation. These algorithms can be found in various sources but are included below for completeness.

2.2.2.1 Maximum Cross-Correlation (MCC)

The cross correlation function between two PIV windows is calculated as:

$$\gamma(x_1, y_1) = \sum_{j=1}^{2s+1} \sum_{k=1}^{2s+1} \frac{\left(S(j,k) - \bar{S}\right) \cdot \left(I(j,k) - \bar{I}\right)}{\left(\sigma_S^2 * \sigma_I^2\right)^{1/2}} \tag{2.1}$$

where I is the interrogation window centered on (x_0, y_0) in first image and S is the search window centered on (x_1, y_1) in the second image. The overbar and σ^2 denote mean and variance of the matrix respectively. As described above, MCC seeks to locate (x_1, y_1) of the maximized $\gamma(x_1, y_1)$, yielding the horizontal pixel shift from (x_0, y_0) to (x_1, y_1) as the most likely pixel shift for the interrogation window. Elements of the cross-correlation matrices $\gamma(x_1, y_1)$ range from 0 for no correlation to 1 for perfect matching. Note that the normalization in the denominator is important because un-normalized correlation would unduly weight the scheme towards higher pixel intensities. The ratios $s/\Delta t$ and $1/\Delta t$, multiplied by the pixel width, give maximum and minimum velocities that the technique may resolve. Here the pixel width is the real world distance a single pixel represents. Normally, an obvious cross-correlation peak is apparent (Figure 2.3a). However, in some cases when the particles are densely distributed or the image has a nearly uniform texture with small intensity gradient, single peak identification is difficult. In these instances, a weighting function is applied to the correlation matrix to amplify the near center (small velocity assumption) correlations (Figure 2.3b). In addition, a Gaussian fit function is used to interpolate integer pixel offsets to obtain sub-pixel resolution.

(a)

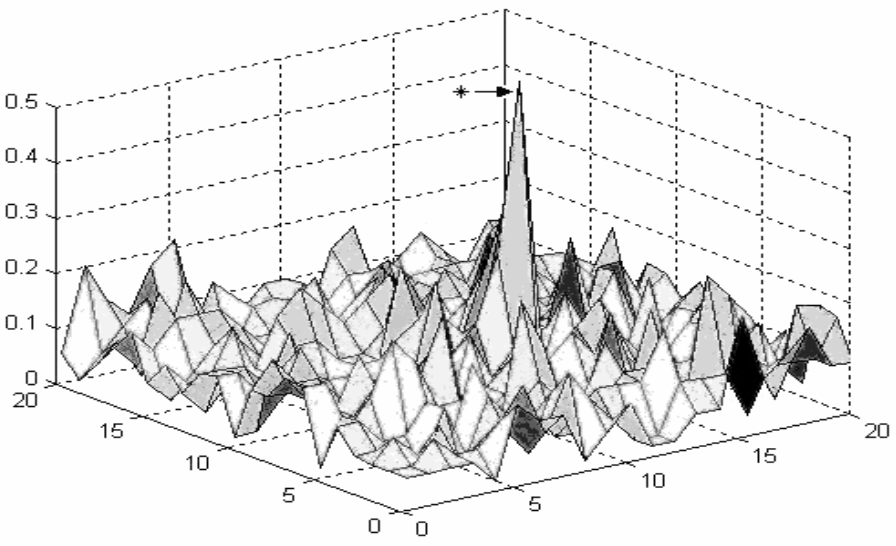

(b)

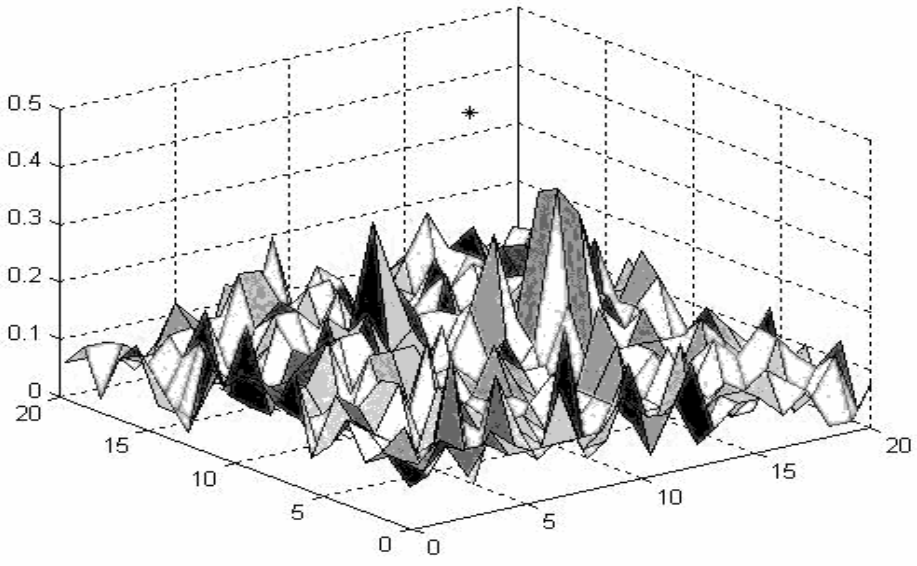

Figure 2.3: Cross-correlation matrix in a pixel space (a) with an apparent peak and (b) without an apparent peak, asterisk denotes the location of matrix center

Increasing the size of interrogation window will increase the computation time but yield more reliable vectors due to the larger spatial averaging region, while decreasing the value of I does the opposite. Thus, the optimal interrogation window size is the trade-off between accuracy and efficiency.

2.2.2.2 Error Correlation Method (ECOR)

The scalar product of two matrices and variance calculations in MCC has an expensive computational requirement. Therefore, a more time-efficient error correlation function has been defined as [Roth *et al.*, 1995]

$$\gamma(x_1, y_1) = 1 - \frac{\sum_{j=1}^{2s+1}\sum_{k=1}^{2s+1}\left|S(j,k) - I(j,k)\right|}{\sum_{j=1}^{2s+1}\sum_{k=1}^{2s+1}\left(S(j,k) + I(j,k)\right)} \quad . \tag{2.2}$$

Similar to MCC, $\gamma(x_1, y_1)$ in the error correlation also ranges from 0 to 1, but in a more computationally efficient fashion that only requires matrix addition and subtraction. Since this algorithm relies on the difference between interrogation and search windows, not removing the mean intensity implies a weighting towards higher pixel intensity. Thus, the techniques are more robust under conditions with a dark background and bright seeding material or tracking bright features such as breaking wave bubbles and foam.

2.2.2.3 Minimum Absolute Deviation (MAD) and Minimum Quadratic Difference (MQD)

$$\gamma(x_1, y_1) = \sum_{i=1}^{2s+1}\sum_{j=1}^{2s+1}\left|S(i,j) - I(i,j)\right| \tag{2.3}$$

$$\gamma(x_1, y_1) = \frac{1}{(2s+1)^2}\sum_{i=1}^{2s+1}\sum_{j=1}^{2s+1}\left(S(i,j) - I(i,j)\right)^2 \tag{2.4}$$

The above two functions are absolute deviation function and quadratic difference function respectively, and the location of minimum $\gamma(x_1, y_1)$ indicates

displacement between two windows. These two methods both assume the image has small pixel intensity gradient.

2.2.2.4 Cross-Correlation via FFT (FFTCOR)

While the above approaches in the time domain are calculated on the basis of nested loops by incremental shifts of *I*, correlation in the frequency domain significantly reduces computation requirements [Stevens and Coates, 1994]. Rather than performing a sum over all matrix elements as in time-domain approaches, the operations are reduced to a FFT, a complex conjugate multiplication and an inverse FFT. Acquired images are divided into equal sub-regions in the same scheme for each image pair. The shift of the center of mass between the interrogation window in the first image and search window in the second image is deemed as the translation of the interrogation window. Correlation in the frequency domain is through Fourier transforms, $S'(\alpha,\beta)$ and $I'(\alpha,\beta)$ of the search window and interrogation window respectively. The correlation function $\gamma(x,y)$ is calculated as the inverse Fourier transform of

$$R(\alpha,\beta) = S'(\alpha,\beta)I'^{*}(\alpha,\beta) \tag{2.5}$$

where the asterisk denotes the complex conjugate. Raw results from the frequency domain calculation of the correlation of *I* and *S* will differ from time-domain cross correlation in terms of normalization and lower signal to noise ratio due to spectral leakage, that could be compensated to some extent by including pre-processing procedures such as applying a two-dimensional window.

2.2.2.5 Multigrid Iterative Scheme (MFCOR)

In using the non-iterative FFTCOR, the signal to noise ratio is a crucial parameter because of the presence of degradation factors such as high velocity gradients, turbulent signature or pair loss due to in-and-out-of–plane motion [Scarano and Riethmuller, 1999]. Multi-pass iteration has been developed to compensate for this

disadvantage of single pass FFTCOR, where flow fluctuations at scales lower than the interrogation region cannot be resolved. By starting with large interrogation windows, coarse fluid orientation is determined in an initial, less time-consuming step. Sequentially reducing the window size then yields the finer flow structure, which has an improved signal to noise ratio compared with a procedure beginning with smaller windows. This method alleviates the difficulty of small interrogation windows with low signal to noise ratio or large interrogations windows that over-smooth the flow field in a single pass implementation.

The basic principle of multi-pass iteration [Hart, 1999; Scarano and Riethmuller, 1999; Nogueira, 2002] is illustrated in Figure 2.4 for the small subwindow (grey) shifted up and to the right. The image is first partitioned into large windows shown as the 4 squares denoted by solid lines. FFTCOR is applied to obtain the coarse flow displacement denoted by the prediction vector, Vp, for the next iterative step. Then the large windows are further subdivided into smaller windows (dashed lines) where the small subwindow of interest has a coarse predicted velocity Vp (Figure 2.4, left side). To obtain velocities for the small windows, the search is only carried out in the likely direction of offset determined by the predictor. FFTCOR is applied again for the smaller windows yielding another offset called the correction vector, Vc. The final displacement of the interrogation window is then determined by the resultant displacement, Vr, the vector sum of the predicted value and a small correction component (Figure 2.4, right side)

$$Vr = Vp + Vc \tag{2.6}$$

In practice, the iteration can continue to smaller window sizes as deemed necessary. Though this iteration procedure increases the computational load for PIV processing, it is still far more efficient than conventional cross-correlation methods if the correlation is performed in the FFT domain.

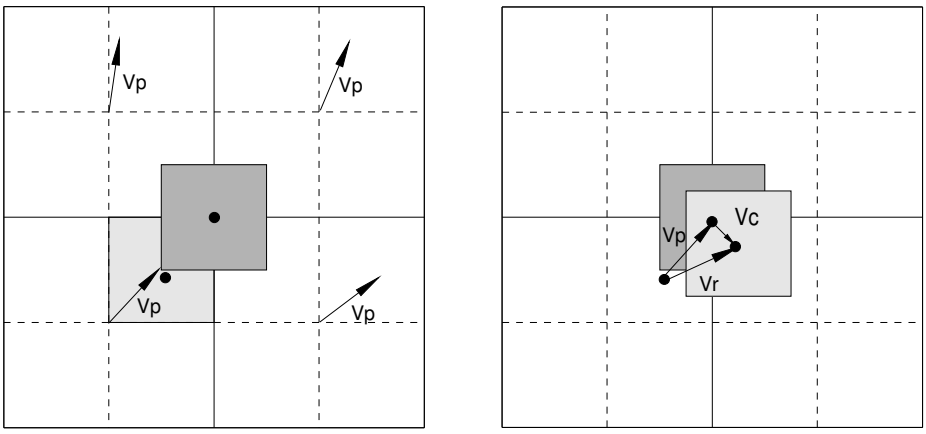

Figure 2.4: Schematic illustration of multi-grid iterative PIV (MFCOR) for coarse windows (solid lines) and better resolved windows (dashed lines). Diagram shows prediction vector, Vp, correction vector, Vc, and resultant vector Vr. The black dots denote the center of windows

2.2.3 Weighting Function and Sub-pixel Interpolation

When the cross-correlation has been performed, a measure of the displacement is found by detecting the location of the highest correlation peak. Just detecting the peak will result in an uncertainty of $\pm 1/2$ pixel in the peak location. However, the accuracy can be increased by bowl fitting and interpolation. A weighting function should be applied to the cross-correlation function to avoid bias towards the displacement other than zero and also allow sub-pixel resolution. Figure 2.5 demonstrates the bowl-fitting procedure. (a) is a raw cross-correlation plane obtained in pixel resolution and (b) is a bowl-fitting function used in this project, it has a maximum value 1 at the center and 0.15 at the edge of the window.(c) is the sub-pixel resolved cross-correlation convoluting the raw cross-correlation with bowl-fitting function.

(a)

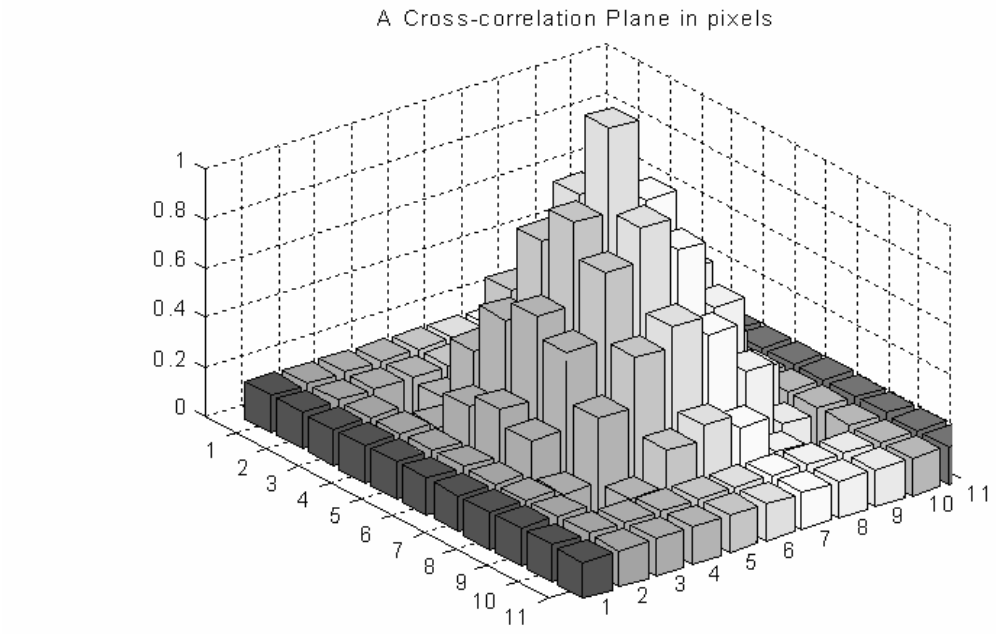
A Cross-correlation Plane in pixels
1
0.8
0.6
0.4
0.2
0
1 2 3 4 5 6 7 8 9 10 11
1 2 3 4 5 6 7 8 9 10 11

(b)

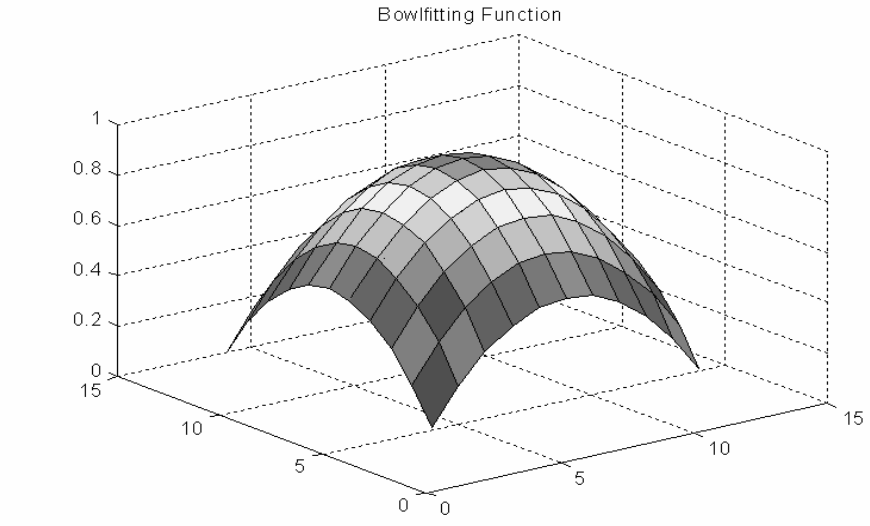
Bowlfitting Function
1
0.8
0.6
0.4
0.2
0
15 10 5 0
0 5 10 15

(c)

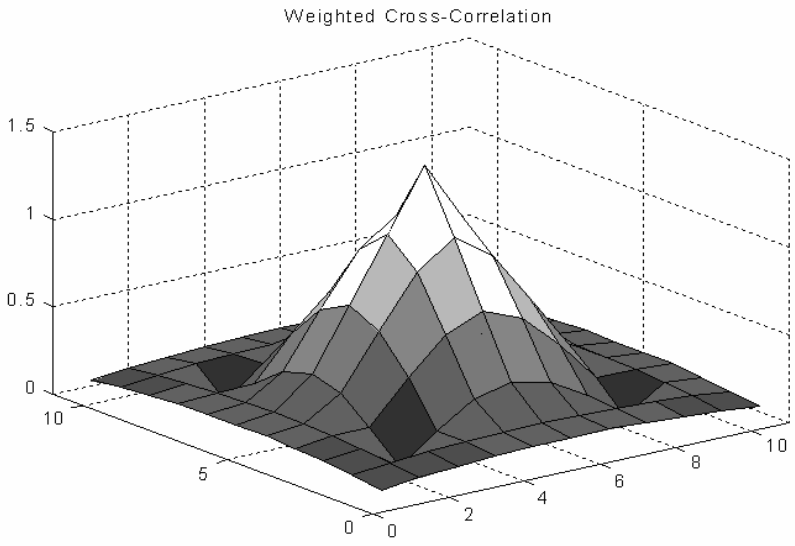

Figure 2.5: Bowl-fitting function to interpolate cross-correlation into sub-pixel resolution. (a) A typical cross-correlation plane in pixel coordinate, (b) bowl-fitting function with maximum of 1 and minimum of 0.15 (c) the cross-correlation function after applying bowl-fitting.

2.2.4 Vector Post-processing

Sometimes vectors significantly different from neighboring vectors are returned either because an erroneous peak dominates the more appropriate matching peak or background noise causes multiple similar peaks among which the nearest one is chosen. Each vector in turn is compared to the local mean surrounding it, and is deemed to be bad if it is different from the mean by some given threshold [Fujita and Kaizu, 1995]. Under these circumstances, velocity post-processing is essential. Assuming the continuity of the flow field, post-processing is basically a smoothing operation. Criteria include signal to noise ratio, dominant peak to secondary peak ratio, global filters and local filters. Raffel *et al.* [1998] presented an advanced post-processing method using the dynamic mean

value operator to discard a vector when the absolute difference between the vector magnitude, ω and that of the mean magnitude of the eight surrounding vectors exceeds a certain threshold. The mean value, μ_{mag}, of the eight vectors $\omega_{2D}(n)$ surrounding the center vector at a location (x_n, y_n) and their difference are both calculated.

$$\gamma_{mag}^2 = \frac{1}{N}\sum_{n=1}^{N}\left(\mu_{mag} - \omega_{2D}(n)\right)^2 \tag{2.7}$$

And a vector would be rejected if $\left|\mu_{mag} - \omega\right| > \varepsilon_{mag}$, where $\varepsilon_{mag} = K_1 + K_2\gamma_{mag}$ is an error threshold defined by user supplied constants K_1 and K_2. The direction of vector, θ, also can be estimated using constants K_3 and K_4 in $\varepsilon_{dir} = K_3 + K_4\gamma_{dir}$. So, a vector in post processing scheme will be rejected if

$$\left|\mu_{mag} - \omega\right| > \varepsilon_{mag} \text{ or } \left|\mu_{dir} - \omega\right| > \varepsilon_{dir} \tag{2.8}$$

Once the locations of all the rejected vectors have been determined, they are replaced using a weighted average of the eight nearest non-rejected vectors. Holland *et al.* [2001] successfully applied the dynamic mean operator to the magnitude and direction of swash zone PIV data and showed reductions in RMS error on synthetic data of 21%. Post-processing in this study will similarly follow the Raffel *et al.* [1998] technique.

2.2.5 Synthetic Image Testing and Error Analysis

To compare the performance of the various PIV algorithms, synthetic images are created with white pixels randomly distributed on a uniformly black background with a particle density of 20% (Figure 2.6a). A second image (Figure 2.6b) is generated by applying a synthetic rip current flow field (Figure 2.7) and shifting the pixels from the first image in magnitude and direction based on the prescribed local flow. Since the image is in integer pixel space, offsets are rounded to the nearest pixel, leading to a small source of error in pixel resolution, which will not be a problem in the actual images. This

synthetic image pair is then used as a test bed to implement accuracy assessment of the various PIV algorithms in predicting the prescribed rip current flow field.

Figure 2.8a shows the computed velocity field of the synthetic image pair using MFCOR PIV routine with an interrogation window size iterating from 32x32 to 16x16. Most of the PIV-derived vectors agree well with their prescribed counterparts and the orientation of the local flow field is generally well-resolved with a few apparently spurious vectors. In the synthetic test case, one possible error source is the requirement of integer pixel offsets, which causes a slight bias in the comparisons between the synthetic flow field and the velocities that can be derived through PIV. This difficulty does not exist in real images. Other spurious vectors occur in regions of flow heterogeneity where large spatial velocity gradients or strong flow rotation are observed. Figure 2.8b shows the result of the post-processing procedure applied to the vector field of Figure 2.8a using the same constants as those used in Holland *et al.* [2001]. After post-processing, Most of the obviously spurious vectors are removed and replaced by the local mean vector that more appropriately matches the prescribed flow field (Figure 2.7). This post-processing procedure causes the normalized RMS error (Equation 2.7) to decrease by 17 % (0.46 to 0.38). Some of the remaining error can be attributed to the fact that each erroneous vector contributes to its local mean.

(a)

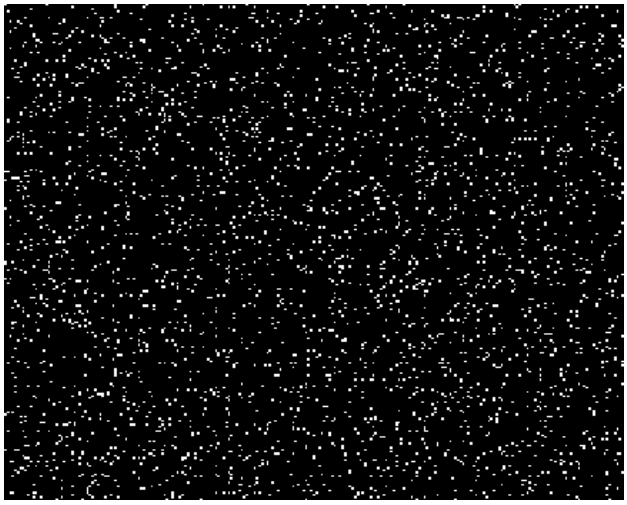

(b)

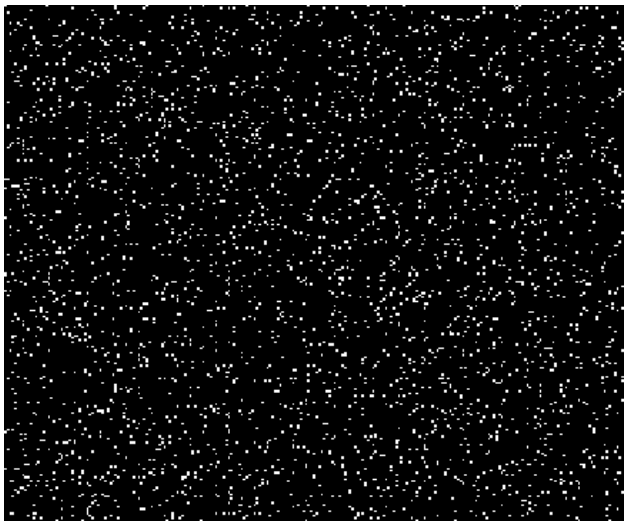

Figure 2.6: Synthetic images with white dots on black background. (a) is random pattern and (b) is shifting all the dots in (a) based on the corner flow

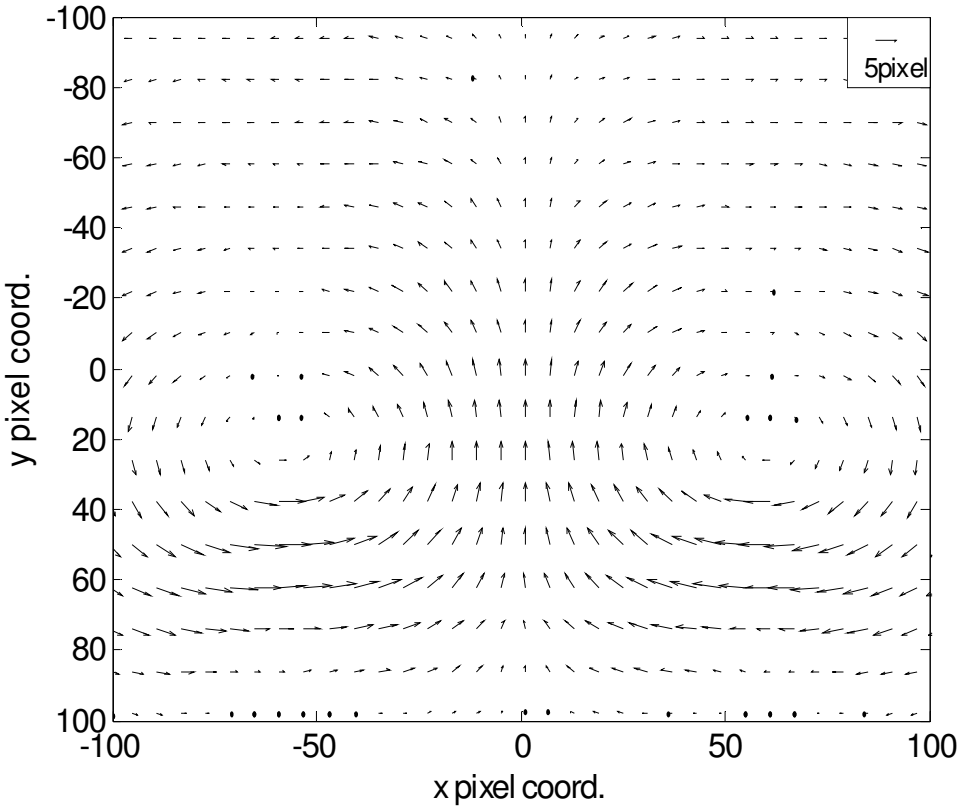

Figure 2.7: Synthetic rip current flow pattern (right) applied to the synthetic image to generate the second image of the PIV input pair. A scale vector of 5 pixels is shown in the upper right.

The root-mean-square error (RMS) of the vector magnitude is chosen as an accuracy assessment criterion,

$$RMS = \left[\frac{1}{M \times N} \sum_{j=1}^{M} \sum_{k=1}^{N} \left(\frac{v_{PIV}(j,k) - v_{SYN}(j,k)}{v_{SYN}(j,k)} \right)^2 \right]^{1/2} \tag{2.9}$$

where $v_{PIV}(j,k)$ denotes the PIV–derived vector magnitude for grid point (j,k) and $v_{SYN}(j,k)$ is the prescribed vector magnitude at grid point (j,k). M and N are the number of grid points horizontally and vertically across the image. Figure 2.9 is the histogram showing the normalized error of Figure 2.8b, in which case there is zero noise. The mean deviation between the PIV estimates and prescribed vector was less than 1% and 80% of the estimated vectors had normalized errors of 0.17 or less.

In Figure 2.10a, error analysis for the synthetic rip current flow field is performed using interrogation lengths ranging from 4 (interrogation window is 9×9) to 15 (interrogation window is 31×31) for ECOR, MAD and MCC as a function of computation time. As the interrogation window size increases, so does the computational overhead. On the other hand, FFTCOR uses 32x32, 16x16 and 8x8 as a window size and MFCOR uses iterative window sizes of [64x64; 32x32], [32x32; 16x16] and [16x16; 8x8]. The two FFT-based correlation algorithms are the most time-efficient. It is clear that MFCOR has increased accuracy without a significant increase in computation time. The three time domain correlation methods require nearly an order of magnitude more time than the FFT-based methods for this image pair. As previously mentioned, the conventional methods implement a pixel by pixel comparison in the time domain, while the FFT methods only apply a FFT and an inverse FFT at each time to compute the correlation coefficients. The time difference of roughly 10-40 s may seem insignificant

for a single image pair, but is significant when considering a 20-minute real imagery time series collected at 10 Hz (as is the case for this study; see Chapter 3).

To further test the robustness of the five PIV algorithms, different levels of random Gaussian distributed noise are introduced when producing the second synthetic image. Six noise levels are chosen from 0 to 100 in intensity value to degrade the image. Out of the five methods, ECOR, MAD and MCC exhibit essentially the same level of sensitivity to the added noise (Figure 2.10b). The RMS error increases steadily as more noise is introduced. The majority of the RMS signal is still lower than 1 even after the signal to noise ratio is at a minimum. On the other hand, FFTCOR and MFCOR exhibit difficulties when high intensity noise is introduced into the image. RMS errors increase rapidly as the signal to noise level drops.

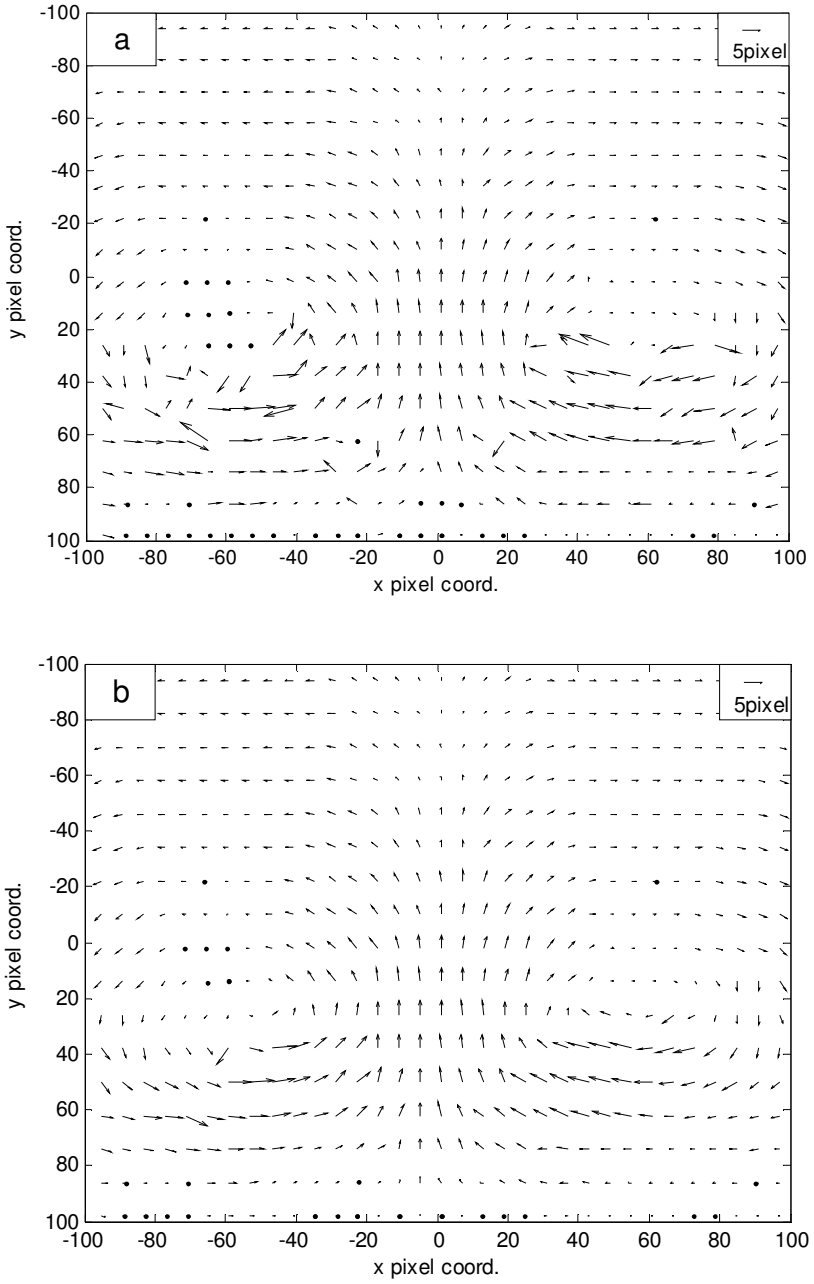

Figure 2.8: (a) Result of PIV analysis of the synthetic image pair prescribed in Figure 3. The correlation algorithm employed is MFCOR with iterative window sizes of [32x32; 16x16]. (b) Vector field of post-processed velocity vectors. A scale vector of 5 pixels is shown in the top-right corner.

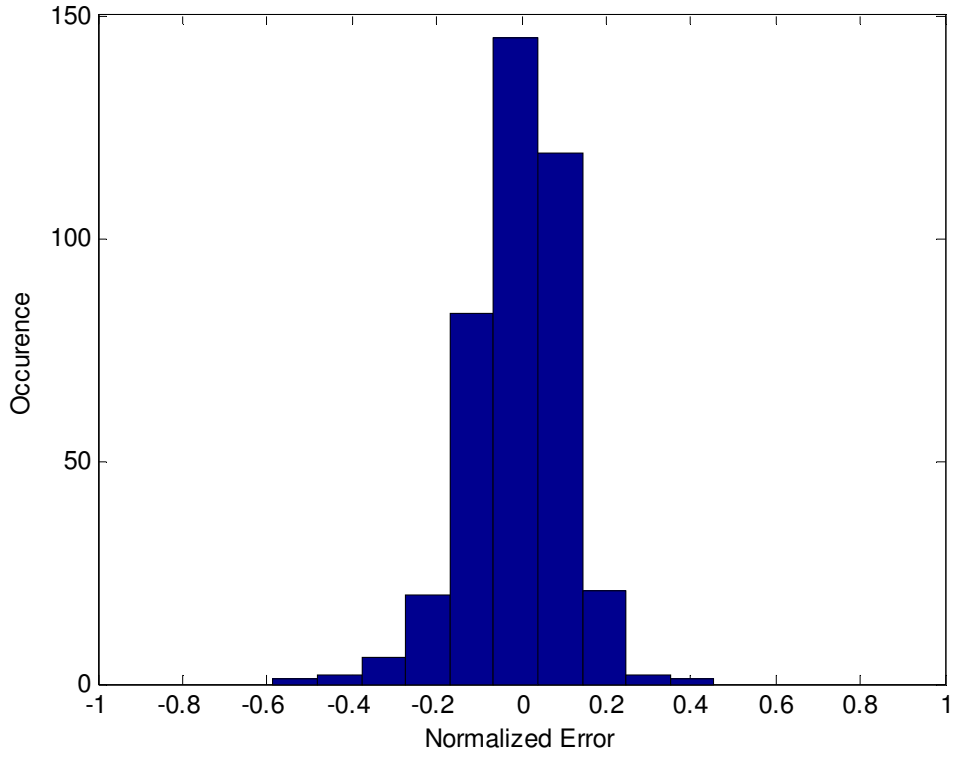

Figure 2.9: A histogram of normalized errors for the synthetic test of Figure 2.8b

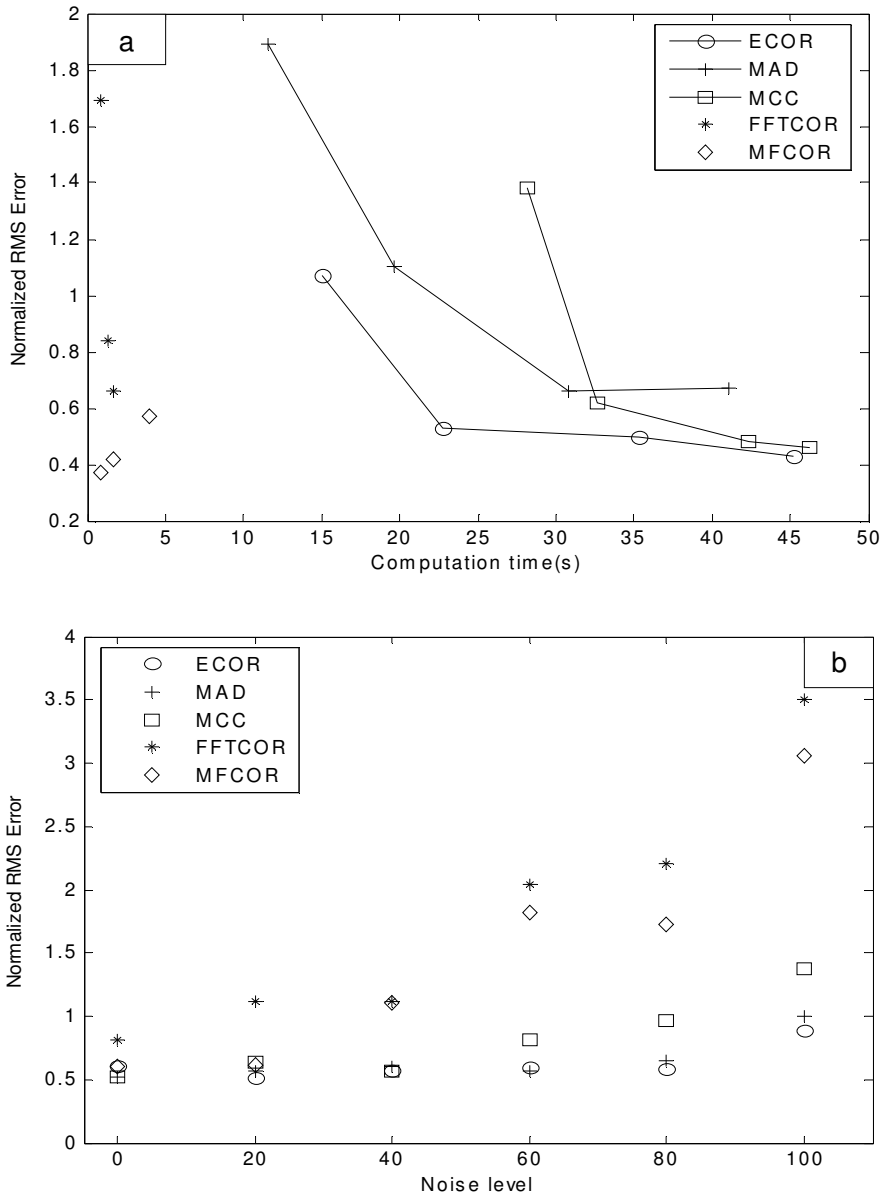

Figure 2.10: (a) Comparison of time efficiency of ECOR, MAD, MCC, FFTCOR and MFCOR with noise level 0 and window sizes of [9x9], [13x13], [17x17] and [31x31] for time domain algorithms, [32x32], [16x16] and [8x8] for FFTCOR and similarly square windows with width iterating from [64x64; 32x32], [32x32; 16x16] and [16x16; 8x8] for MFCOR. (b) Noise sensitivity test of the five algorithms with randomly distributed Gaussian noise levels of 0, 20, 40, 60, 80, 100 with the same interrogation window sizes as for (a).

2.3 Camera and Laboratory Calibration

It is necessary to pre-process actual laboratory flow field images before they are fed into a PIV routine, because the image velocimetry technique is more straightforward if performed on geo-referenced imagery. The 2D image coordinates need to be transformed to 3D world coordinate in order to obtain the real flow field data from snapshots. There are two sets of parameters governing the transformation between the two coordinates system. One is a set of implicit parameters, which indicates distortion of camera and lens set up. Different camera and lens combinations would have a particular distortion effect due to different focal length, aperture, camera technical parameters and image acquisition hardware. The other set of explicit parameters comprise geometrical information, including the position of the camera with respect to the world coordinate, its orientation and shooting angle. The determination of the implicit parameters is called lens or camera calibration, once it has been calibrated, the parameters can be regarded as the system's physical constants. While the calculation of the explicit geometric parameters is called laboratory or field calibration, and it needs to be recalibrated under each different experimental scenario if the camera location or orientation is altered. In the present research, a direct linear transformation (DLT) method suggested by Abdel-Aziz and Karara [1971] is taken for the estimation of distortion coefficients based on deviations of observations from this closed form solution. For the mathematical model for laboratory calibration, we follow Holland *et al.* [2001]. In all, the implicit parameters $(\lambda_u, \lambda_v, u_0, v_0, k_1, k_2)$ and explicit parameters $(x_c, y_c, z_c, f, \phi, \tau, \sigma)$ add up to 13 unknowns, in which λ_u and λ_v are the scale factors, u_0 and v_0 are image center coordinates, k_1 and k_2 are camera distortion coefficients, (x_c, y_c, z_c) is the three-dimensional location of the camera, f is the effective focal length and (ϕ, τ, σ) are the three rotation angle azimuth, tilt and roll, respectively. Calibration is a procedure to reduce the unknowns.

2.3.1 Camera and Lens Calibration

Camera calibration is a necessary step for both two-dimensional and three-dimensional computer vision in order to extract useful and accurate information from images taken. Zoom lens without edge distortion would give a more comprehensive picture for applications such as active computer vision, three dimensional reconstruction, feature tracking and image velocimetry. To meet the requirement of different laboratory experiment scenario, such as lighting condition or shooting distance, assembly of cameras and lens are stored. Thus, to calibrate each combination of available lens and camera is a significant job so that particular zoom, aperture, focus length, field of view and spatial resolution for each combination can be taken into account to undistort the snapshots. The goal of zoom lens calibration is to determine the relationship between zoom lens settings and intrinsic camera parameters. Both for fixed focal length camera and the adjustable one, unfortunately, the relationship is rather complicated. Many calibration procedures are proposed firstly by photogrammetry community and recently by computer vision experts. Different from professional photographers, laboratory experimenters are satisfied with simple model camera calibration with acceptable accuracy.

To simplify the procedure of removing edge distortion, the technique only requires that the camera observe a plane panel, which is positioned parallel to the camera focal plane. The pattern used is a black background with evenly spaced 20 x 15 white circles, printed by Laser printer and attached to a hard cover or other smooth surface. In some other calibration applications, the camera is moved from time to time at different orientations or two attached but perpendicular planes are placed within one view [Sturm and Maybank, 1999]. It is more flexible compared to our one-angle shooting, but more difficult to initialize. We simply choose the most inexpensive, convenient and robust plane calibration method by shooting the pattern at right angle repeatedly. Each time we establish a laboratory camera calibration system and adjust the azimuth or tilt of the camera to let the edge of field of view and white frame of the pattern overlap as much as

possible. To determine the intrinsic camera parameters for each camera and lens combination, the procedure is repeated 4 times independently to reduce the external interference and user's operation error. The raw image is the same control points, but distorted by the camera and lens system, as figure 2.11a.

In our research, we choose the radial distortion model [Holland *et al.,* 1997] in which the distortion coefficients k_1 and k_2 are expressed in an odd-order polynomial:

$$\Delta r = k_1 r^3 + k_2 r \tag{2.10}$$

where Δr is the radial deviation between the location of predicted control points (u_p, v_p) and the ones in distorted image (u_d, v_d)

$$\Delta r = \sqrt{(u_d - u_o)^2 + (v_d - v_o)^2} - \sqrt{(u_p - u_o)^2 + (v_p - v_o)^2} \tag{2.11}$$

and r is the radial distance between the control points and image center

$$\Delta r = \sqrt{(u_d - u_o)^2 + (v_d - v_o)^2} \tag{2.12}$$

(a)

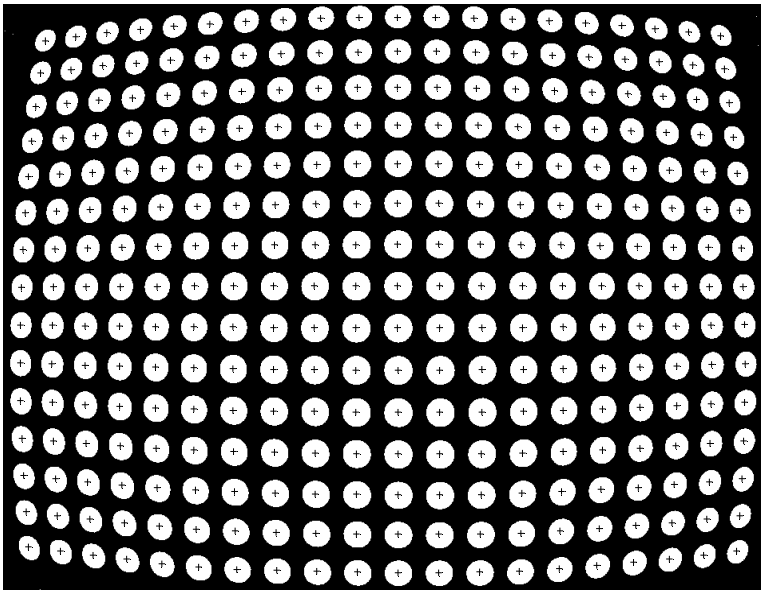

(b)

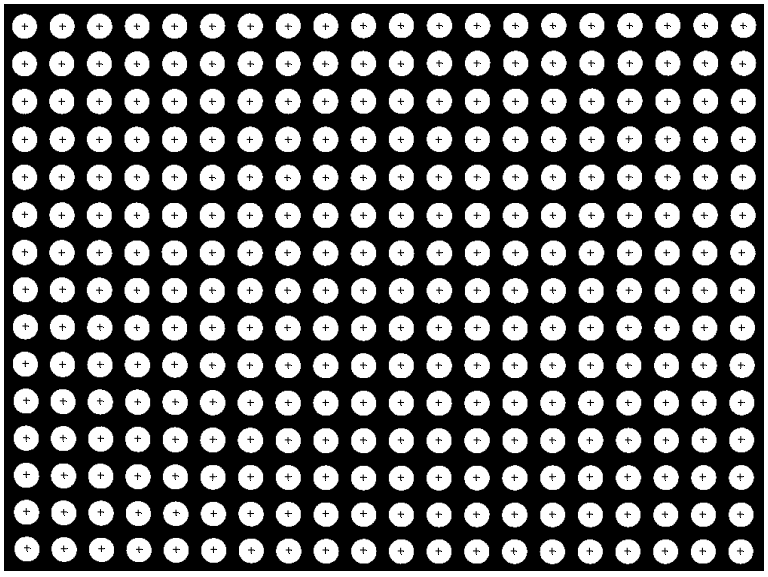

Figure 2.11: (a) is the distorted image by shooting the pattern with camera (4.2 mm lens) focal plane and pattern plane in parallel and (b) is the predicted pattern plane. The crosses represent the center of white dots.

Based on the distorted pattern, approximately the center of the image could be regarded as the center of the frame buffer. The image center determined using this type of minimization closely approximates the center laser approach as described by Lenz and Tsai [1988], at least for lenses with significant amounts of distortion. Once the center of the predicted pattern is located, an estimated matrix of dots can be distributed evenly with the same number of rows and columns as the original image. As shown in Figure 2.11b, the most accurate prediction coordinates should be in accordance with where the white circles are located in the original plane pattern. It can be seen from Figure 2.12 that the center of prediction and distortion is well matched, but the wide-angle lens causes the image to be spherised or inflated, especially at the edge of the zoom, which is termed as Barrel effect in photogrammetry.

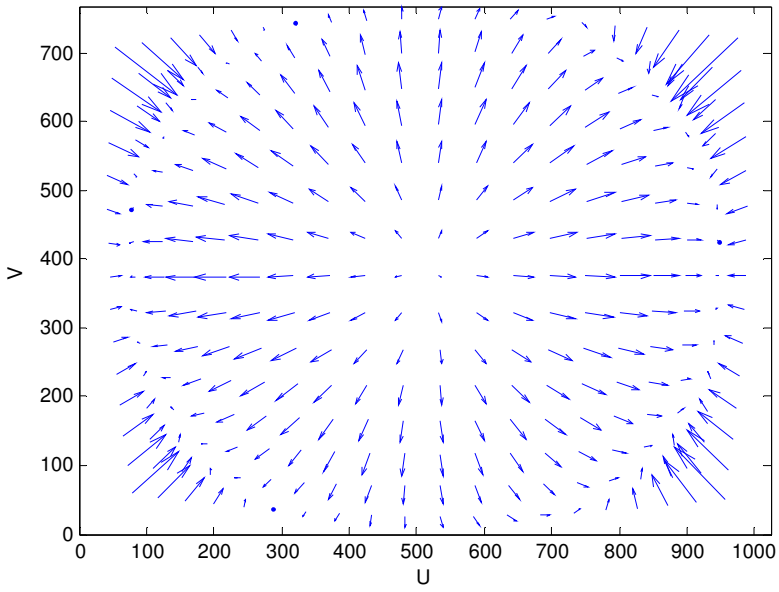

Figure 2.12: The radial distortion experienced by a 4.2 mm lens, the arrow starts from predicted circle location to distorted one, the length of the vectors has been amplified to emphasize the general trend.

(a)

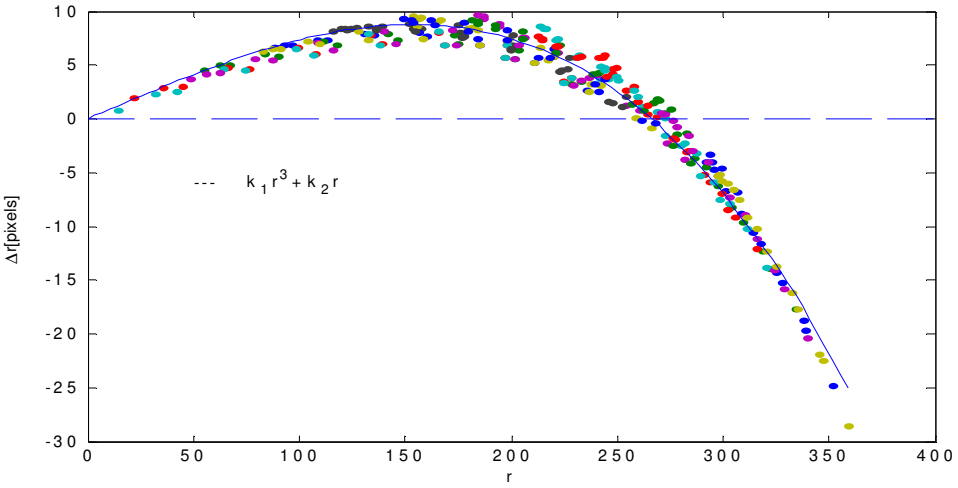

(b)

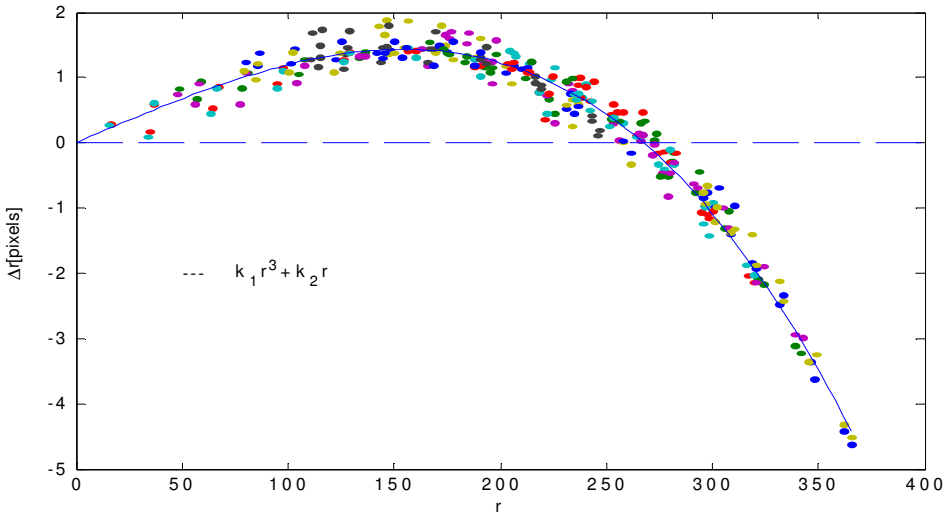

Figure 2.13: The best fit curve for the coefficients in the polynomial, where r is distance from dots to image center and Δr difference between distorted and predicted dots center, (a) and (b) are for 4.2 mm and 8.5 mm lens respectively.

Two cameras and three lenses are all calibrated. One of the cameras is Fire-i400, with a ¼" interline CCD and allowing 640×480 pixel output. The other is a DFW X710 camera manufactured by SONY, it provides XGA resolution 1024×768 up to 15 frames per second. The four lenses all have fixed focal length, which are Pentax 12 mm and 6.0 mm and Computar 4.2 mm and 8.5 mm.

In table 2.1, U_{std} and V_{std} are standard deviation of all horizontal and vertical difference between prediction and distortion, U_0 and V_0 are location of predicted image center and k_1 and k_2 are distortion coefficients in Equation 2.10. All the values are obtained by averaging three or six independent calibration operations, which means the camera set up is re-established for each time. Images from DFW X710 camera has 1024×768 pixel resolution, in this image processing technique, all images are stretched or compacted into 640×480 format. That is why images from both cameras have center around (320, -240). It is obvious from the table that camera and lens selection both play an important role of image distortion. The shorter the focal length of the lens, the more serious the distortion is. The image taken by the 12 mm lens matches the original pattern very well, however, the displacement of the white circles can be visually observed in the 4.2 mm lens pictures. The bigger scale factor also causes larger amounts of distortion because of its wider field of view. Just like Figure 2.12 indicates, more serious distortion occurs along the edge of the zoom lens rather that the center. So in most calibrations, the image center is almost the same. k_1 and k_2 are system specific, which means they can be used to un-distort the image from certain lens and camera combination.

Table 2.1: Camera Calibration Parameters Determined by Pattern Shooting Laboratory Calibration (F is for Fire-i400 camera and D is for DFW X710 camera, image processors are all the same for each calibration)

	$4.2mm(F)$	$6.0mm(F)$	$8.5mm(F)$	$12mm(F)$	$4.2mm(D)$	$6.0mm(D)$	$8.5mm(D)$
U_{std}	3.358	0.904	0.603	0.486	8.645	2.952	1.629
V_{std}	2.680	0.799	0.503	0.501	6.987	2.176	1.371
U_0	322.467	322.633	321.800	322.833	319.167	322.667	320.200
V_0	-242.900	-249.233	-241.067	-233.433	-238.300	-237.500	-234.833
k_1	-6.853e-007	-1.7717e-007	-1.2100e-007	-8.7577e-008	-1.2488e-006	-3.0548e-007	-2.3253e-007
k_2	0.0477	0.0124	0.0085	0.0063	0.0855	0.0220	0.0111

(a)

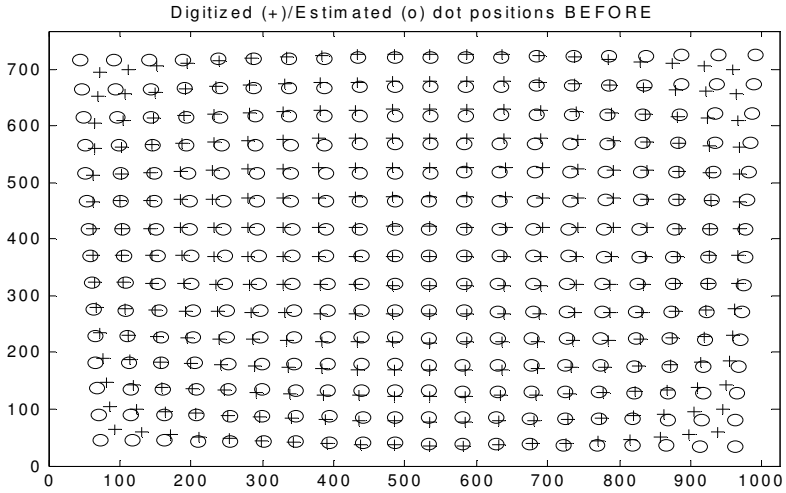

(b)

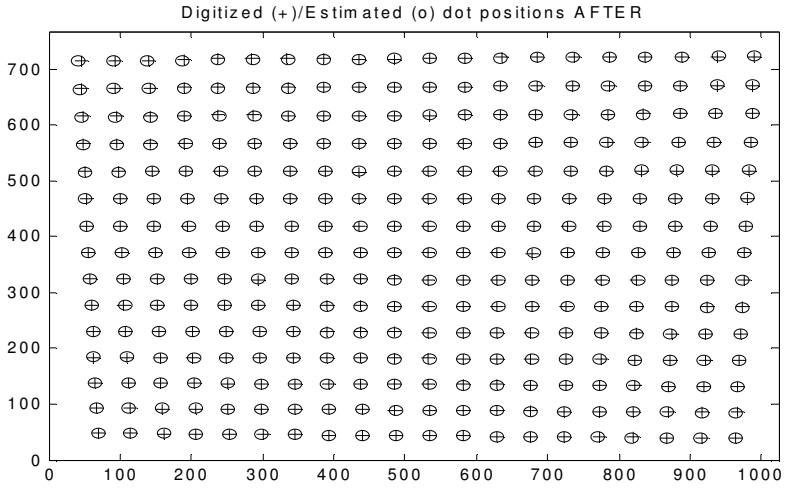

Figure 2.14: (a) The comparison of predicted and obtained dots position by Computar 4.2 mm camera before calibration and (b) after calibration. 'o' represents where they should be and '+' represents the adjusted dots center

2.3.2 Image Rectification

For this laboratory study of rip currents we opted for higher resolution, choosing Sony DFW X710 firewire camera and a 6mm Pentax lens to acquire imagery. In order to perform PIV, imagery must be cast into a local coordinate system. And the oblique nature of the originally acquired images doesn't allow us to extract the surface velocity accurately, which necessitates a converting procedure, called image rectification. The laboratory calibration is performed in the wave basin in Center for Applied Coastal Research, University of Delaware. The detailed description for the basin geometry is elaborated in section 3.1. The implementation of the rectification is achieved by using a handful of the fixed ground control points and geo-rectification procedures [Holland, *et al.,* 1997] that map the image to a specified horizontal plane. The implicit parameters as unknowns for the calibration system have been eliminated in the prior procedure of lens calibration. Another essential set of parameters is the rotation angle of camera, its ϕ (azimuth), τ (tilt) and σ (roll). With the implicit parameters having been determined in previous camera calibration, the parameters to be determined have been reduced to seven $(x_c, y_c, z_c, f, \phi, \tau, \sigma)$. Figure 2.15 gives the general geometrical basis of image coordinate and world coordinate transformation. Figure 2.16 is the schematic plan view of the wave basin, the marking crosses are painted on the basin floor, which has a smooth slope. As ground control points (GCPs), the three-dimensional world coordinates of the crosses on the floor are all known by previous laboratory survey. The camera is placed around $(17m, 9m)$ out of the basin with an approximate height of $5.6m$, obliquely and distantly shooting the area around the right channel between the bars. In our application, it is not feasible to get the measurement of the accurate location and rotation of the camera and lens. Thus, given world coordinates of seven objects (x, y, z) and their corresponding un-distorted

image coordinates (u^*, v^*), the unknown camera position, field of view, azimuth, tilt and roll, could be calculated using a standard iterative minimization technique that utilizes linearized versions of collinearity equations [Holland, *et al.,* 1997]. As shown, (x_c, y_c, z_c) is the optical center of the camera and regarded as the idealized position of camera. (x, y, z) represents the world coordinate of a location in the three dimensional space and (u, v) is its projection on the image plane, which is a two dimensional coordinate system. In other words, (u, v) corresponds to (x, y, z) by the same identity on a photogrammetric basic. To transform the image pixel coordinate of all the objects in image to a real world coordinate, it is a challenging application because 3-dimensional coordinates of the 2-dimensional pixel location cannot be determined (two equations with three unknowns). As we are seeking to extract the surface flow velocity that is projected onto the still water level, one of the three coordinates (elevation) after transformation is constrained and the transformation would be feasible. As shown in Figure 2.17 and Figure 2.18, the circumscribed area in the acquired image is rectified as a square area with a right view angle, the black triangle at the lower right corner of Figure 2.18 is out of view. Here the extrapolation is not necessary, thus the uncovered area is all set to zero.

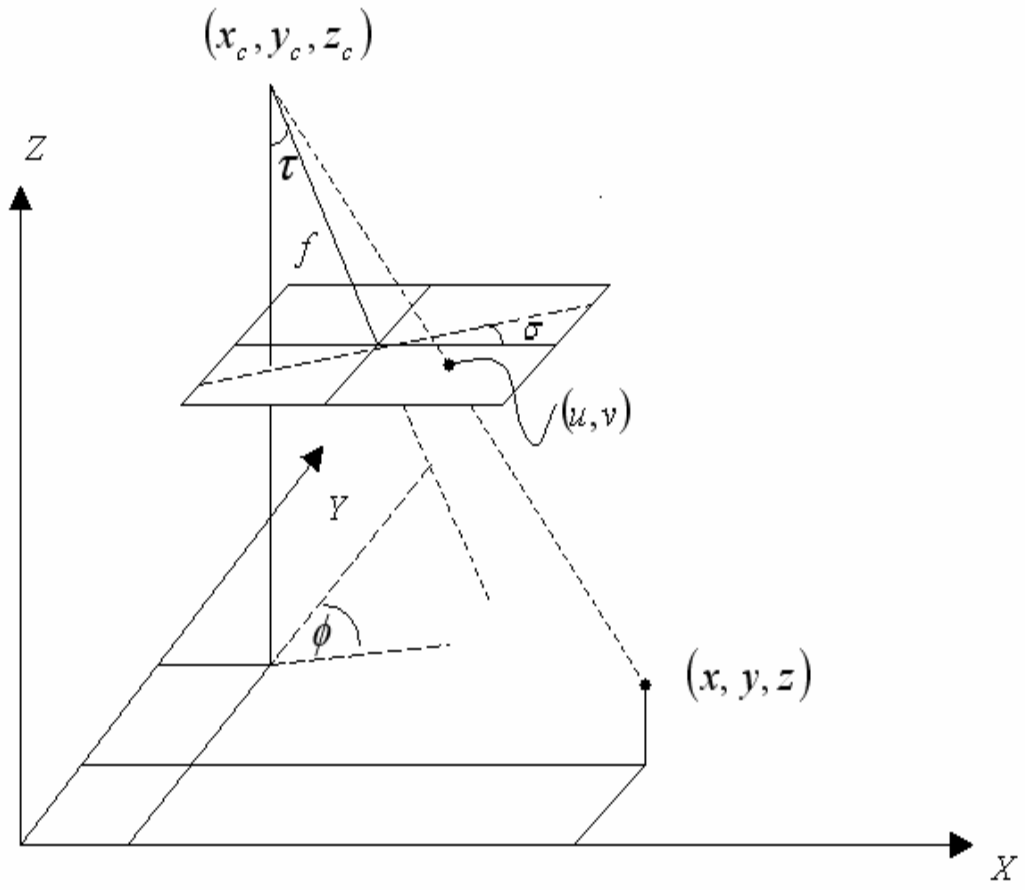

Figure 2.15: Collinearity relationship between camera location, orientation, image and world coordinate

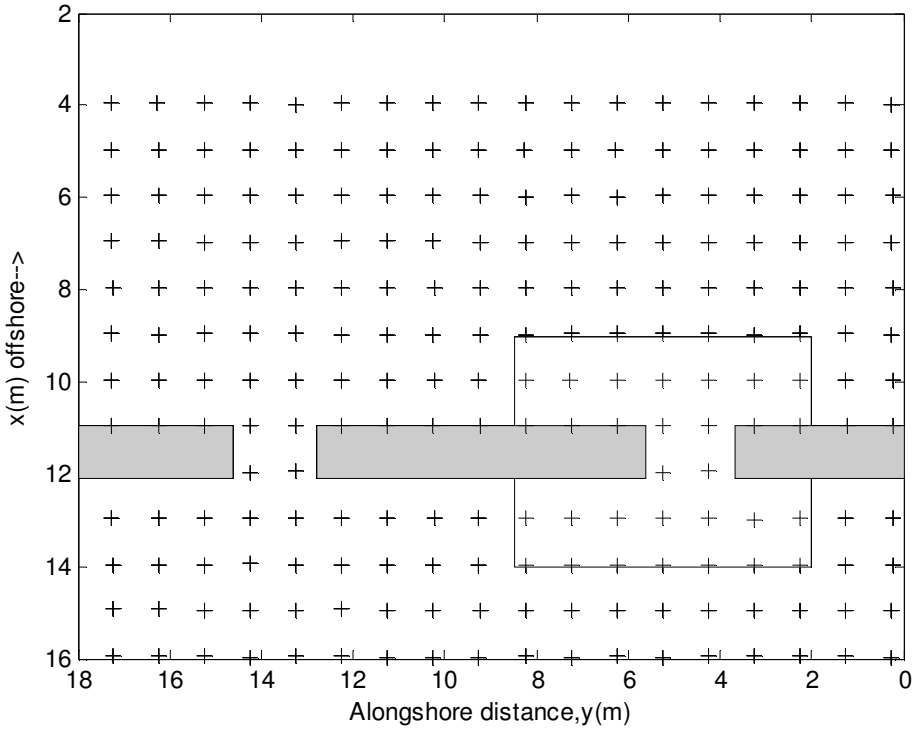

Figure 2.16: Plan view of wave basin geometry, plastic "sand" bar (gray), ground control points (+'s) and region of interest (black box).

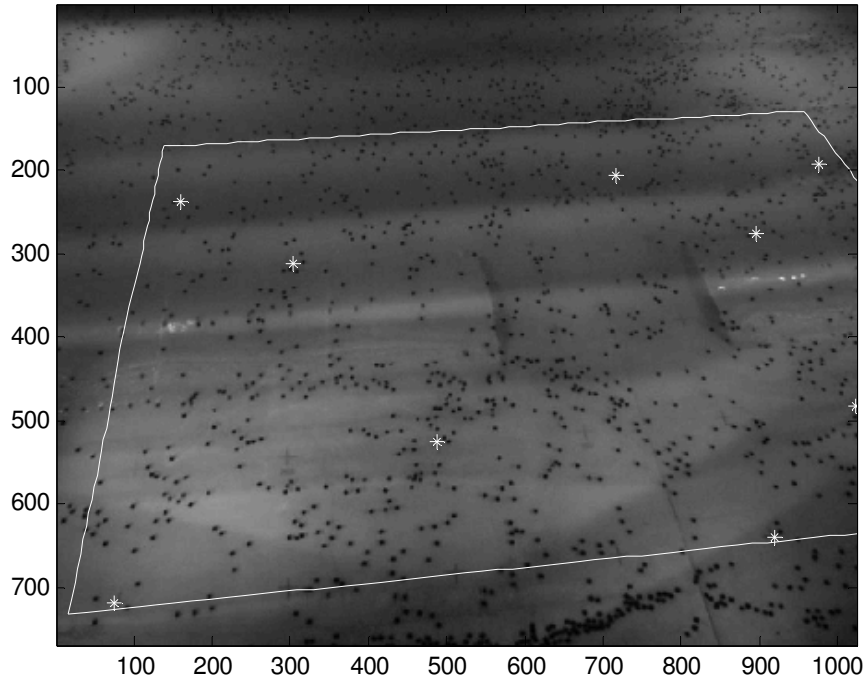

Figure 2.17: An oblique angle view of the basin showing the region of interest in the white box and ground control points used for geo-rectification purposes as white stars The overhead view of the region of interest rectified to the still water level

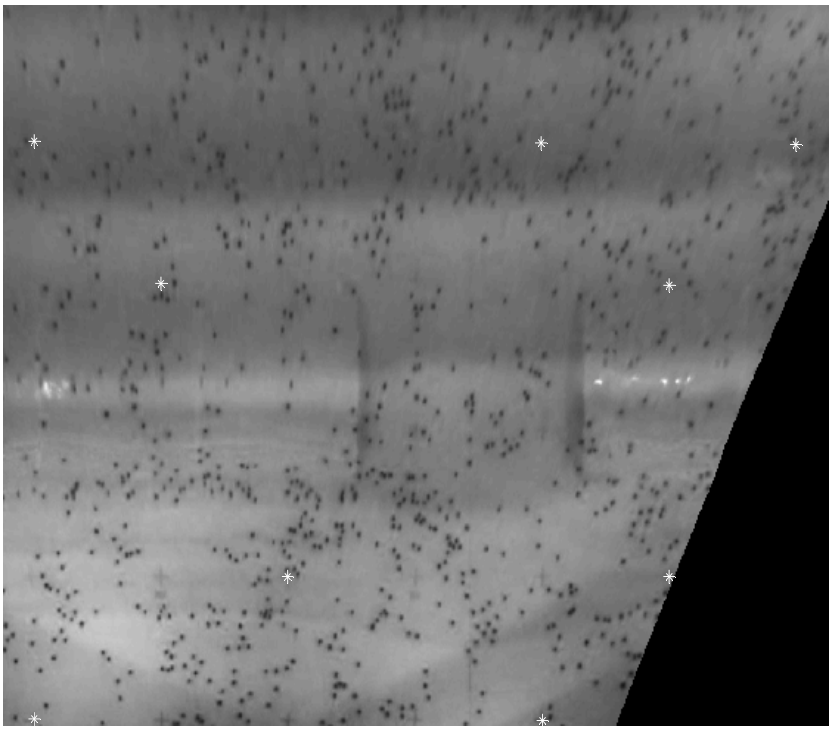

Figure 2.18: The overhead view of the region of interest rectified to the still water level

2.3.3 Image Pre-processing

After image rectification, there are still image imperfections that will negatively impact the PIV analysis. The inevitable heterogeneity of the illumination make the image have low-frequency background variation, the edge of the bar is still occasionally visible, and wave signature due to the light reflection sometimes obscure the image feature of the particles. Features like these will all affect the cross-correlation calculation and matching. Pre-processing is performed on the rectified images to make them more suitable for use in the PIV analysis: (1) the acquired color image is converted to a gray scale image and digitized as a matrix (2) the image is inverted by computing the reverse negative making the black tracer particles white and bright background dark, (3) A two-dimensional (3x3 pixel) median filter is applied to sharpen the target edge and remove noise, (4) The image is high-pass filtered by subtracting a low-pass version of the image, (5) Finally, the contrast of the (inverted) white tracers and black background is enhanced by binarization. Figure 2.19 shows a processed image corresponding to Figure 2.18. It is clear that the seeding materials become more highlighted and background brightness gradients are replaced by uniform darkness. More importantly, this processed image is more like the synthetic image that has been tested. This procedure is performed on all images after rectification and before PIV analysis commences.

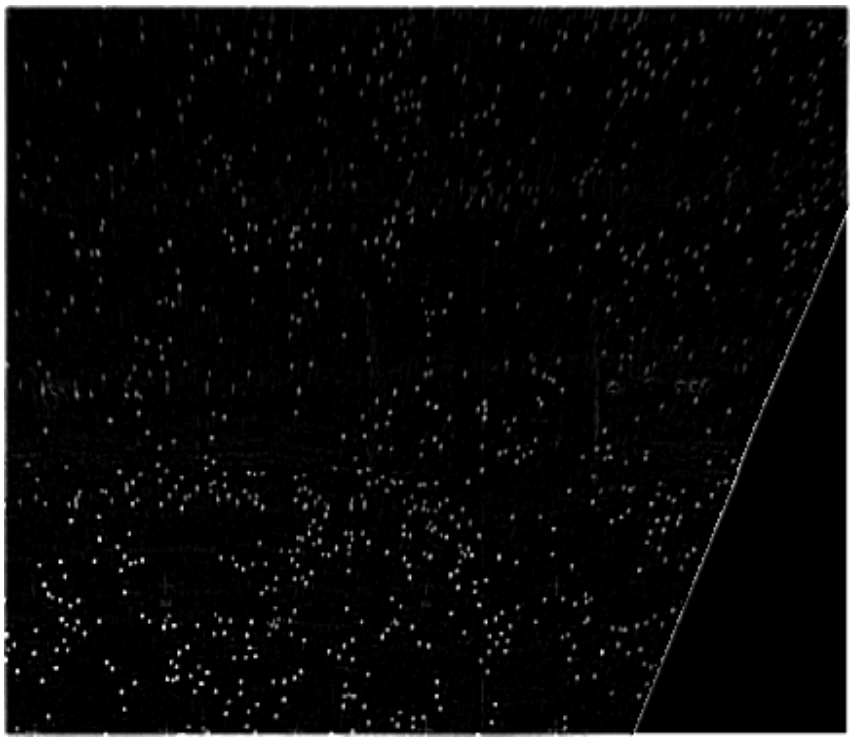

Figure 2.19: Pre-processed image prior to PIV analysis showing the increase in contrast between the seeding particles and the uniform background**.**

Chapter 3

PIV DATA AND VALIDATION

3.1 Experiment Setup

The internal dimension of the experiment basin is approximately 17.2 m in length and 18.2 m in width, the wave maker consists of 34 programmable flap-type wave paddles. The beach consists of a steep 1:5 toe located between 1.5m and 3m from the wave maker with a milder 1:30 sloping section extending from the toe to the wall of the basin opposite the wave maker. Three artificial sandbars are constructed from the HDPE (high density polyethylene) panel. This bar-channel system consisted of three sections: one main section spanning approximately 7.32 m longshore and two half-sections spanning 3.66 m each. Then the designed rip channel is 1.82m wide, centered at ¼ and ¾ of the basin width. The seaward edges of the bar sections were located at approximately x = 11.1 m with the bar crest at x = 12 m and their shoreward edges at 12.3 m. The plan view and the cross section view of the wave basin are illustrated in Figures 2.16 and 3.1 respectively. In our experiment we are interested in a square area covering 2 m to 8.5 m in longshore direction and 9 m to 14 m in cross-shore direction. This basin geometry has been justified by Haller *et al.* [2002] because both the ratio of current spacing to surf zone width and the ratio of rip channel width to rip current spacing falls into the range of field observations. If we consider this basin as an undistorted Froude model of scale 1:50, then the experiment condition corresponds to a rip channel width of 90 m and a rip spacing of 450 m. This channel

configuration produces currents slightly larger than those observed in the field when scaled to prototype conditions [MacMahan, *et al*., 2005], however, the geometry is utilized in the present study following on from previous studies in the basin [see Haller and Dalrymple, 2001, Haas and Svendsen, 2002, and Kennedy and Thomas, 2004 for further details on the basin geometry and bathymetry].

Since PIV records the position over time of image texture within an interrogation window, suitable tracer particles are needed to seed the flow. In field applications, texture provided by surface foam can be used as the tracer. In laboratory studies with clear fresh water, artificial means are necessary. In their particle tracking techniques, Kennedy and Thomas [2004] used plastic swimming pool lane floats (diameter = 0.107 m and thickness = 0.017 m) because they rode low in the water. Those floats are prohibitively large to use for laboratory PIV studies because adequate particle density would require large interrogation windows leading to an overly smoothed flow field. Here, black high-density polyethylene (HDPE) chips (nominally 0.025 x 0.025 m square) are utilized as seeding particles. HDPE is chosen because its specific gravity of 0.96 means that, similar to the Kennedy and Thomas [2004] floats, the chips are only slightly positively buoyant. This enables the chips to travel easily with the currents, but often precludes them from surfing on waves to shore as a tracer with full positive buoyancy would.

Over 40,000 HDPE square chips are used as seeding particles. However, it is impossible to maintain a uniform and constant seeding density within the region of interest over 20 minutes of recording. Prior to generating waves, particles are spread and distributed across the surface within the region of interest as evenly as possible. Rip current formation occurs rapidly after wave generation commences

causing particles to be transported offshore. In an attempt to maintain seeding density, two people are used to continually supply the rip feeder currents with chips. Some of the offshore particles eventually return to the surf zone by Stokes drift, however, the time scale is such that the particles will stay out of the region of interest during most of the recording. Thus, seeding particles are also introduced as necessary in the offshore just outside the region of interest to populate the flow field offshore of the bar. Earlier pilot experiments suggested that the circulation fields associated with the two rip currents were reasonably equivalent and behaving independently; Just before the our experiment, rip currents in the two channels are tested and witnessed to be different in strength. The possible explanation for a stronger rip within the right channel than the left one is a slight alongshore gradient on the basin floor due to the deterioration of the concrete construction. Therefore, the measurement in this study will concentrate on only right half of the basin.

As mentioned earlier, image illumination can be problematic. To overcome lighting problems, white Titanium Dioxide dye is poured into the water and mixed prior to data collection with the help of waves. The purpose of the dye is four-fold: (1) it enhances the contrast of the black particle chips and white water as background, (2) the opaque water diminishes light reflections through waves and off the basin floor, (3) the opaque water renders the meter-spaced ground control points less visible in the PIV imagery, alleviating potential difficulties in pattern matching with fixed targets in the images, and (4) it can also be regarded as scattering material to generate echo, when acoustic current meters are collecting signal. Imagery is collected at night to remove any potential uneven solar effects through laboratory

windows. The basin is illuminated using five 300 W halogen lights with the lighting spread as evenly as possible within the region of interest.

3.2 PIV Data

PIV analysis is applied to laboratory-generated rip current imagery captured at 10 Hz. A total of 20-minutes worth (12000 frames) of rip current images are recorded to observe the initiation, development and temporal variation of the rip current for each run. MFCOR-based PIV is employed to process the data set for its computational efficiency and accuracy characteristics when little noise is present (as is expected given the pre-processing steps described). Following the previous rip current studies in this basin [Haller, *et al.*, 2002], monochromatic waves with a height of 0.05 m, period of 1s and incident angle of zero are chosen. Considering the wave period of 1 s and image capture frequency of 10 Hz, velocity vectors that the PIV technique resolves should be attributed to not only the current but also incoming waves.

A comprehensive description of rip currents was obtained in the laboratory with a longshore bar-trough beach incised by rip channels. Waves are dissipated over the bar, while the waves in the rip channel are larger owing to wave-current interaction, and dissipated closer to shore. Wave set up over the bar profile is larger than within the rip channel, and the resulting alongshore pressure gradient drives the currents alongshore that converge to the region of lower set-up generating a rip current [Haller, *et al.,* 1997].

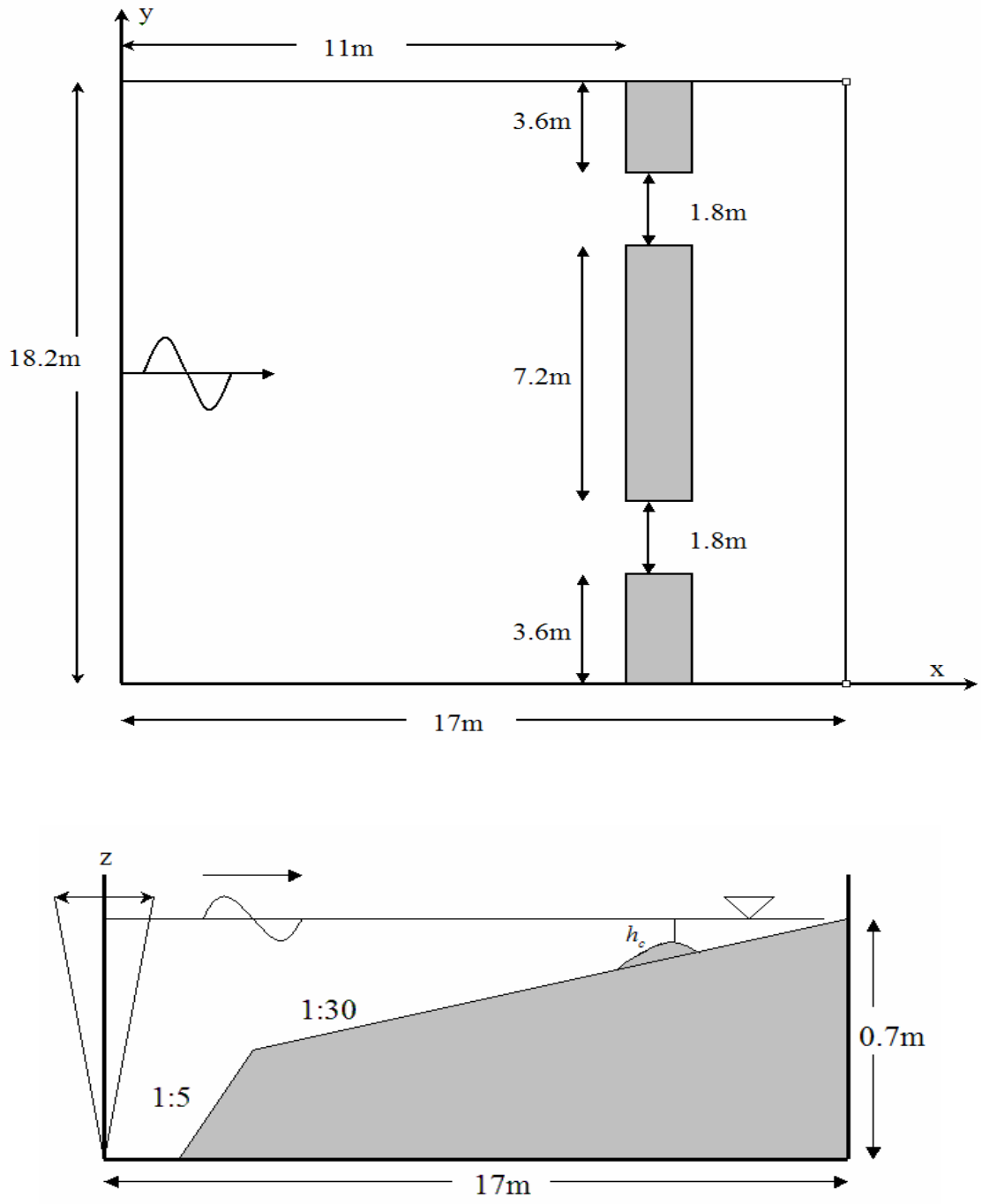

Figure 3.1: Plan and cross section view of the wave basin, gray area is the concrete floor and constructed bar.

A series of PIV vector snapshots are returned after image acquisition, pre-processing, PIV routine and post-processing. Figure 3.2a shows the PIV result of an image pair taken at the beginning of wave generation. By then, no alongshore feeder currents have formed and the PIV results only indicate the incoming waves. Vectors heading onshore or offshore indicate particles moving up and down on the wave crest or trough. At this stage, the lack of a rip is obvious and almost alongshore uniformity of wave crests can be seen. It is similar to what we see visually at the initiation of wave motion. Just 20 s into the simulation a feeder current sets up behind the bar driven by an alongshore water level gradient due to wave breaking (Figure 3.2b). Vectors from both sides of the channel converge in the middle of the channel to form the rip current. Essentially most of the surface velocity vectors within the channel are offshore oriented with a maximum magnitude of 2.5 m s^{-1}. As expected, all vectors near the shoreline are small in magnitude and the instantaneous wave signature is only present where the current is weak such as over the bar. Sometimes during the recording, seeding chips "stick" together and are transported as a group, this will pose problem for PIV processing. Spurious vectors will be smoothed out during the post-processing but if the bunch of particles covers a large area, erroneous estimation of the vector field will be returned for current snapshot. This effect can also be averaged out when the 20-minute mean is taken through out the snapshot series.

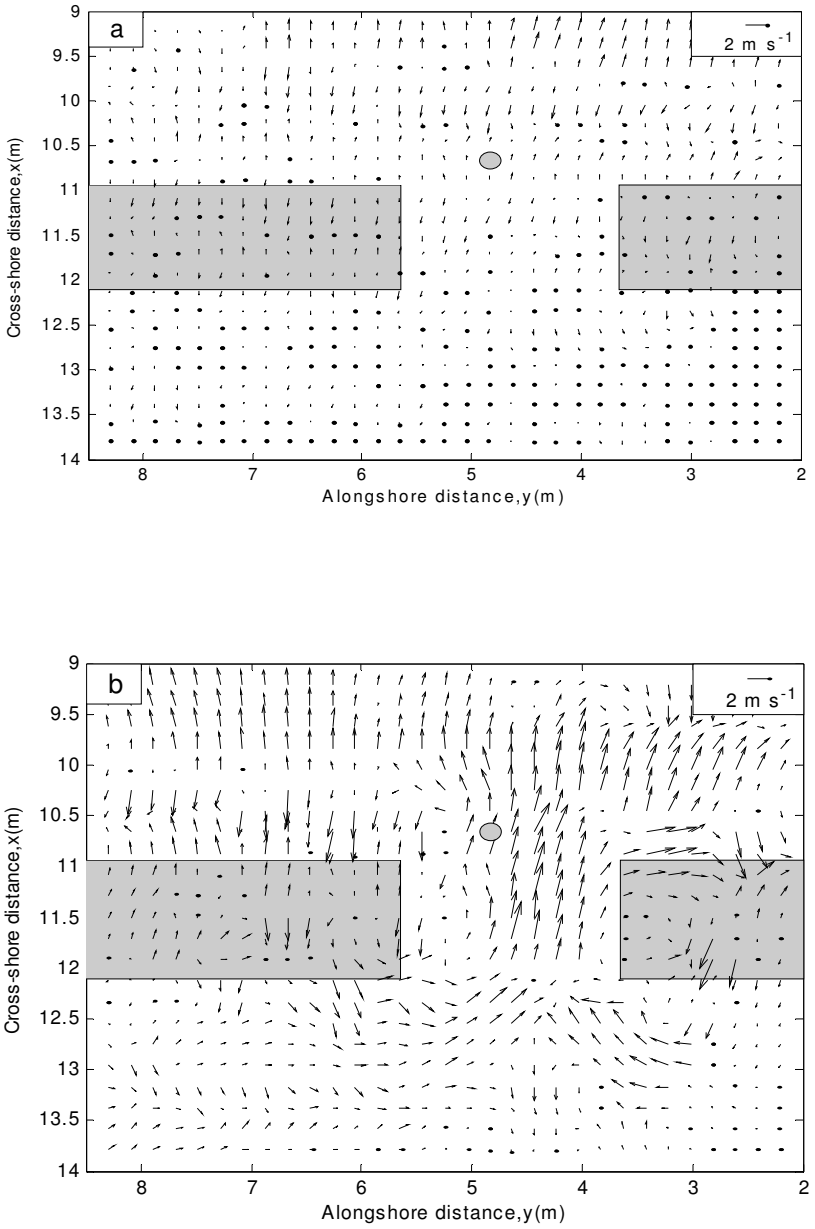

Figure 3.2: (a) PIV flow field at the beginning of wave generation and (b) PIV flow field 20s after wave generation. Upper-right corner shows velocity scale of 2 m s^{-1}. The gray dot indicates the location for the time series shown in figure 10

It is well known that a fluid particle position averaged over one wave period has a net transport in the wave direction that is in addition to any current measured by a fixed current meter. In the previous drifter tracking measurement [Kennedy and Thomas, 2004], Stokes drift must be taken into account when interpreting the results and comparing them with fixed instrument measurement. The Eulerian velocity measurement in Particle tracking technique should always be re-estimated to remove the Lagrangian drift component. Although PIV is also quantifying the movement of seeding particles, Lagrangian drift is not a problem here because instead of following the particles all way through, the interrogation window is fixed and local velocity is sought. In contrast, PIV can give reasonable velocity at each grid point because of its inherent Eulerian nature. Figure 3.3 shows a 5-minute velocity time series at one location just outside the channel (for specific location refer to the dot in Figure 3.2). A 1-second running average filter using a boxcar window in an attempt to remove the wave effect is superimposed. The cross-shore velocity initially oscillates around zero before rip current circulation has set up. After 20 seconds, the cross-shore velocity has a steady tendency of being negative, implying a fairly persistent offshore flow. The mean cross-shore surface flow velocity for these 300 seconds is –0.16 m s^{-1}. Although the grid point is just outside the channel, it still experiences small variations in alongshore flow with a mean of 0.05 m s^{-1}. These oscillations are due to the meandering of the rip current.

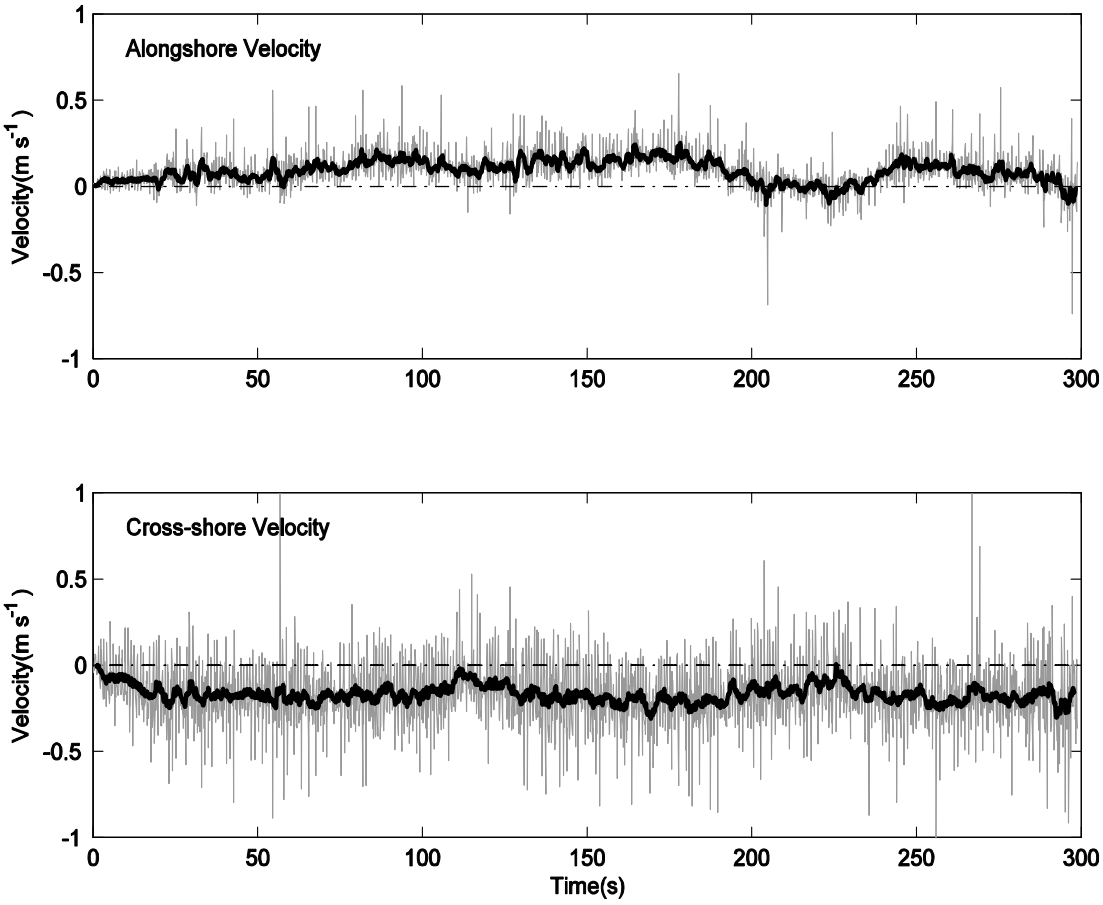

Figure 3.3: Five-minute velocity time series (gray) and 1 second running average (black) at a location just outside the rip channel (see Figure 3.2). The upper panel is alongshore velocity and the lower panel is the cross-shore velocity component. Negative values for the cross-shore velocity are offshore-directed

3.3 PIV Repeatability

The repeatability testing of PIV technique is conducted under the same experiment conditions. Since the density and coverage of the seeding particles cannot be maintained to be constant within each run, there is no point to compare the instantaneous snapshot sequentially. In addition, the presence and absence of unsteady wave forcing will generate ever-changing surface flow structure. Even under the identical wave condition and the measurement is undertaken at the same location, the rip behavior has remarkable variation. A more practical approach is to compare the twenty-minute mean of the velocity magnitude. Twenty minutes is sufficient for averaging the unsteadiness observed on many temporal and spatial scales. During the two separate runs, we use the same experiment characteristics of wave height of 0.05 m, fully incised rip channel geometry and same shoreline location and water depth. Other image acquisition parameters such as shutter speed, angle of view and camera orientation are also kept unchanged. Figure 3.4 shows a magnified comparison of some selected grid points, the root mean square (RMS) difference of magnitude between successive runs on the same topography are listed beside them. It is apparent the regions with strong current have less velocity difference and the locations more subject to wave fluctuations had significant discrepancy in velocity magnitude. Statistically, the overall RMS deviation throughout the domain is 12.6%, which is acceptable considering they are not measuring exactly the same process. Figure 3.5 shows the twenty-minute mean flow field for the two runs.

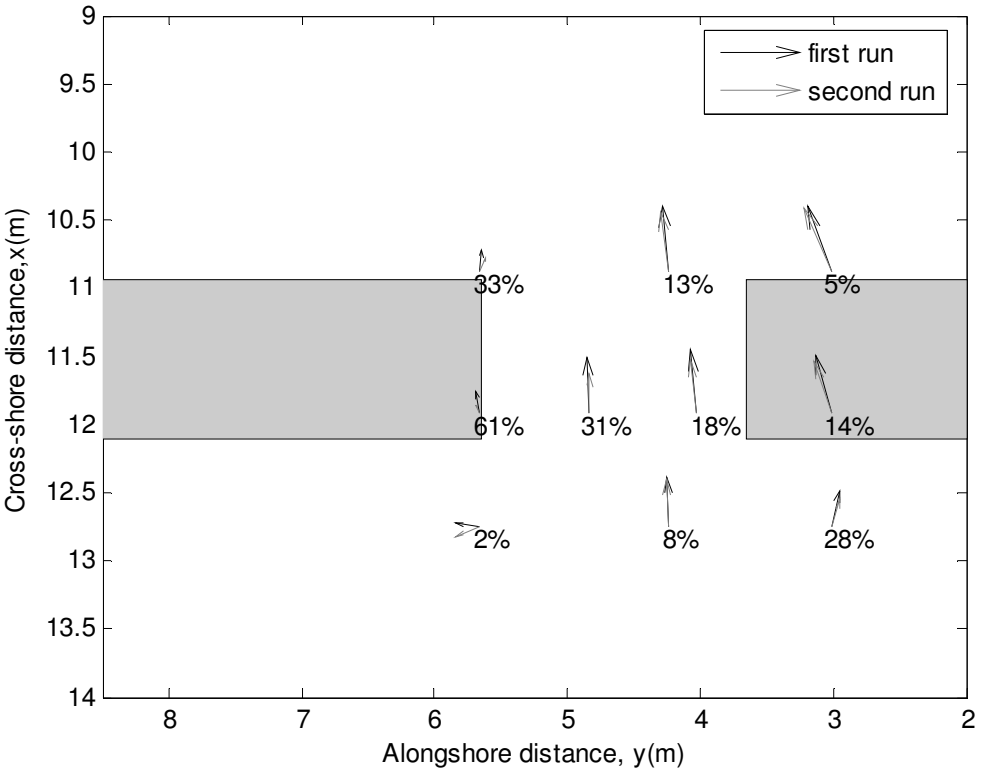

Figure 3.4: Velocity magnitude comparisons at 10 discrete locations over the bar, within the channel, offshore and onshore the bar. The vectors are magnified to a scale for comparison

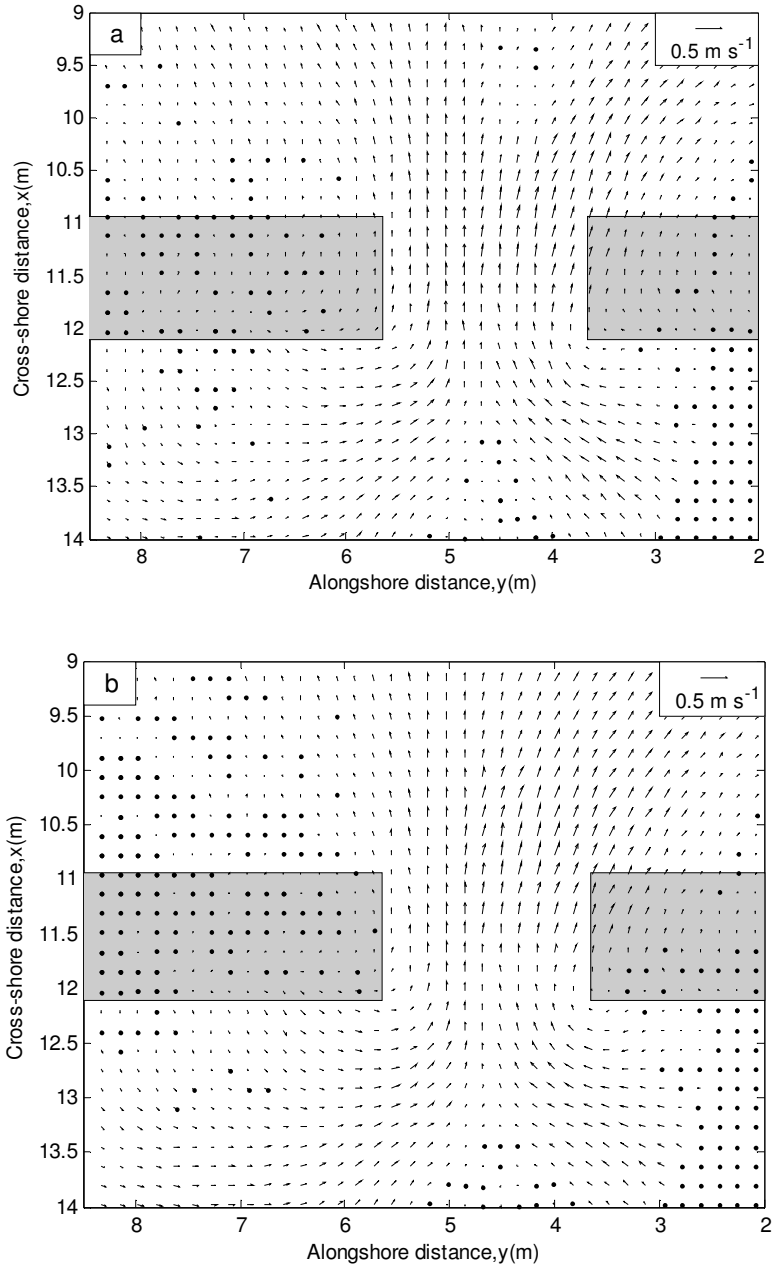

Figure 3.5: Twenty-minute mean of the flow field series for to separate wave runs holding all parameters constant; (a) first run and (b) second run. The arrow at the upper right corner is 0.5 m/s

3.4 PIV Validation

Acoustic Doppler Velocimeters (ADV) were deployed within and near the rip channel in an attempt to compare in situ measurements with PIV estimates. Care is taken to extract PIV velocity information at the same horizontal location where the current meter is installed since PIV and ADV data collection typically requires separate runs. The current meter is installed under the trough level to insure it does not emerge from the water column. The fact that PIV returns surface velocity and the ADVs are installed near mid-water depth complicates a direct quantitative comparison, but no other practical means exist. Figure 3.8 shows the cross-shore distribution of the time-averaged cross-shore velocity component measured at four locations within the rip channel by PIV and ADV separately. The wave condition here is 0.05 m wave height and the topography is fully incised rip channel. Both methods returned an offshore current at the surface and below the surface. As expected, mean ADV velocities were of smaller magnitude than the surface PIV estimates in conjunction with the vertical variation in cross-shore velocity observed by Haas and Svendsen [2002]. Stokes drift is also calculated at these four locations based on the 20-minute averaged wave height and local bathymetry as approximately 0.04, 0.12, 0.08, 0.06 m s^{-1} moving from offshore to onshore. However, unlike PTV or other tracking techniques, surface Lagrangian wave drift does not need to be subtracted from PIV to yield the Eulerian velocity since the aim of PIV is to extract the instantaneous local flow field. In addition, previous studies using PIV in wave-dominated regions reported the PIV-estimated velocities without any corrections for Stokes drift [Chang, *et al*., 1997; Gary, *et al*., 1988], further suggesting the Eulerian nature of the technique even in wavy environments.

In order to obtain a more time sensitive comparison between the ADV and PIV, an additional run was undertaken. In another run with 0.05 m waves and fully incised channel, PIV and ADV data are collected simultaneously. Multiple ADVs could not be used because the presence of fixed objects in the imagery tends to obscure PIV. It's also our intention to remove all the unnecessary objects in the field of view and only a single ADV was installed in the channel. The wood designed to hold the ADV stem is unavoidable, so the interrogation window at the other side of the ADV is not applicable. Unable to obtain the PIV velocity information at the exact ADV location, the three closest PIV-derived velocities whose interrogation windows did not overlap the actual current meter were used (shown in Figure 3.6). Based on the continuity assumption in PIV post-processing procedure, the exact PIV surface velocity at the ADV location can be interpolated with its surrounding vectors. The three time series were spatially averaged and used as the time series for one-to-one comparison.

In attempt to initiate PIV and ADV exactly at the same time, two people are needed to implement a simultaneous operation. Because the PIV image capture and ADV signal sampling are logged into two different computers, the human induced delay and error is inevitable. Cross-correlation is applied to the acquired two time series and PIV data is re-sequenced according to the peak of cross-correlation of cross-shore velocity (Figure 3.8). Cross-shore velocity is chosen because weak current signal and mostly wave fluctuation in alongshore velocity makes no obvious correlation peak. Figure 3.9 shows the alongshore and cross-shore velocity comparison of ADV and PIV time series of twenty minutes and two-minute segment of that time series starting at the 6^{th} minute is selected to illustrate the simultaneous comparison

(Figure 3.8, again from the location shown in Figure 3.2). It can be seen that both alongshore velocity and cross-shore velocity exhibit similar trends and both of the recordings discern the low-frequency meandering of the rip current in the alongshore direction and persistently strong flows in the cross-shore direction. PIV shows smaller alongshore velocity amplitudes probably due to some smoothing inherent in the method. The r^2 correlation coefficient in the alongshore comparison was only 0.13 while that in the cross-shore was 0.45 after alignment. Alongshore mean velocities and standard deviation are 0.0185±0.13 m s^{-1} (ADV) and 0.0013±0.08 m s^{-1} (PIV), showing negligible mean alongshore current just outside the channel with significant meandering of the rip head. Cross-shore mean velocities are -0.1355±0.17 m s^{-1} (ADV) and -0.1530±0.17 m s^{-1} (PIV), indicating a difference of roughly 10% in mean velocity and similar variability. Spectral analysis was performed using these four time series. Both PIV and ADV show a frequency component of O (1s), which is attributed to the presence of waves, and a low-frequency oscillation with a time scale of O (200s) that has been previously observed in rip current studies in this basin under similar conditions [Haller *et al*., 2001; Kennedy and Thomas, 2004]. Although the time series show good correlation in a mean sense and for spectral peaks, the low r^2 correlations between PIV and ADV would seem to indicate poor PIV performance. However, it is expected that the largest source of the difference between the 2 sets of time series arises from unavoidable measurement discrepancy at different elevations (PIV at the surface and ADV near mid water depth). Thus, even though only moderate correlation is found for the cross-shore velocity in the comparison to the subsurface ADV signal, we believe the technique is robust in extracting surface current information.

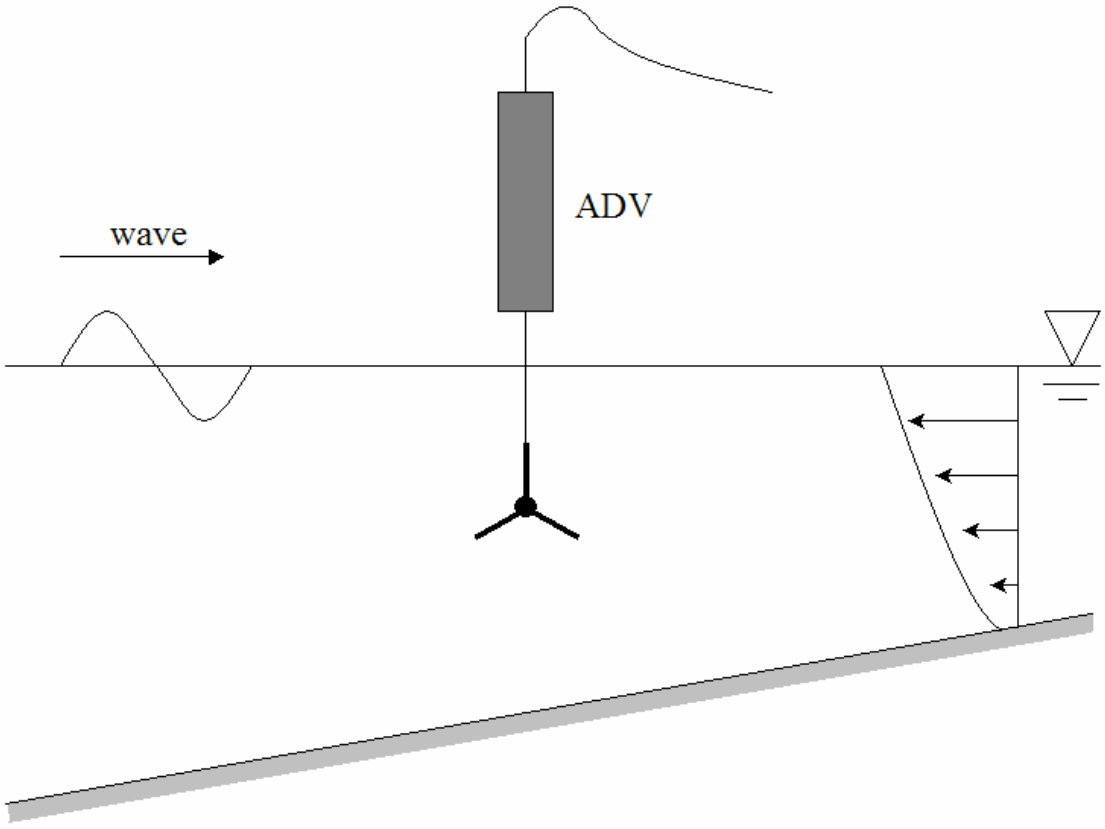

Figure 3.6: Illustration of the ADV installation, it consists of High-Frequency cable, Signal conditioning module, and ADV sensor

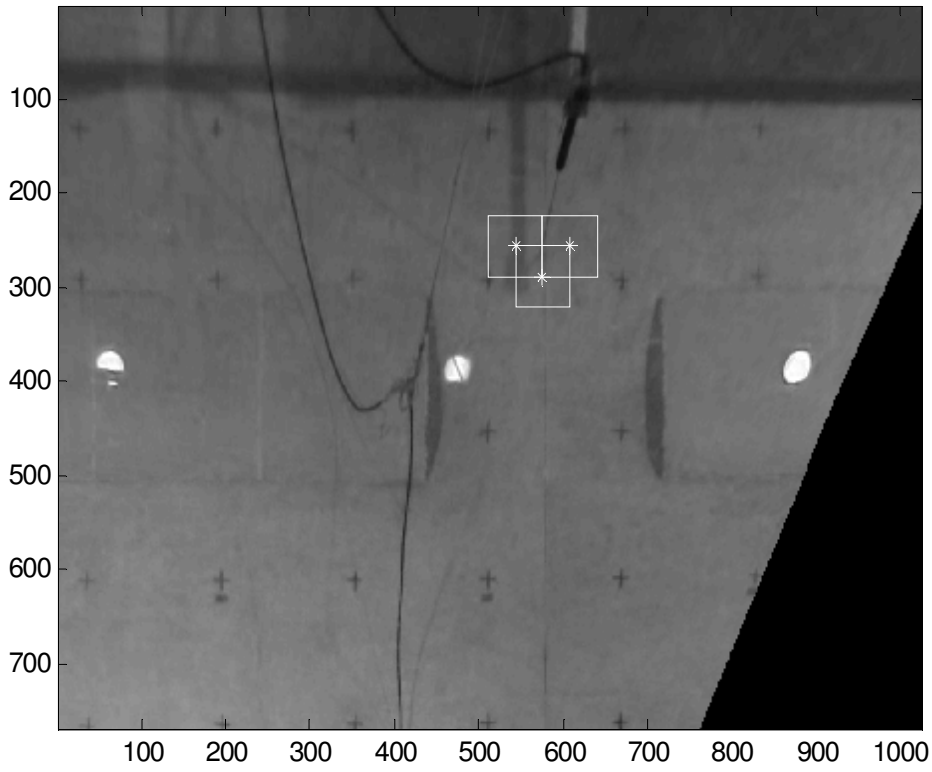

Figure 3.7: A snapshot of rectified image with ADV in the view, x and y axis are in pixel coordinate. The three white squares denote the neighboring interrogation windows surrounding ADV and asterisk denotes the center of the window surrounding the sampling volume

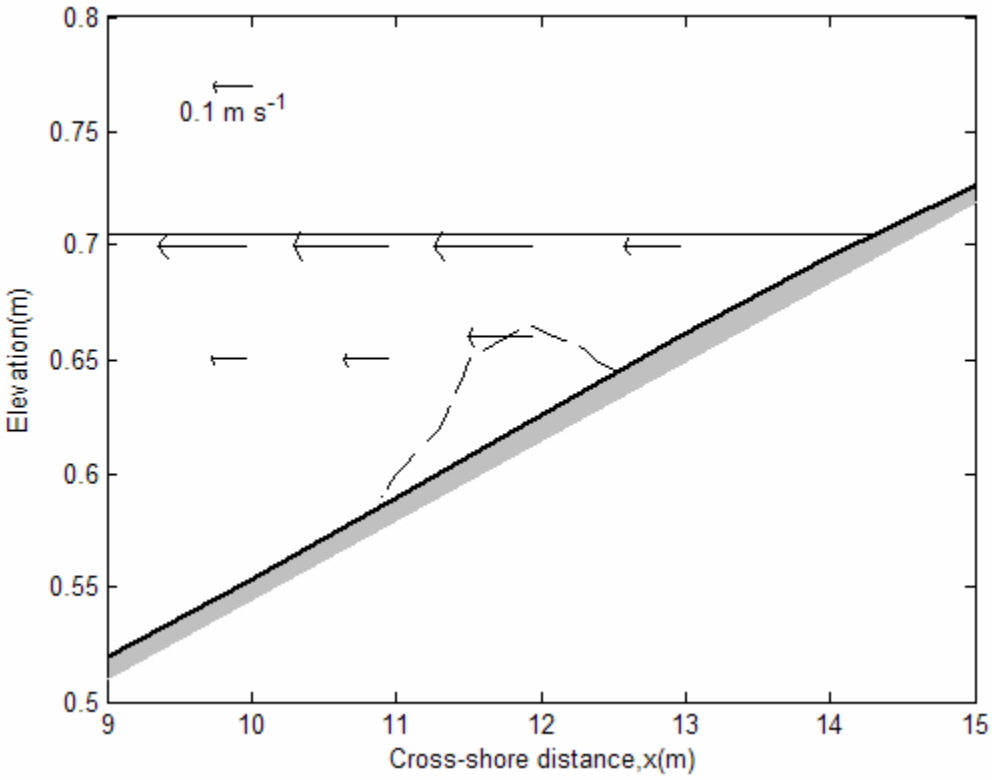

Figure 3.8: Time-averaged cross-shore velocity component from the centerline of the rip channel measured by ADV (lower vectors) and PIV (upper vectors plotted just below still water level).

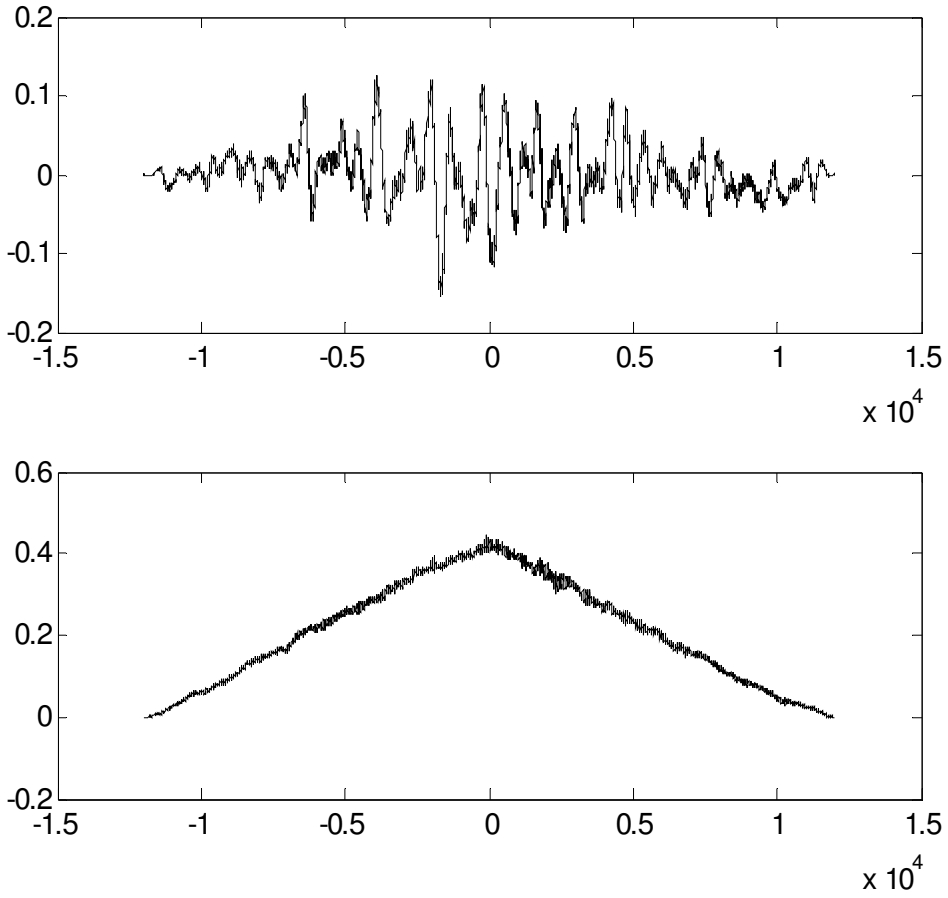

Figure 3.9: Cross-correlation coefficient of alongshore velocity (upper) and cross-shore velocity (bottom). The horizontal axis in both figures is sampling data number at 10 Hz and the vertical axis is cross-correlation coefficient.

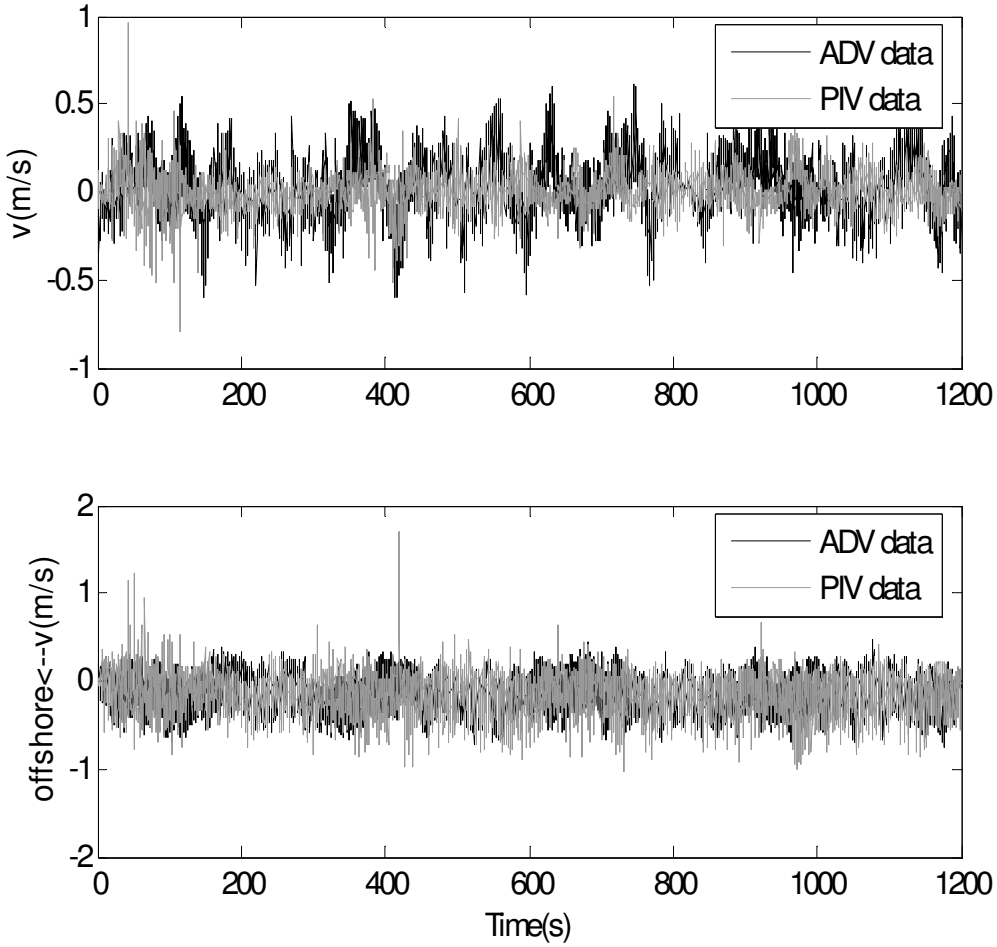

Figure 3.10: Twenty-minute time series of alongshore velocity (upper) and cross-shore velocity (lower) after

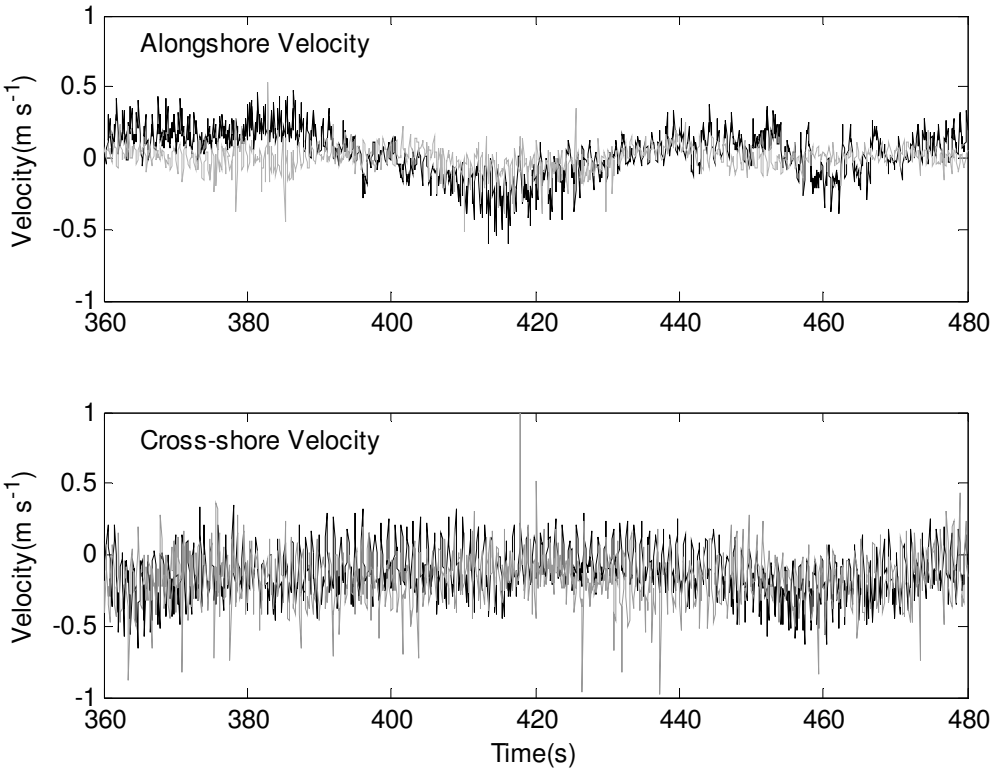

Figure 3.11: 2-minute time series of PIV (gray) and ADV (black) recording starting at 6th minute of the twenty-minute run. Upper panel is alongshore velocity and lower panel is the cross-shore velocity component. Negative values for the cross-shore velocity are offshore-directed

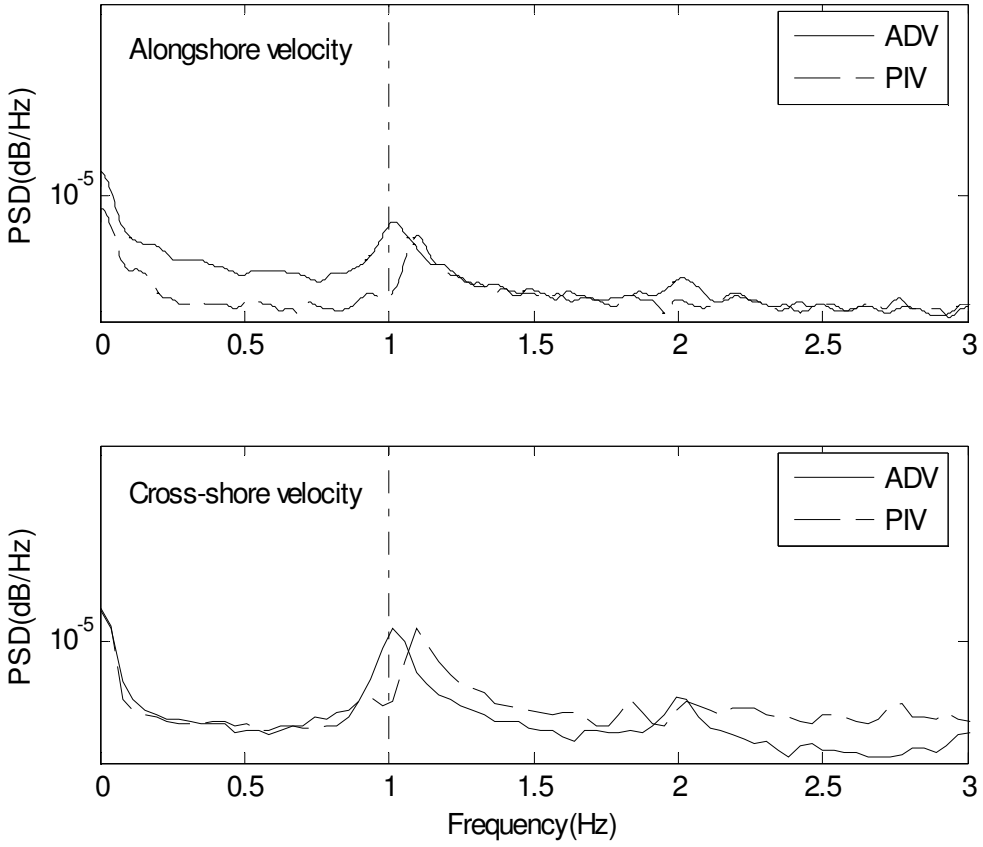

Figure 3.12: Power spectrum of the twenty-minute long time series corresponding to the data in Figure 3.10, the power spectrum is estimated using Welch's method, in which 256 is the sample window length, 32 is the overlapping length

Chapter 4

FLOW FIELD OVER VARIABLE BEACH TOPOGRAPHY

4.1 Variable Rip Channel

Early qualitative observations suggested that the rip currents were coupled to the morphological change and that velocities increase with increasing wave height [Shepard, 1936; Shepard and Inman, 1950; McKenzie, 1958, Bowman, 1988]. Recent studies have increased both spatial and temporal resolution of the observations with greater accuracies and have quantified earlier qualitative assessments. Complete rip current experiments require three types of measurement data, assuming the conditions exist or the generation of rip currents; 1) comprehensive measurement within the rip channel and neighboring shoal, 2) accurate measure of the bathymetry, and 3) offshore directional wave measurements. Considerable difficulties are encountered in an attempt to obtain all three of these measurements simultaneously. In our study, the bathymetry is fixed once it is created. Offshore wave measurement is also conducted and calibrated before each run. The problem lies in the fact that we are unable to obtain vertical varying velocity within the channel because of the ADV's interference on PIV images. Consequently, our measurements for laboratory rip currents are collected in a piece-wise manner.

Recent laboratory experiments have been used for theoretical verification and for interpretation of field measurements [Hamm, 1992; Haller *et al.*, 1997, Haller and Darymple, 2001; Haller *et al.*, 2002]. Most field observations of rip currents are

associated with incised rip channels in shore-connected shoals or depressions on near-planar beaches. While some laboratory simulations produce rip currents with directional waves producing a converging current and a return flow, most laboratory measurements have been conducted with an alongshore bar-trough system cut by a rip channel [e.g., Kennedy and Thomas, 2004; Haas and Svendsen, 2002].

Previous research on rip currents conducted in the wave basin at University of Delaware use the topography described here with the rip channel incised down to background slope [e.g. Kennedy and Thomas, 2004]. Many tests were undertaken by varying the wave period, depth over the bar, and wave height to examine general rip behavior and sometimes the unsteady properties of the rip current even in absence of unsteady forcing. However, all of these tests are based on a fixed topography, which exaggerates the rip channel incision and is atypical of most field rip channels. If we consider the experimental basin as an undistorted Froude model of the field conditions with a length scale ratio of 1:50,

$$Fr = U_r / \sqrt{gh} \tag{4.1}$$

where U_r is the velocity within the rip channel and $\sqrt{gh}$ is equal to the wave group velocity or phase speed in the shallow water [Haller, *et al.*, 2002]. The measured laboratory rip current in previous experiments within the channel ranges between 0.1-0.2 m/s. Then, the actual rip current we are mimicking is about 1 m/s. The breaking wave height would range from 1.5-3.5 m. Similarly, the modeled beach topography would correspond to a rip channel width of 90 m, a rip spacing spanning 450 m and a rip channel incision of 3.9 m. However in the field, topography is ever-changing and rip channels are often more subtle relative to the alongshore bar. Variable alongshore beach topography has been numerically modeled by Slinn *et al.* [2000]. To simulate

the barred beach profile similar to topography measured at Duck, North Carolina as a part of the DELILAH field experiment, they created an alongshore uniform bar and perturb it with sinusoidal alongshore variation with amplitude ε and wavelength λ (shown in Figure 4.1). 0-1m rip incision relative to a rip spacing of 124m makes our modeled standard rip channel (Figure 4.2) significantly deep.

Thus, in our study, we are trying to decrease the channel incision depth and are interested in the variable dynamics of the rip current in relation to variable topography. As shown schematically in figure 4.3, three types of artificial rip channels are all made of HDPE and shaped similar to the main sand bar. At the edge of bar, cement "end caps" are built for the purpose of smoothing the junction between the sand bar and altered incision to reduce wave reflection. The height of the crest of the sand bar, h, is 7.8 cm. The modified channels reduce the incision to 1/3 and 2/3 the original incision yielding maximum channel depths of amplitude of 2.57 cm and 5.23 cm respectively. Similarly, consider a Froude model with a length scale ratio of 1:50, our topography can be considered as modeling the prototype of a rip incision of 1.26 m and 2.65 m.

Repeatability tests have been performed for all the three types of topography set ups, similar to section 3.3. To test the repeatability of the bar-trough construction and PIV as well, the 1/3 and 2/3 bars were removed after the first PIV run. Statistically, the overall 20-minute RMS deviation throughout the flow field of fully incised rip channel is 12.6%, 2/3 incised rip channel is 7.1% and 1/3 incision is 12.4%.

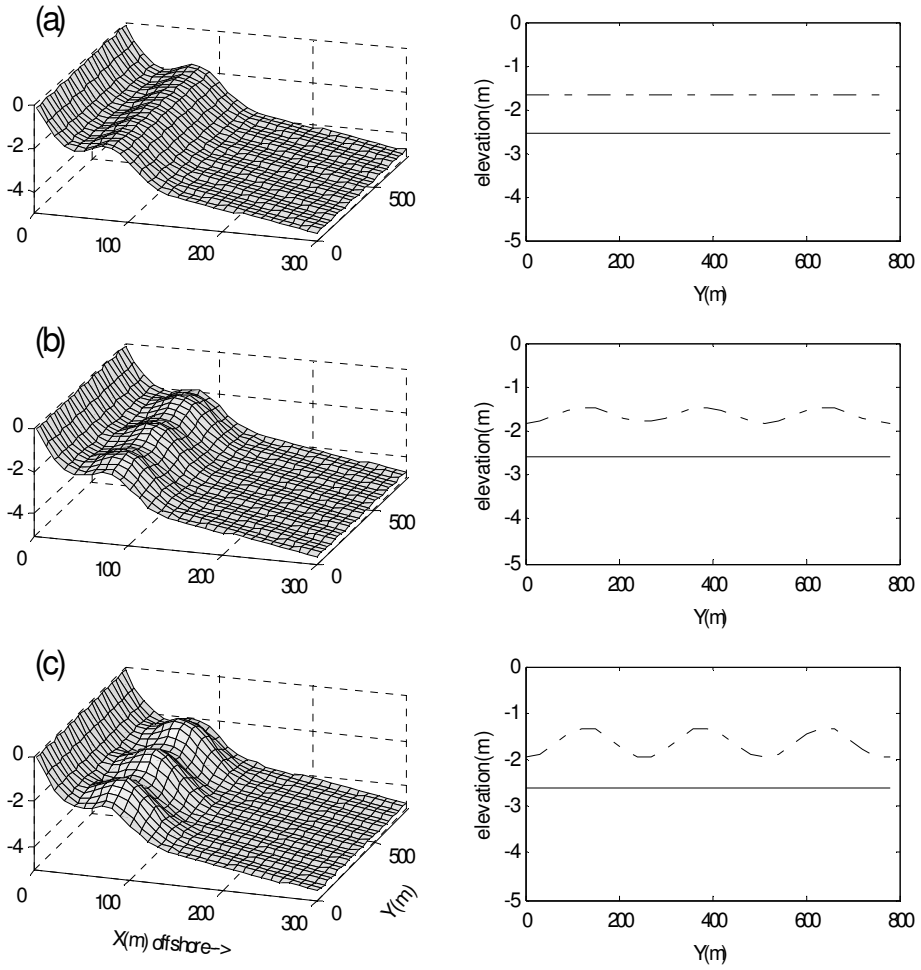

Figure 4.1: Beach bathymetry for a barred beach with alongshore variations for (a) ε=0.0, (b) ε=0.1 and (c) ε=0.2 and wavelength is 124 m.

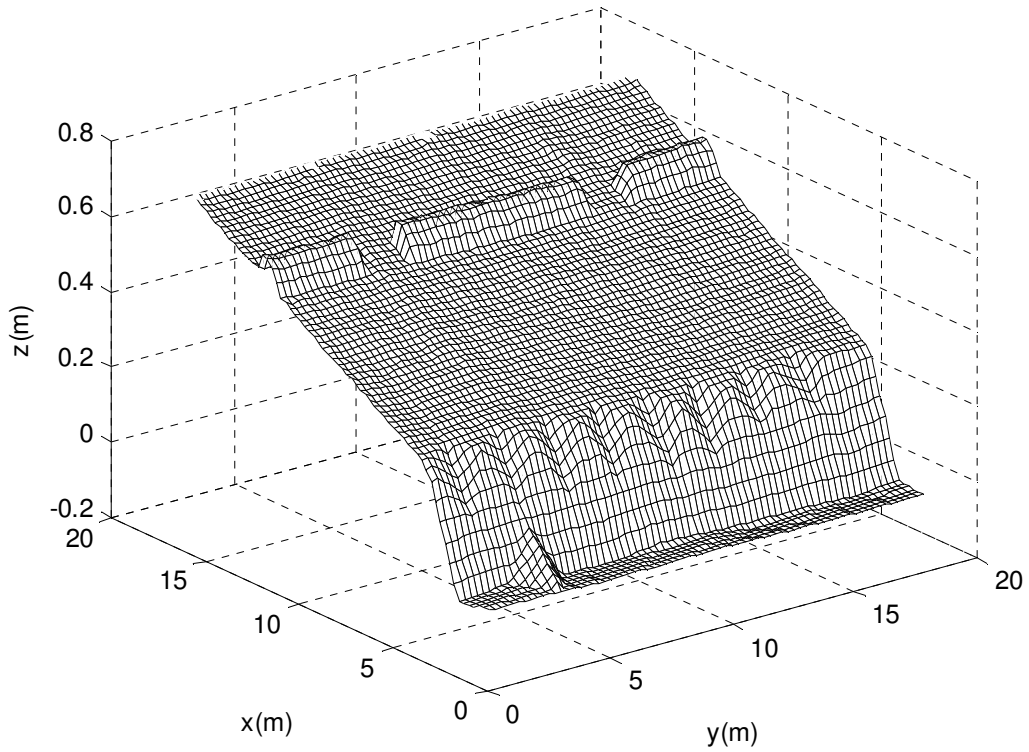

Figure 4.2: Topography plot interpolated for a fully incised rip channel from a previous survey

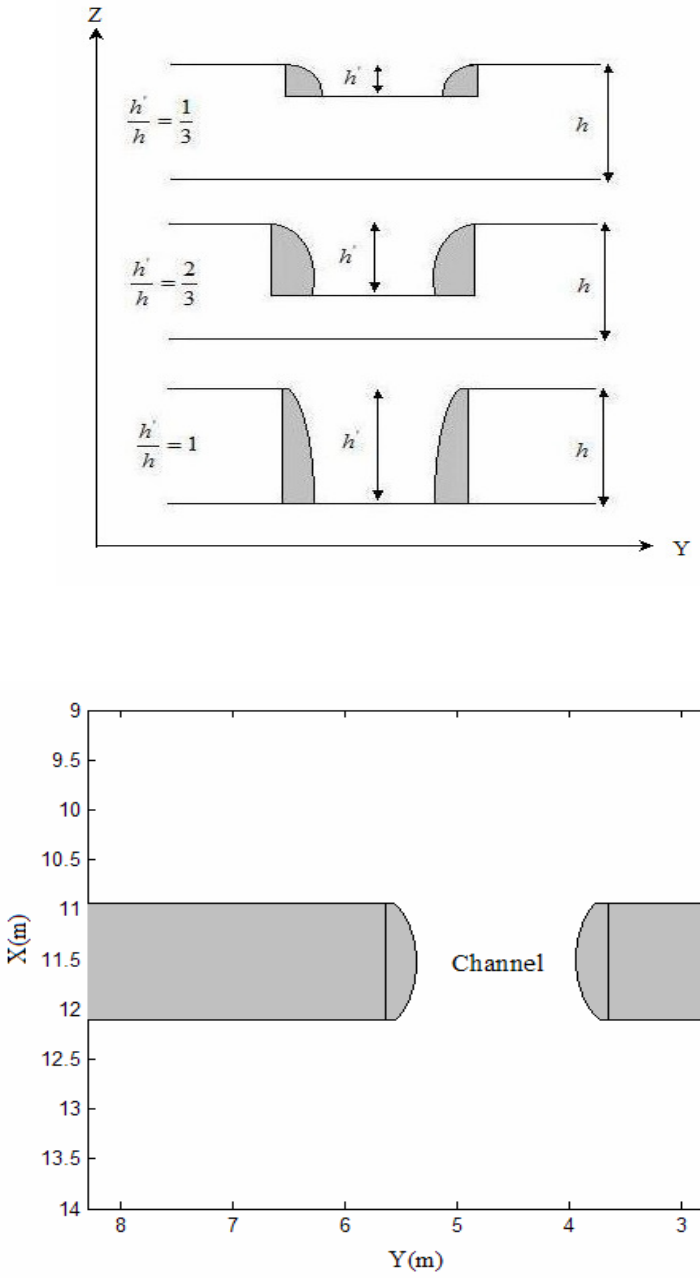

Figure 4.3: (a)The side view of the variable incision depth relative to the original bar height. h' is rip channel incision depth and h is the bar height, gray area denotes the cement slope. (b) The plan view of the area of interest, the gray area is the bar and cement.

4.2 Rip Currents Scaling

The mean velocity of rip currents varies with different beaches and different incoming wave forcing, as well as tidal elevation. The tidal elevation effect has not been addressed in our study since the still water level over the bar and the location of the shoreline are maintained throughout all runs. The Froude number $U_r / \sqrt{gh}$ provides a dimensionless measure of rip current flow, which is defined in Equation 4.1. Previous field and laboratory data indicates the rip current strength increases with increasing wave height and decreasing water level. Thus, here the wave forcing is parameterized with dimensionless variable H / h (wave height/water depth). In previous experiments, the parameterized water depth is taken as the depth over the crest of the bar. Macmahan *et al.* [2005] did the same for the field measurements. For consistency, we compare our data with the dynamic scaling of the previous observations, both in laboratory and field. From figure 4.4, we can see our data basically falls into the scattering of field data, which indicates a nearly linear relationship between the dimensionless wave forcing H / h and dimensionless rip current strength $U_r / \sqrt{gh}$.

Wave current interactions affect the wave height within the rip channel, where an increasing current leads to increasing wave heights owing to wave steepening, until wave breaking occurs. MacMahan *et al.* [2005] define the following classification of rip currents, low, intermediate, and high energy systems, which are related to wave-current interaction and inversely related to the wave energy within the rip channel. All available data and our experiment data are combined to assess the importance of wave current interaction (Figure 4.5). Low energy rip currents have

minimal wave-current interaction. An example of this is NCEX, where the rip morphology is subtle and the wave energy was relatively low. Observations most commonly fall within the class of intermediate energy rip currents that have moderate wave-current interaction. Increasing the wave height (without breaking) within the rip channel creates a negative feedback on the system, because the radiation stress gradients develop a counter torque that opposes the pressure gradients. Yu and Slinn [2003] also suggest a negative feedback for wave breaking in the rip channel based on numerical models. When the current becomes fast enough, wave breaking occurs within the rip channel and the opposing radiation stress is reduced and a positive feedback mechanism occurs, increasing the rip current flow. Therefore, the larger the wave height in the rip channel, the larger the opposing force. Haller and Dalrymple observed breaking for all of their cases but the wave heights were generally larger within the rip channel and broke closer to shore, except for their case D, which had intense wave breaking. High-energy rip currents have significant wave-current interaction inducing significant wave dissipation. This case is hypothesized to represent a mega-rip. For each of these three cases, the forcing and feedback varies.

From the kinematic scaling plot, we can see there was a division between the field and laboratory measurements around $U_r / \sqrt{gh} = 0.17$, with field measurements occurring for smaller Froude numbers. The importance of wave-current interaction within the laboratory has greater significance than documented in field measurements, thus far. From Figure 4.5, we can see the wave-current interaction in our experiment approaches the field data more than other experiment, which suggests our variable geometry as a closer simulation of the field dynamic system.

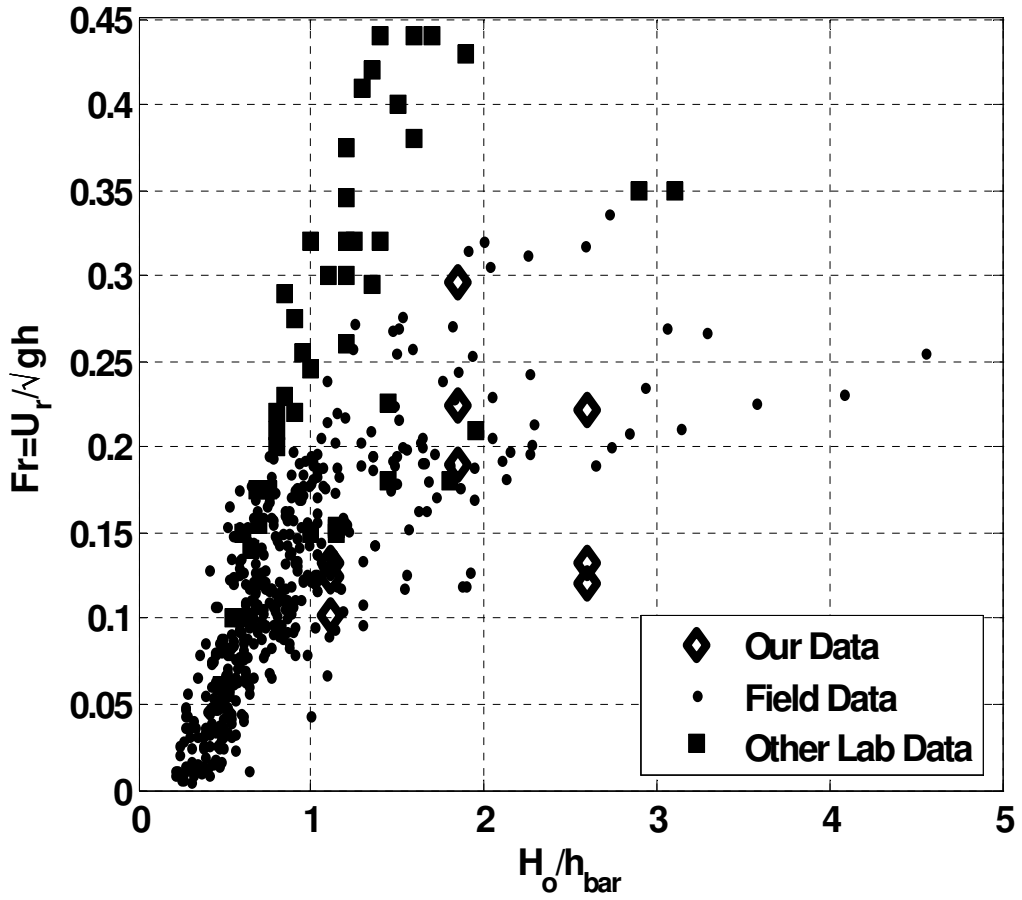

Figure 4.4: Dimensionless return flow, *Ur,* as function of H / h_{bar} from laboratory [Dronen *et al*., 2002, Haller *et al*., 2002] and field data [MacMahan *et al*., 2005]

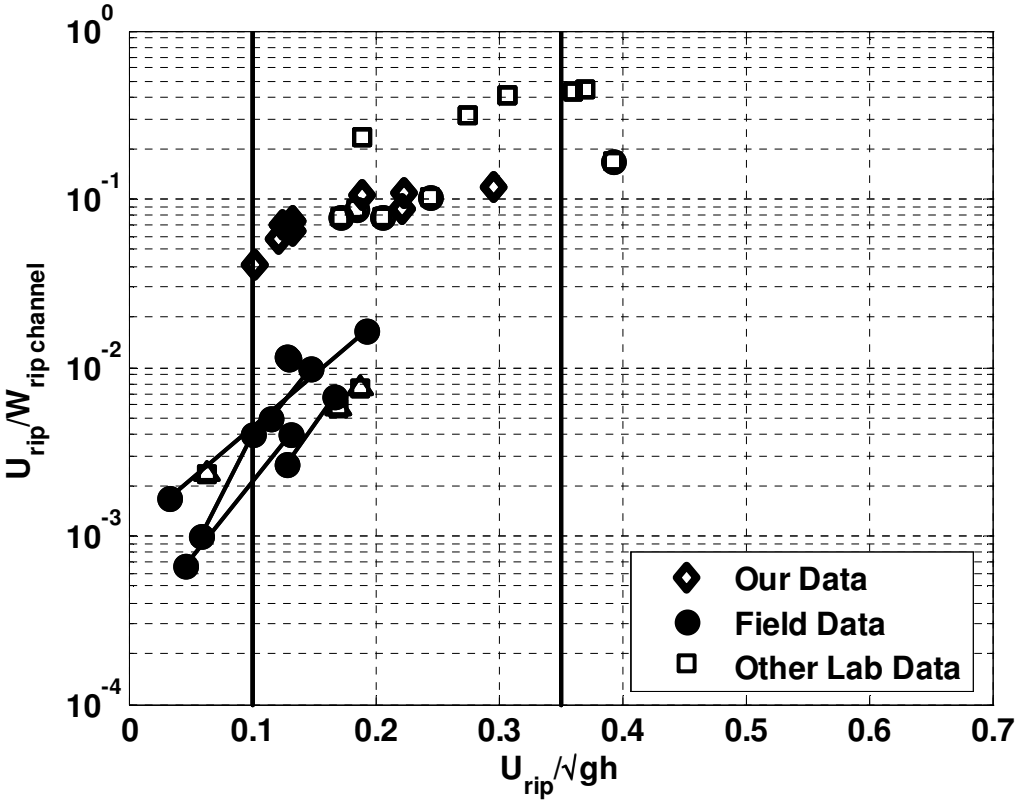

Figure 4.5: Strength of rip current measured by Froude Number, $Fr = U_r / \sqrt{gh}$ versus shear of rip current $U_{rip} / W_{rip-channel}$. Lines connecting symbols represent the relative minimum and maximum values during the experiment. Bold diamonds represent the data in our experiment and bold dashed vertical lines divide the data into low, intermediate and high-energy rip current regimes. The locations for the field data include Skalligen, Danmark [Aagaard *et al.*, 1997], Palm Beach, AU [Brander, 1999], Murawai [Brander and Short, 2000], Torrey Pines [MacMahan *et al.*, 2005], Monterey [MacMahan *et al.*, 2004], Moreton Island [Callaghan *et al.*, 2004] and Sea Grove [Sonu, 1972]. Other laboratory data includes Haller, *et al.*, 2002, Dronen *et al.,* 2002, Hamm, 1992

4.3 Averaged Flow Field of Variable Rip Currents

One remarkable advantage of Particle Image Velocimetry is its ability to obtain the whole surface flow field measurement. In our experiment, the instantaneous velocity measurement at every grid point can be averaged over the 20-minute record to yield the time-averaged flow field. Although we use a large of seeding particles, particles may remain out of the field of view for significant periods of time. Thus we cannot routinely collect time series longer than 20 minutes. However, long period oscillations (~25 min) have been noted in previous experiments [Haller *et al.*, 2002], that we cannot capture with our data collection procedure. The fact that the sampling may be extracted from part of a long process with an unknown trend, implies our 20-minute averaged value is probably slightly affected. The approximate time-averaged RMS error in mean velocity caused by a long-term variation can be calculated as following. Assume the velocity oscillation is of form

$$u' = A\cos(\sigma t + \varepsilon) \tag{4.1}$$

and a record length T, its ensemble-averaged RMS would be

$$\langle \delta u \rangle = A\sqrt{1-\cos\sigma T}\,/\,\sigma T \tag{4.2}$$

where σ is the radian frequency of velocity oscillation. Thus, assuming a 25-minute oscillation, the worst case scenario, the RMS error in computed mean velocity will be around 0.17 of the amplitude of oscillation, for a recording length of 20 minutes. For shorter oscillation periods, error decreases quickly. If oscillations are very long, errors are not negligible, but neither do they seriously imperil the computation of mean velocities.

Figure 4.6 shows the 20-minute time-averaged flow field under two different wave conditions and different topography. Three basin geometries and three incoming wave heights generate nine case scenarios, with each of them representing a particular wave forcing and morphology. In all, nine panels of 20-minute flow field are obtained for each case, but only two representative of them are shown here. With the wave oscillation, rip instability and occasional meandering of rip necks averaged out, most averaged flow fields approximately follow the same pattern. The dominating offshore current through the rip channel is present for all runs and feeding currents onshore of the bar are also visible. There is no obvious flow on the bar and the areas onshore and offshore of the bar away from the channel. The resultant small flow velocity can either be attributed to the presence of turbulence or the fact that all the motion of particles is projected onto the still water level, which is a slight deviation from its actual position on the free surface. Generally, the averaged flow velocity throughout the domain are all less than 0.2 m/s, which are comparable to averaged measurement of most cases in Kennedy and Thomas [2004].

Two typical cases are selected to demonstrate the variable rip currents, shown in Figure 4.6 and 4.7. In the case of 0.03 m wave height and 1/3 incision in Figure 4.6, there is an apparent secondary circulation in the nearshore area. This phenomenon probably could be explained by the smaller wave forcing and smaller alongshore gradient, which initiate a weaker alongshore feeding current and the incoming broken wave will 'push' against the rip to be a counter-rotating circulation pattern on an irregular basis. Visually, particles in this experiment were seen remaining near the shoreline for longer time, until they are circulated to the onset of offshore current. For the area offshore of the bar, the vectors of small magnitude

heading onshore should be partly attributed to the deviation of actual particles floating on the free surface and their projection we convert to the still water level. The similar counter-rotating circulations occur occasionally in other runs, and probably are averaged out because of their short-term characteristics. With the same topography but higher wave height of 0.05 m shown in the Figure 4.7, no secondary circulation is seen. Taking the mean of the flow field of the 12,000 snapshots, the short-term turbulence and the irregular rip head oscillation are all averaged out and a typical rip current flow pattern is left. It can be seen there is a significant oblique offshore flow out of the rip channel. This is probably partly due to the slight alongshore slope present in the basin and the presence of a basin wall.

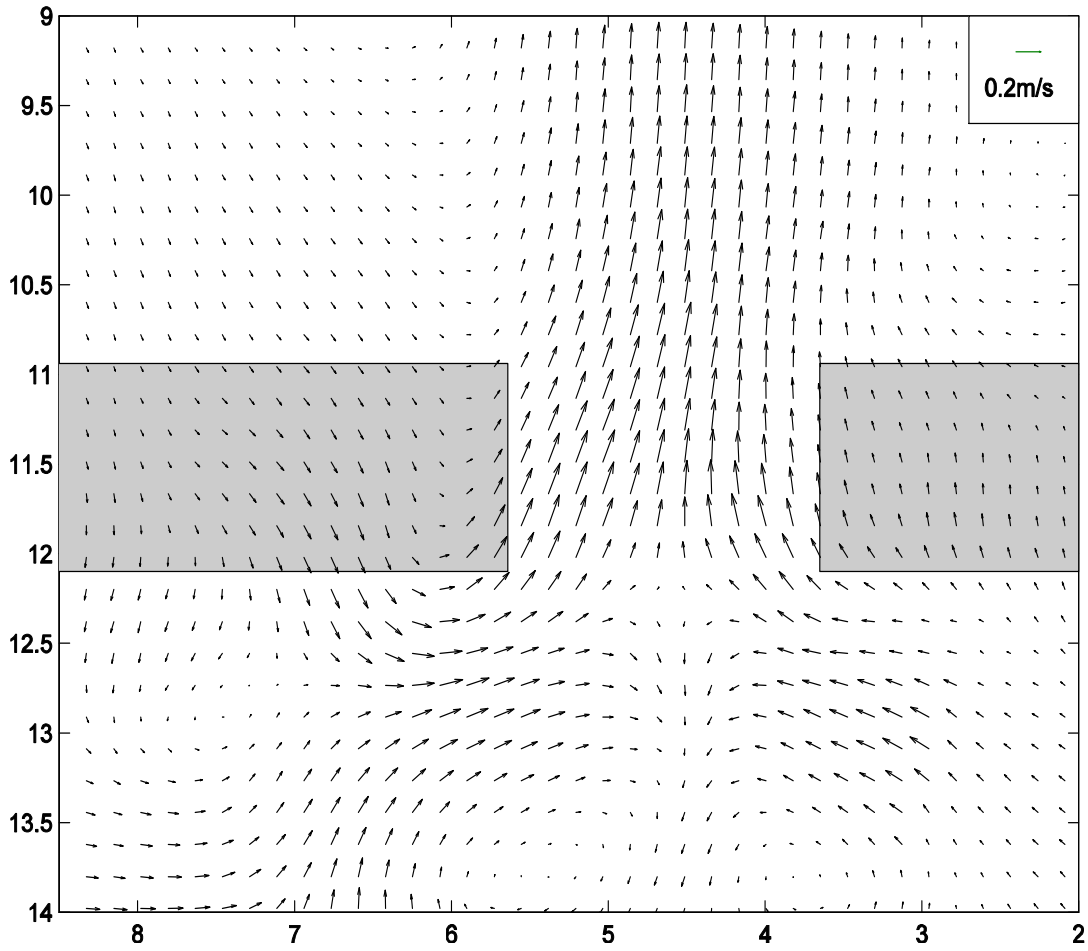

Figure 4.6: Twenty-minute time-averaged flow field for 1/3 incised rip channel topography under incoming wave height 0.03 m

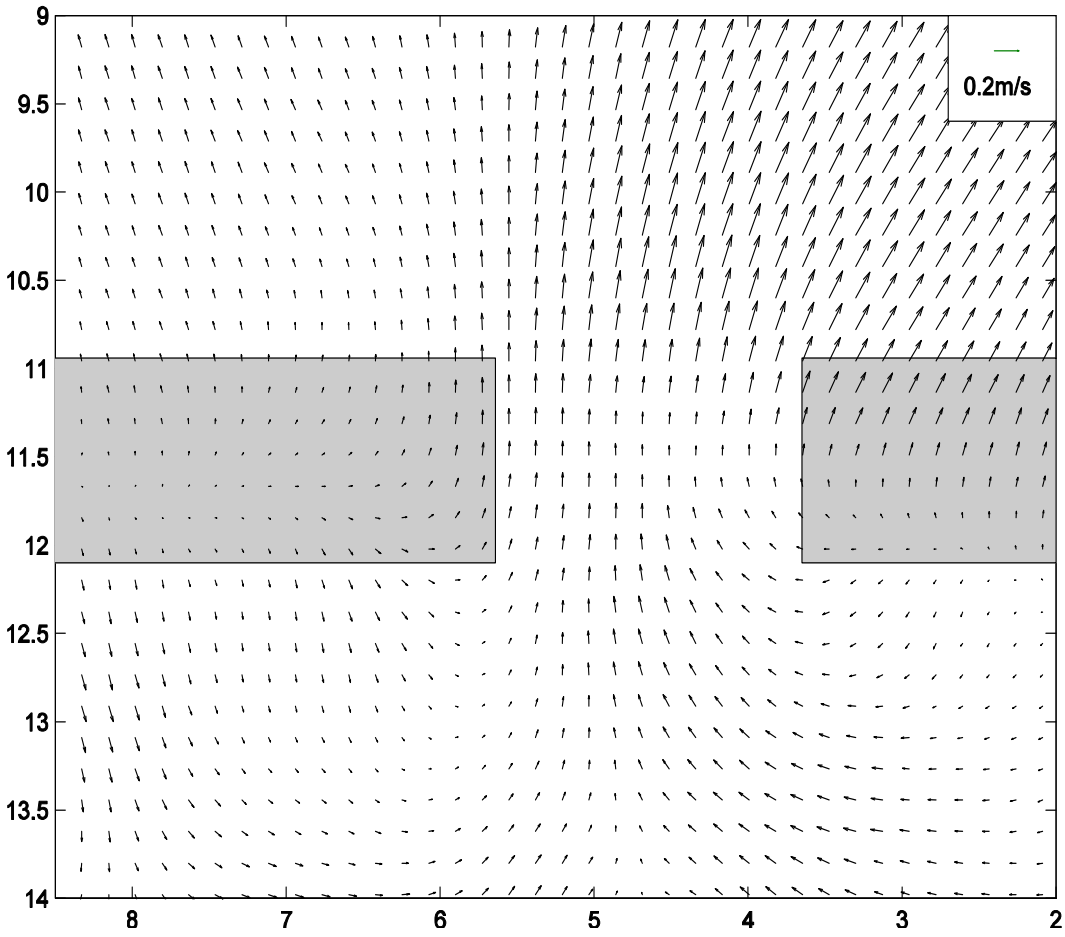

Figure 4.7: Twenty-minute time-averaged flow field for 1/3 incised rip channel topography under incoming wave height 0.05 m

4.4 Vorticity and Shear

Having spatially dense surface velocity fields rather than point-wise measurements allows the estimation of higher-level fluid motion descriptors such as the vorticity field and shear stress fields by taking the appropriate velocity gradients. The four panels in Figure 4.8 display the one-minute average vorticity field [1/2(dv/dx-du/dy)] starting at the 1st, 5th, 11th and 17th minute. From (a) to (d), gradually the rip current develops and circulation cells form on both sides of rip channel similar to the areas of rotation observed by Schmidt *et al.* [2003] in the field. Relatively constant vorticity magnitudes of greater than 0.3 s^{-1} are observed for this case. Positive and negative vortices show persistent shoreward motion over the bar near the channel being diverted into the channel to form the rip. It can be seen that the two major vortices maintain location, meaning that even though the rip head may occasionally oscillate from left to right, the feeder vortices are relatively stable.

Figure 4.9 shows the distribution of the one-minute averaged shear rate fields [1/2 (dv/dx+du/dy)] corresponding to the four panels in Figure 4.8. At the first minute, the rip current has not fully developed and the shear rate is small in magnitude. Similar to the vorticity map evolution, from (b) to (d), the locations of high shear rate remain relatively constant but experience variations in magnitude. The maximum observed lateral shear stress tend to occur near the edges of the rip channel and offshore and exceeds 0.1 s^{-1}. The fact that there is high shear observed offshore of the bar may indicate that shear and vorticity is generated within the channel and then advected offshore.

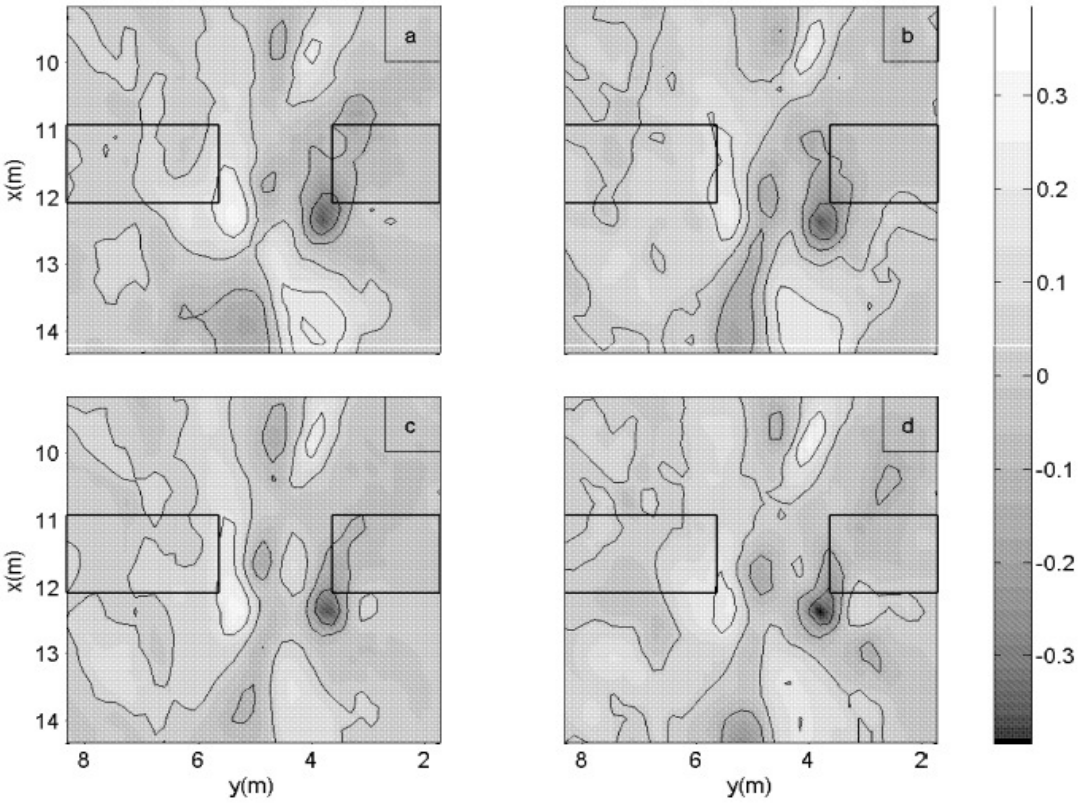

Figure 4.8: One-minute time-averaged vorticity (colorscale in s^{-1}) field starting at (a) 1st minute (b) 5th minute (c) 11th minute and (d) 17th minute after the onset of wave generation. Black boxes denote the location of 'sand' bar.

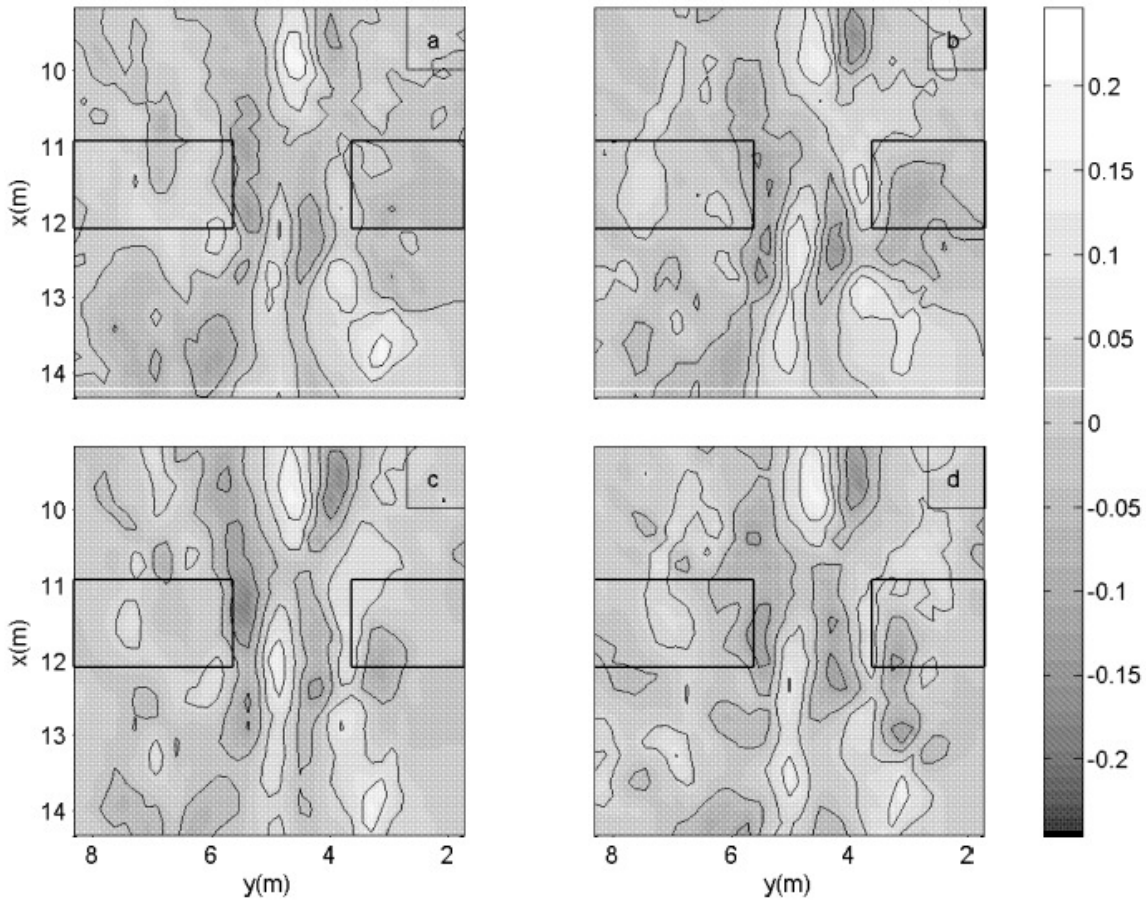

Figure 4.9: One-minute time-averaged shear rate field (colorscale in s^{-1}) starting at (a) at 1st minute (b) 5th minute (c) 11th minute and (d) 17th minute after the onset of wave generation. Black boxes denote the location of 'sand' bar

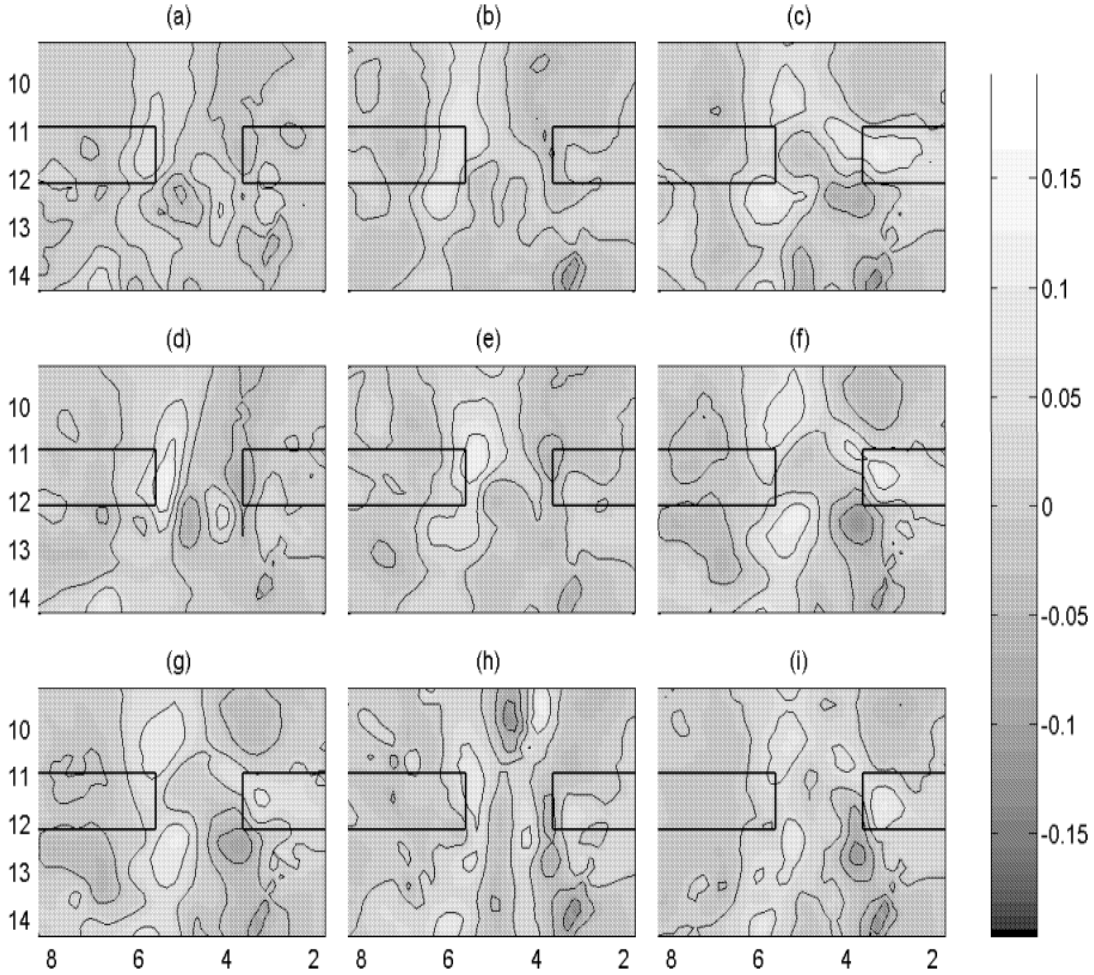

Figure 4.10: Twenty-minute time-averaged vorticity field for 9 cases, (a) 1/3 incised rip channel and 0.03 m wave height, (b) 1/3 incised rip channel and 0.05 m wave height, (c) 1/3 incised rip channel and 0.07 m wave height, (d) 2/3 incised rip channel and 0.03 m wave height, (e) 2/3 incised rip channel and 0.05 m wave height, (f) 2/3 incised rip channel and 0.07 m wave height, (g) fully incised rip channel and 0.03 m wave height, (h) fully incised rip channel and 0.05 m wave height, (i) fully incised rip channel and 0.07 m wave height.

Figure 4.10 shows the twenty-minute mean of the vorticity field as a function of incoming wave conditions and topographical circumstances. Horizontally the wave increases from 0.03 m, 0.05 m to 0.07 m and vertically the rip channel is incised from 1/3, 2/3 to fully. Compared with the one-minute averaged snapshot of vorticity field in figure 4.8, longer time-averaged vorticity has smaller mean value, in which most short-term rotation and counter-rotations are both averaged out. All have the major circulation ring around the rip channel and bar and some of them have apparent secondary rotations. The higher the incoming wave height, the stronger the driving force of rip formation, the larger and more intense major vorticity ring is observed. There is no obvious trend with respect to geometry, which may imply the effect of variable topography on the mean vorticity field is not significant.

4.5 Offshore Flow Within the Rip Channel

To better examine the offshore flow strength under different conditions, Figure 4.11 and Figure 4.12 respectively show the mean offshore velocity and maximum offshore velocity magnitude as the function of wave condition and rip incision. With the same color scale, we can see in Figure 4.11 most of the offshore average velocity is less then 0.2m/s in most cases, and not surprisingly, the increased wave height induces faster mean offshore flow within the channel. With respect to channel incision, the magnitude of the velocity does not seem to change significantly, only the shape of contour is slightly different indicating the variable distribution of offshore current strength. For 0.03 m waves, the mean rip current velocity magnitude roughly increases as the channel depth increases. In the case of the 0.05 m waves, the mean rip current velocity magnitude is fairly consistent but the gradient in cross-shore distribution of the velocity magnitude decreases with increasing channel depth. That is, for the fully incised channel, the large offshore-directed velocities are observed

throughout the cross-shore expanse of the channel and landward and seaward of it. In contrast, for the 1/3 incised channel, mean rip current velocity magnitudes are weak landward of the bar and increase in the offshore direction implying the rip current strength increases as it "shoots" through the channel. On all three topographies, as the incoming wave height increases from 0.03 m to 0.05 m, there is a global increase in the mean rip current velocity magnitude within the channel and offshore. However, when the wave height increases from 0.05 m to 0.07 m, there is a global decrease in rip strength. This phenomenon can be explained by the energy classification (Figure 4.5). While most of our experiment data falls in the intermediate energy rip current regime. Increasing the wave height within the rip channel creates a negative feed back on the system, because the radiation stress gradients develop a counter-torque that oppose the pressure gradients [MacMahan, *et al.*, 2005]

Because the rip head is known to meander back and forth, calculating the mean will average out the oscillations and possibly obscure the true effect of altering the channel incision depth. Thus, maximum offshore-directed currents were also calculated (Figure 4.12). Rather than picking the single maximum value from each time series, we choose a surrogate based on the offshore-directed velocity that is the average of the top 5% in the time series. We refer to this value as the maximum. Perhaps not surprisingly, maximum offshore flow velocities increase when the wave height increases from 0.03 m to 0.05 m for all channel geometries. As the channel depth increases from 1/3 to 2/3 a global increase in the maximum rip current velocity is observed for the 0.03 m waves. However, at this wave height the maximum rip current velocity appears to decrease as the channel is further deepened to full incision. In contrast, the maximum rip current velocities magnitudes are more uniformly high

(~0.6 m/s) for the 0.05 m waves regardless of channel depth. Again, we do observe a stronger cross-shore gradient in maximum rip current velocity for the 1/3 channel incision that is less distinct in the fully incised case for the 0.05 m waves. And on all three topographies, there is no apparent global increase or decrease if the wave height increases from 0.05 m to 0.07 m, the maximum rip currents just suggest how fast the rip currents can be.

To more rigorously investigate the variability for the nine cases, two locations, with one in the channel and the other offshore of the channel, are extracted from the rip channel for single point analysis. In most of the cases, the location offshore of the rip channel experience stronger offshore flow than the location within the center of rip channel, which corresponds to what is seen in Figure 4.11. Depending on location within the rip current, the mean surface rip current velocity magnitude could increase or remain roughly the same when the channel depth increases from 1/3 to 2/3. When the channel depth increases from 2/3 to full incision, the mean surface rip current velocity can either increase or decrease.

Maximum offshore velocities also show the variation in magnitude of the rip current at these two locations. The maximum current velocities exhibit basically the same trend as the mean velocities in that as channel depth is incised from 1/3 to 2/3, stronger offshore flow is generated. As the channel depth increases from 2/3 to full incision, the offshore flow decreases in its strength. This inconsistent trend could possibly be explained by combining the effect of forcing mechanisms and continuity argument. Previous measurements have demonstrated that there is an approximately linear relationship between the incident wave field and wave forcing and also between wave forcing and rip current strength [Aagaard, *et al.*, 1997]. So in our study, as the

wave height increases from 0.03 m to 0.05 m, there is a global stronger offshore current. While the incoming wave height plays the major role in driving the return flow, the alongshore gradient of bathymetry is also important. Additionally, the strength of rip within the channel is subjected to the wave-current interaction. Holding the incoming wave constant, hypothetically, as the rip channel is incised from 1/3 to 2/3, a larger alongshore gradient in bathymetry will cause a greater alongshore gradient in setup due to variations in wave breaking, and in turn induces a stronger offshore flow. However, as the channel is further incised, two concepts may explain the slower offshore-directed current. One is the continuity argument. The deeper rip channel incision is equivalent to a lager area of cross-section through which roughly the same amount of water is forced within a unit time. Consequently, increasing the cross-section of the outlet may induce weaker offshore flow. The other factor is the wave-current interaction effect, in which the incoming breaking wave interacts with the rip current possibly retarding offshore-directed flow motion.

In Figure 4.13, we compare the flow fields by subtracting the mean flow field from conditions with the same wave height but full channel incision. For example, Figure 4.13 (a) is the 0.03 m wave and 1/3 rip incision flow field subtracted from the flow field corresponding to 0.03 m wave and full rip incision. It is obvious that in most cases there is a positive area in the nearshore region. Consider the negative value if the currents are heading offshore, a positive sign here means a smaller offshore current in magnitude. It suggests, compared with fully incised rip current, the 1/3 and 2/3 incised rip have weaker offshore current in a small nearshore region of the rip channel and for the most area within the rip channel, the partially incised channel experience bigger offshore flow compared to the fully incised channel.

To further enhance our comprehension of the rip current dynamics within and out of the rip channel. Two cross-shore lines (shown in Figure 4.14) are chosen with one being within the rip channel and the other going across the alongshore bar. Figure 4.15 shows the time-averaged cross-shore velocity for the channel centerline on three different topographies. Generally, with one incoming wave height, the three rip current lines corresponding to three different topographies are intertwined most of the time. In the area onshore of the rip channel, the fully incised rip channel has larger offshore currents than the one in 1/3 topography. It is also noticeable, there is a junction of the three lines and the trend will change in the offshore portion of the rip channel. Then as the rip current heads offshore, 1/3 and 2/3 rip channel cases exhibit the greatest offshore current in turn. In Figure 4.16, in the case of 0.03 m wave height, there is an almost persistent trend that when topography changes from 1/3 rip channel to 2/3 m, there is a stronger offshore flow and then the flow decreases when the rip channel is further incised to full channel. In the case of 0.05 m wave height, offshore flow with a fully incised rip channel maintains a constant velocity (~0.6 m/s) all way through out the rip channel, while the other two rip currents increase their strength as they shoot offshore. With 0.07 m waves, the three rips have the offshore flow of almost the same magnitude. Particularly in Figure 4.17, in the 0.07 m wave height scenario, an obvious trend is present that 1/3 rip incision topography has the strongest offshore flow.

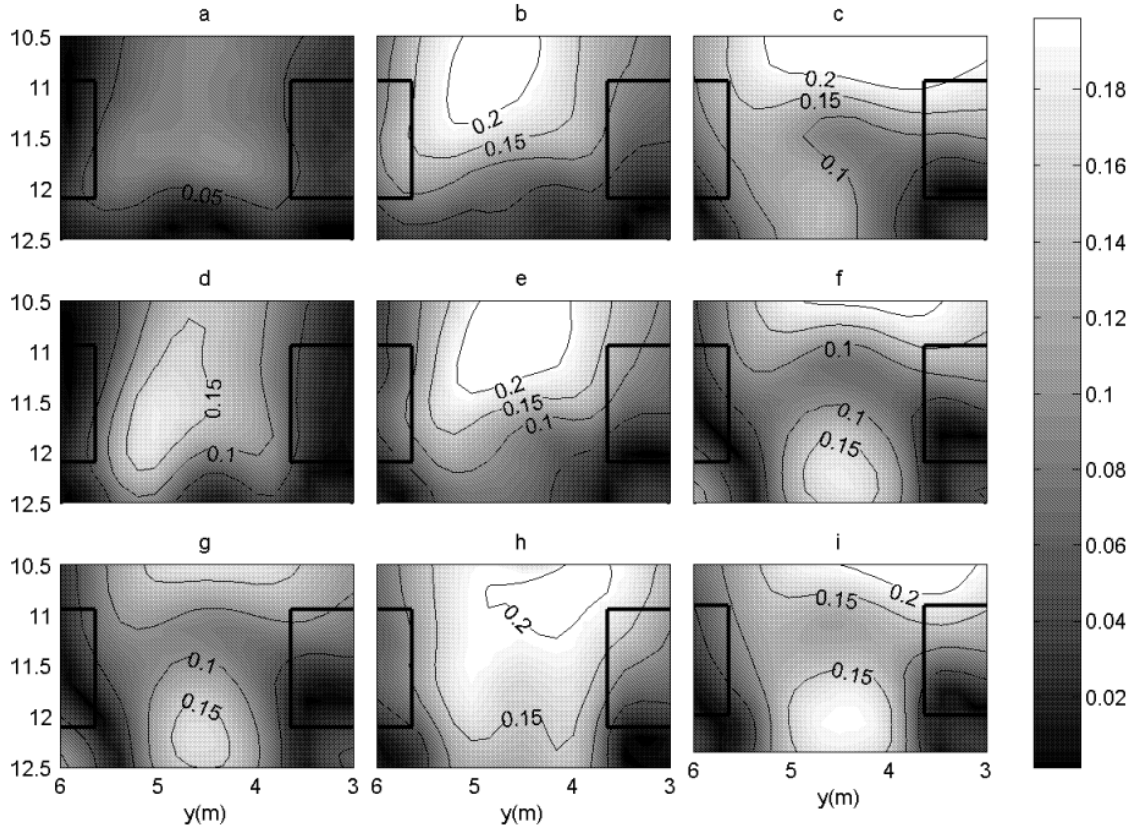

Figure 4.11: Twenty-minute mean offshore velocity magnitude field within the channel for 9 cases, (a) 1/3 incised rip channel and 0.03 m wave height, (b) 1/3 incised rip channel and 0.05 m wave height, (c) 1/3 incised rip channel and 0.07 m wave height, (d) 2/3 incised rip channel and 0.03 m wave height, (e) 2/3 incised rip channel and 0.05 m wave height, (f) 2/3 incised rip channel and 0.07 m wave height, (g) fully incised rip channel and 0.03 m wave height, (h) fully incised rip channel and 0.05 m wave height, (i) fully incised rip channel and 0.07 m wave height. The black square denotes the edge of the bar.

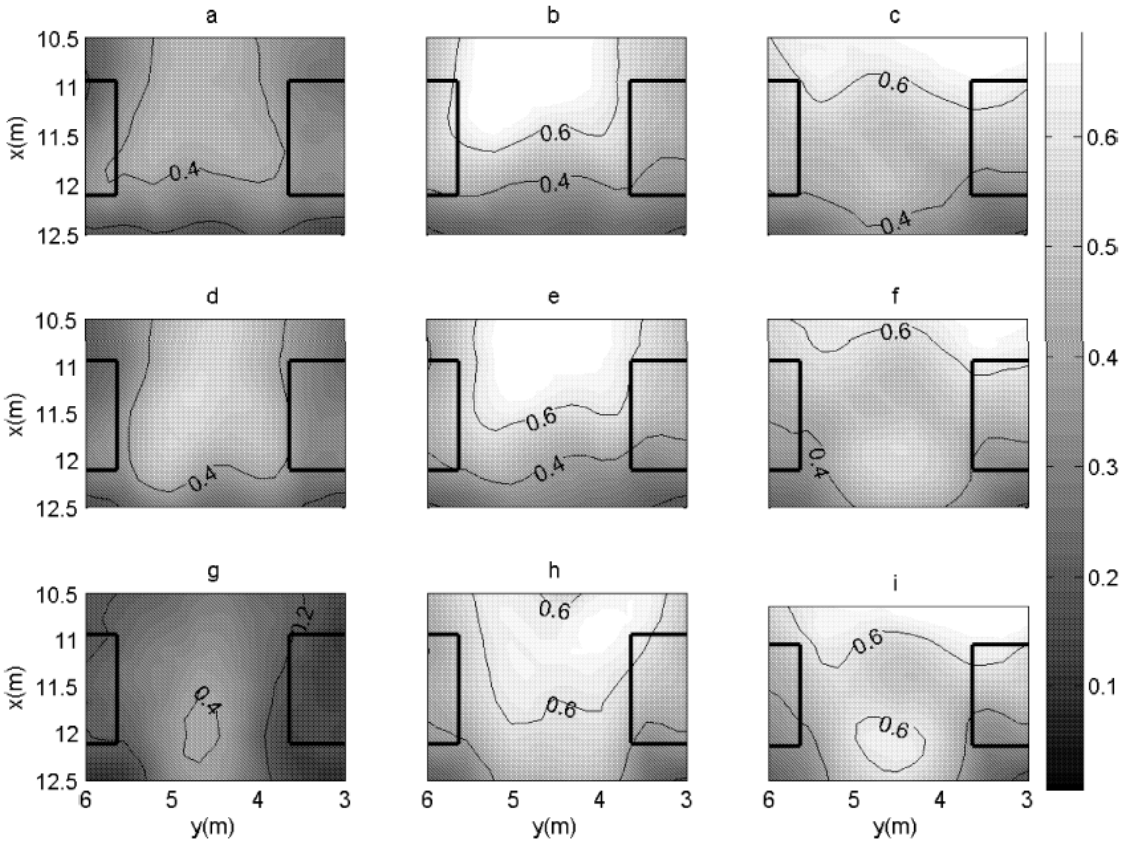

Figure 4.12: The maximum offshore velocity magnitude field within the channel for 9 cases, (a) 1/3 incised rip channel and 0.03 m wave height, (b) 1/3 incised rip channel and 0.05 m wave height, (c) 1/3 incised rip channel and 0.07 m wave height, (d) 2/3 incised rip channel and 0.03 m wave height, (e) 2/3 incised rip channel and 0.05 m wave height, (f) 2/3 incised rip channel and 0.07 m wave height, (g) fully incised rip channel and 0.03 m wave height, (h) fully incised rip channel and 0.05 m wave height, (i) fully incised rip channel and 0.07 m wave height. The black square denotes the edge of the bar.

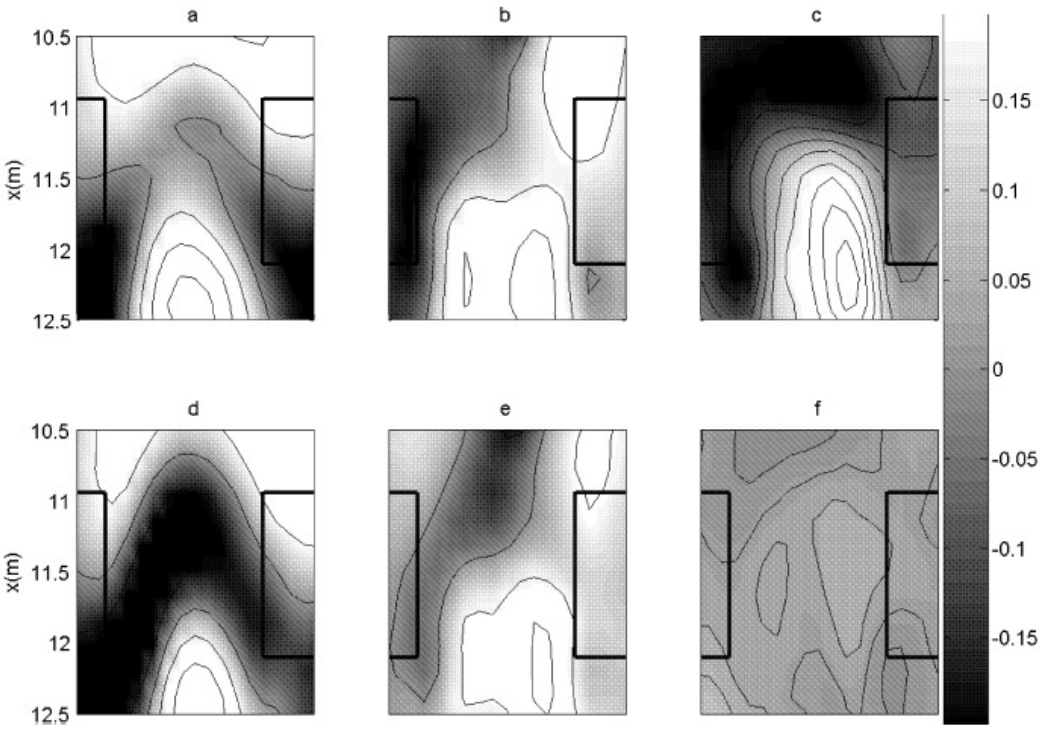

Figure 4.13: Twenty-minute time-averaged flow field subtracted by the fully incised flow field. (a) 1/3 incised rip channel and 0.03 m wave subtracted by 0.03 m but fully incision flow field, (b) 1/3 incised rip channel and 0.05 m wave subtracted by 0.05 m but fully incision flow field, (c) 1/3 incised rip channel and 0.07 m wave height subtracted by 0.07 m but fully incision flow field, (d) 2/3 incised rip channel and 0.03 m wave height subtracted by 0.03 m but fully incision flow field, (e) 2/3 incised rip channel and 0.05 m wave height subtracted by 0.05 m but fully incision flow field, (f) 2/3 incised rip channel and 0.07 m wave height subtracted by 0.07 m but fully incision flow field.

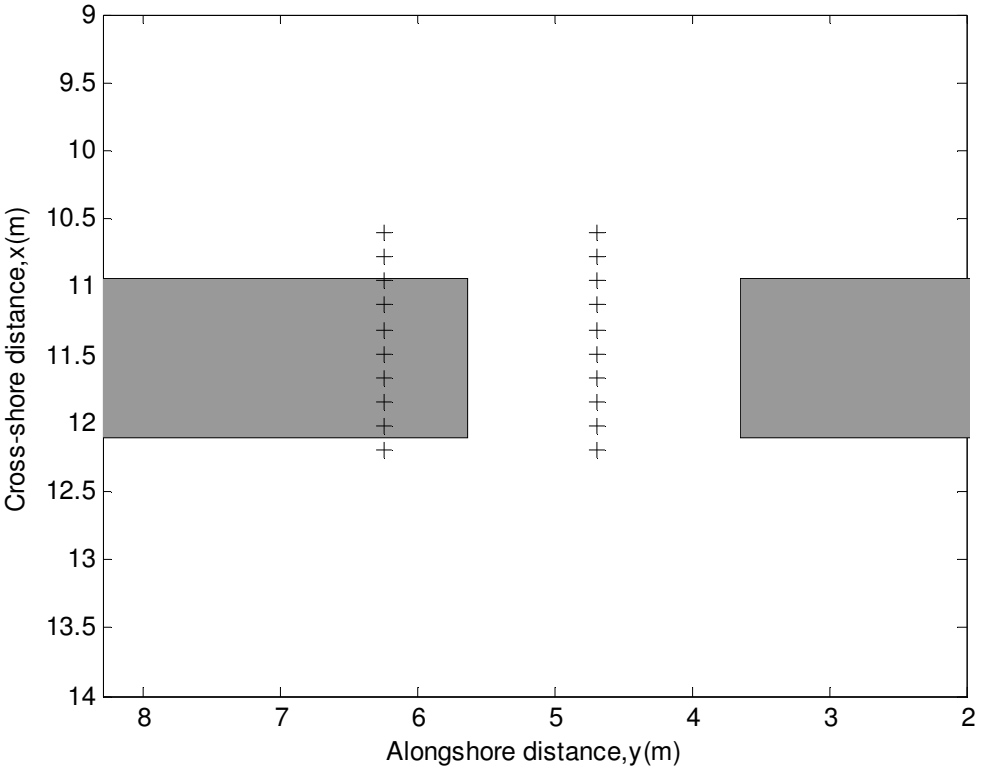

Figure 4.14: Demonstration of the two cross-shore line within the channel and over the bar, which were taken to analyze the rip current variability.

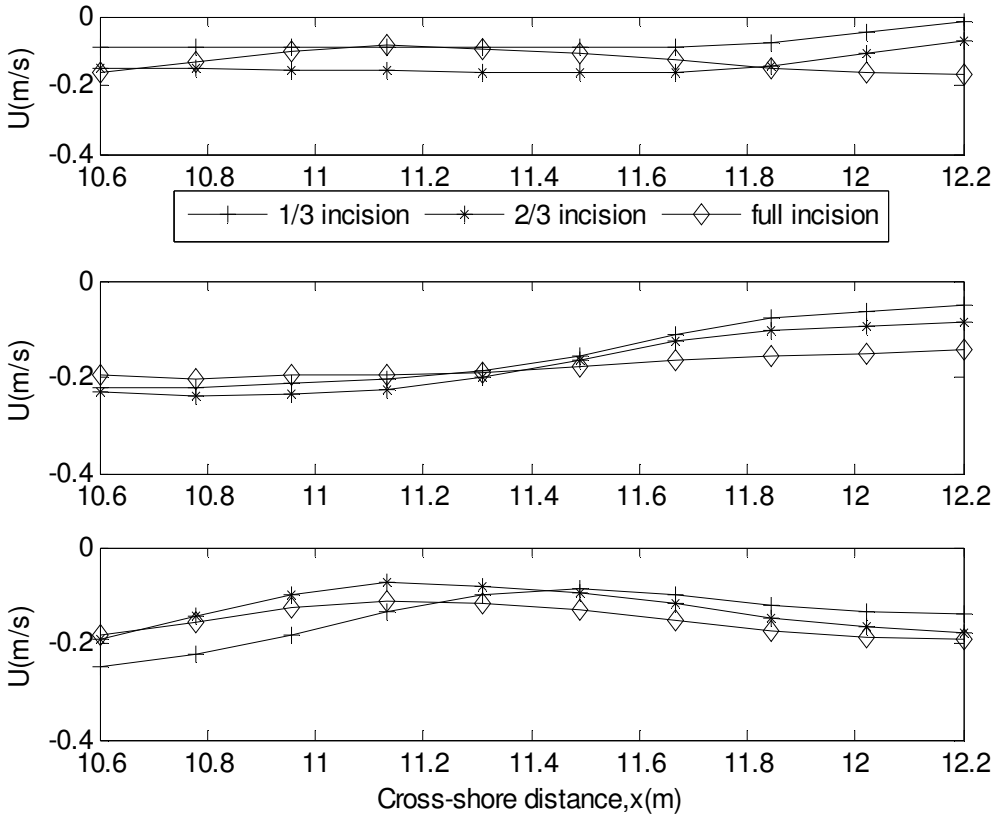

Figure 4.15: The time-averaged cross-shore velocity for the channel centerline on three different topographies. The upper panel is for 0.03 m wave height, middle is for 0.05 m wave and the lower is for 0.07 m wave.

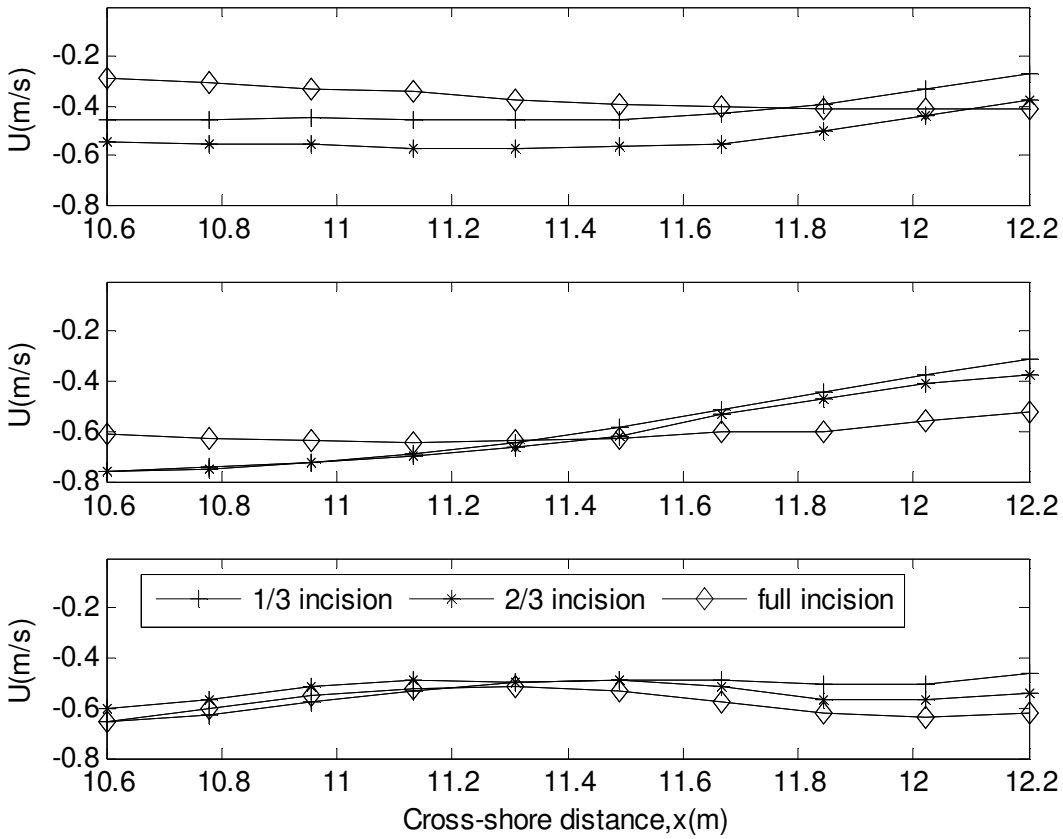

Figure 4.16: The mean of the maximum 5% offshore velocity for the channel centerline on three different topographies. The upper panel is for 0.03 m wave height, middle is for 0.05 m wave and the lower is for 0.07 m wave

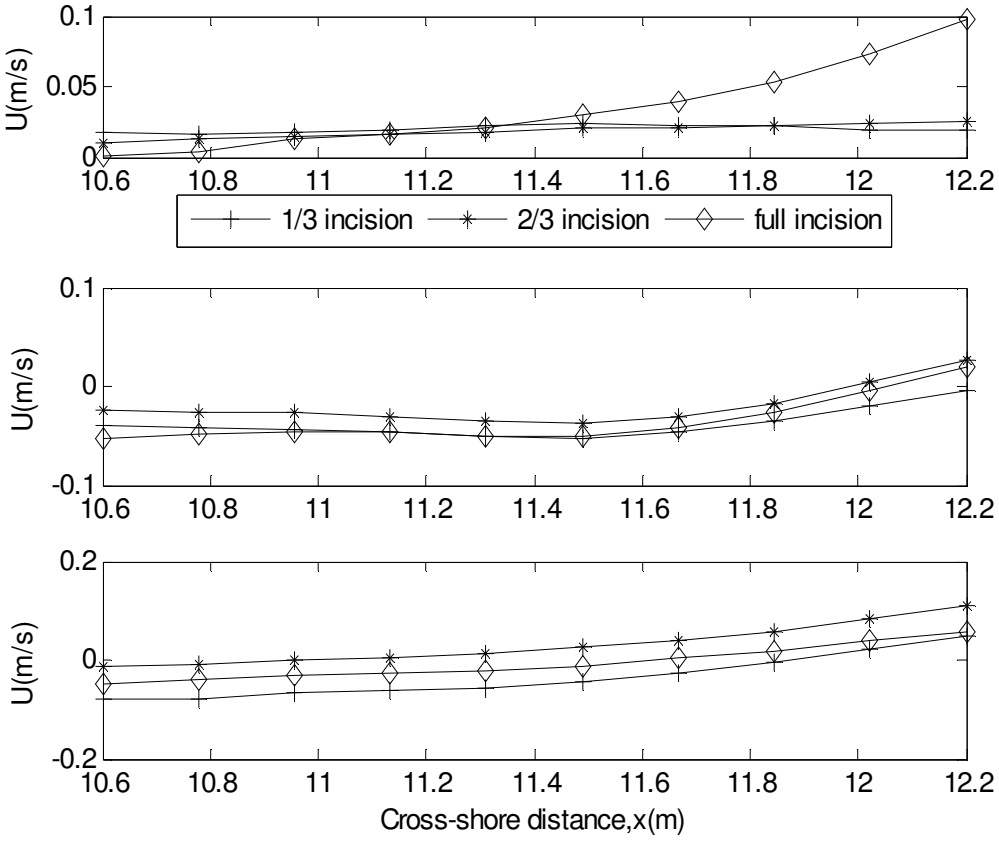

Figure 4.17: The time-averaged cross-shore velocity for the over bar line on three different topography. The upper panel is for 3 cm wave height, middle is for 5 cm wave and the lower is for 0.07 m wave

4.6 ADV Measurement

In chapter 3 for PIV measurement validation, three-dimensional side-looking Acoustic Doppler Velocimeters (ADVs) were installed under the trough level to verify the surface measurement. All the comparisons were performed for a single horizontal location but at different elevations. In order to investigate the topographical effect not only on the surface flow pattern but also the sub-surface velocity, 8 locations are selected around the channel and the bar and the ADV is installed onto a wooden frame, which is easy to move after measurement at each location (shown in figure 4.12). The mounting system is designed to insure the probes of ADV are always under the free surface. Three twenty-minute recordings of velocity were made corresponding to the three wave heights at each location for each topography. Each time the topography is changed and rebuilt, the 72 measurements are repeated. Initially, we also intended to obtain the ADV measurement over the crest of the bars at locations 4 and 6 (not shown), however the shallow water sheet over the bar does not allow a reliable ADV measurement. In Figure 4.18, the 9 mean velocities at the designated 8 grid points are shown, approximately all the vectors are suggesting the local flow orientation of a typical rip current. To obtain a better comparison of different scenarios, the mean and standard deviation of the cross-shore velocity is shown in table 4.1, it can be seen, except the grids within rip channel (5 and 10), other grid points have nearly zero mean in cross-shore velocity component even the standard deviation suggest a big oscillation. Grids 5 and 10 have negative average, indicating an offshore current. There is a persistent increase while increasing the incoming wave height. Different from what we saw from PIV surface flow measurement, the sub-surface flow tends to be faster when rip channel is incised deeper. This phenomenon suggests a

potential vertical variance of flow structure within the rip channel, however, limited by our measurement data with ADV, we are not able to resolve a whole-flow field and three-dimensional rip current structure.

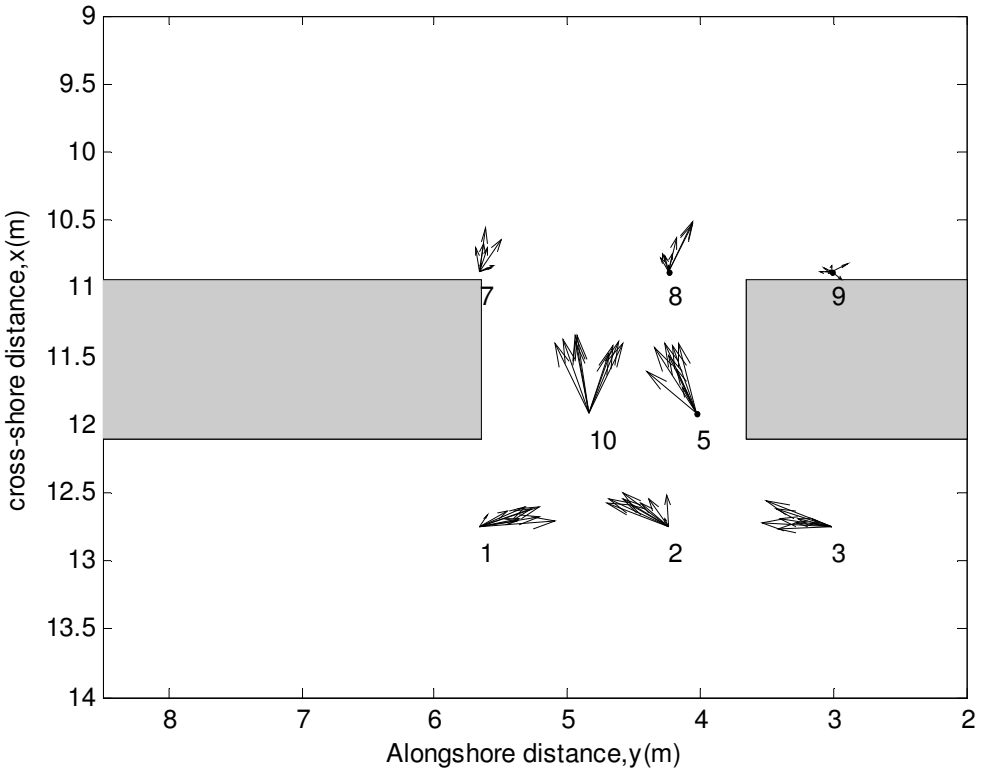

Figure 4.18: The location of ADV installation and the averaged measurement for 9 cases for the 8 locations

Table 4.1: Mean cross-shore velocity and standard deviation from ADV measurement at 8 different locations

Location **1**	1/3 incision	2/3 incision	3/3 incision
0.03 m wave	-0.01±0.05	-0.01±0.04	-0.01±0.06
0.05 m wave	-0.02±0.04	-0.02±0.03	-0.04±0.04
0.07 m wave	-0.01 ±0.04	-0.03±0.04	-0.0437±0.04
Location **2**			
0.03 m wave	-0.01±0.04	-0.03±0.06	-0.04±0.05
0.05 m wave	-0.04±0.04	-0.04±0.04	-0.05±0.05
0.07 m wave	-0.04±0.04	-0.05±0.04	-0.08±0.06
Location **3**			
0.03 m wave	-0.01± 0.04	-0.00±0.03	-0.04±0.04
0.05 m wave	-0.00± 0.04	-0.01±0.04	-0.04±0.05
0.07 m wave	0.00 ±0.04	-0.01±0.06	-0.02±0.05
Location **5**			
0.03 m wave	-0.03±0.09	-0.08±0.07	-0.06-±0.07
0.05 m wave	-0.06±0.09	-0.09±0.06	-0.14±0.08
0.07 m wave	-0.10±0.06	-0.12±0.04	N/A
Location **7**			
0.03 m wave	-0.00±0.04	-0.01±0.04	-0.00±0.05
0.05 m wave	-0.04±0.08	-0.04±0.07	-0.02±0.10
0.07 m wave	-0.06±0.10	-0.05±0.09	-0.05±0.11
Location **8**			
0.03 m wave	-0.02±0.08	-0.2±0.04	-0.01±0.05
0.05 m wave	-0.02±0.08	-0.02±0.07	-0.10±0.12
0.07 m wave	-0.06±0.10	-0.06±0.10	N/A
Location **9**			
0.03 m wave	-0.00±0.05	0.00±0.04	0.01±0.06
0.05 m wave	0.00±0.07	-0.00±0.08	0.00±0.08
0.07 m wave	-0.01±0.10	-0.01±0.09	-0.00±0.10
Location **10**			
0.03 m wave	-0.08±0.07	-0.08±0.06	-0.10±0.08
0.05 m wave	-0.09±0.08	-0.11±0.05	-0.12±0.07
0.07 m wave	-0.10±0.06	-0.13±0.04	-0.16±0.05

Chapter 5

CONCLUSION

5.1 Conclusion

The purpose of this study is to apply a Particle Image Velocimetry (PIV) technique to laboratory generated rip currents and then investigate the variability of the surface flow field structure corresponding to different wave condition and different bottom topography.

Firstly, various time domain and frequency domain based PIV algorithms are computed and compared in terms of computation efficiency and noise response. Conventional cross-correlation algorithms are robust to noise while the FFT based ones are computationally efficient. A multi-grid iterative FFT scheme is chosen as the interrogating algorithm in our study. The cross-correlation peak selection principle, weighting function and sub-pixel interpolation are introduced to optimize the performance of PIV. A post-processing technique identifies the vectors significantly different from the surrounding flow field in either magnitude or direction and substitutes them with dynamic mean. Synthetic images mimicking the processed flow field pictures are created and then used to test the effect of post-processing procedure following Holland *et al.* [2001]. This post-processing procedure causes the normalized RMS error to decrease by 17 % (0.46 to 0.38).

Before the images are fed into our developed PIV processing program, lens calibration, image rectification and a series of image pre-processing needs to be

conducted. A direct linear transformation (DLT) method is employed for the estimation of distortion coefficients and dots pattern is used in this case to account for the radial distortion. The lens edge distortion is removed for each image taken before any other processing.

As all the experiments are conducted in a laboratory environment, marking and surveying the Ground Control Points (GCPs) is not a major undertaking. Following the rectification procedure of Holland *et al.* [1997], seven GCPs, whose real-world coordinates are known from previous surveys and the two-dimensional image coordinate can be determined, are chosen to close the equation system and help to complete a two-dimension to three-dimension transformation of the acquired images. In our study, we prefer to convert the image to a flow field projected to the still water level, which means a final surface velocity measurement at the still water level.

Rectified images may have poor signal to noise ratio until they are preprocessed. Several steps are taken for the purpose of emphasizing the seeding material and reducing the background noise. Median filter, high-pass filter and binarization are all applied to accentuate the effect.

All the rip current simulating experiments are set up in the directional wave basin located in University of Delaware. With several pilot and similar experiments performed here. Parameters such as shoreline position and incoming wave height can be followed and also compared. As PIV is for the first to be applied to our laboratory images processing, repeatability test and instrument measurement validation are performed to ensure the PIV is valid in resolving the surface flow field with

considerable reliability and accuracy. The alongshore and cross-shore velocity returned compares favorably with the ADV measurement sampled at the same location.

The basin topography is constructed for three rip channel incisions, naming the previous rip channel as fully incised channel, we also use 1/3 and 2/3 incised rip channels. For each basin geometry set up, 0.03 m, 0.05 m and 0.07 m wave heights are generated representing different levels of wave forcing. Taking advantage of PIV's dense measurement property, vorticity and shear rate fields are shown at different stage of the rip current evolution.

Variability of rips corresponding to variable wave condition and basin geometry is investigated. Spatial distribution and single location analysis of offshore flow strength indicate that the as the wave height increases from 0.03 to 0.05 m, a global strengthening of offshore surface flow occurs. As the wave height further increases to 0.07 m, the offshore flow does not have a significant increase. Additionally, as the rip channel deepens from 1/3 to 2/3 to fully incised, the strength of the offshore surface current will increase at first and then decrease to some extent. The above trends are partly explained in our study in combination of the wave forcing, continuity standpoint and wave-current interaction.

5.2 Suggestions for Future Work

To obtain a more comprehensive perspective toward the variability of rip current under different wave condition and basin geometry, more subsurface velocity measurements are necessary. It also would be beneficial if the rip channel incision can be made subtler yielding bathymetry even more similar to the natural beach scenario.

BIBLIOGRAPHY

Aagaard, T., B. Greenwood, and J. Nielsen, (1997). Mean currents and sediment transport in a rip channel, *Mar. Geol.*, 140,25-45

Abdel-Aziz, Y.I. and Karara, H.M., (1971). Direct linear transformation from comparator coordinates into object space coordinates in close-range photogrammetry. *Proceedings of the Symposium on Close-Range Photogrammetry,* Falls Church, VA: American Society of Photogrammetry. 1-18

Adrian, R.J., (1991). Particle-Imaging Techniques for Experimental Fluid Mechanics, *Annual Reviews of Fluid Mech.*, 23:261-304

Adrian, R.J., (2005). Twenty years of particle image velocimetry, *Exp. Fluids*, 39: 159-169

Bowen, A.J., (1969). Rip Currents, 2, Laboratory and field observations, *J. Geophys. Res.*, 74, 5479-5490

Bowman, D., D. Arad, D.S. Rosen, E. Kit, R. Golbery, and A. Slavicz, (1988) Flow characteristics along the rip current system under low-enrgy conditions, *Mar. Geol.*, 82,149-167

Brander, R.W., (1999). Field observations on the morphodynamic evolution of low wave energy rip current system, *Mar. Geol.*, 157,199-217

Brander, R.W., and A. D. Short, (2000). Morphodynamics of a large-scale rip current system at Muriwai Beach, New Zealand, *Mar. Geol*., 165,27-39

Calllaghan, D.P., T.E. Baldock, P. Nielsen, D. M. Hanes, K. Hass and J.H. MacMahan, (2004), Pulsing and circulation in a rip current system, *Proc. of the 29th International Conf. on Coastal Eng.*, Am. Soc. Of Civ. Eng., Portugal.

Chen, Q., R.A. Dalrymple, J.T. Kirby, A.B. Kenedy and M.C. Haller, (1999). Boussinesq modeling of a rip current system, *J. Geophys. Res.*, 104, 20617-20637

Dronen, N., H. Karunarathna, J. Fredsoe, B.M. Sumer, and R. Deigaard, (2002). An experimental study of rip channel flow, *Coastal Eng*., 45(3-4), 223-238

Fujita, I., Kaizu, T., (1995). Correlation method of erroneous vectors in PIV, *J. Flow Visualization Image Processing,* 2(2),173-185

Grant, I. and X. Pan, (1997). The use of neural techniques in PIV and PTV, *Meas. Sci. Technol.*, 8

Hart, D.P., (1999) Super-Resolution PIV by Recursive Local-Correlation, *J. Visual.,* Vol. 10

Haas, K.A. and I.A. Svendsen, (2000). Three-dimensional modeling of rip current system, *Res. Rep.*, CACR-00-06, Cent. for Appl. Coastal Res., Univ. of Del., Newark

Haas, K.A. and I.A. Svendsen, (2002). Laboratory measurements of the vertical structure of rip currents, *J. Geophys. Res.*, VOL. 107, No. C5

Haas, K.A., I.A. Svendsen and Q. Zhao, (2003). Quasi-three-dimensional modeling of rip current systems, *J. Geophys. Res.*, VOL. 108, No. C7

Haller, M.C., R.A. Darymple and I.A. Svendsen, (2002). Experimental Study of Nearshore Dynamics on a Bared Beach with Rip Channels, *J. Geophys. Res.*, VOL. 107, No. C6

Haller, M.C. and R.A. Darymple, (2001). Rip current instabilities, *J. Fluid Mech*., VOL. 433, 161-192

Hamm,L.(1992). Directional nearshore wave propagation overa rip channel: an experiment, *Proc. 23rd Coastal Eng. Conf.*, ASCE, 1:226-239, Venice

Holland, K.T., J.A. Puleo and T.N. Kooney, (2001). Quantification of swash flows using video-based particle image velocimetry, *Coastal Eng*., 44, 65-77

Holland, K.T., R.A. Holman and T.C. Lippmann, (1997). Practical Use of Video Imagery in Nearshore Oceanographic Field Studies, *J. Oceanic Eng.*, VOL. 22, No.1

Kennedy, A.B. and D. Thomas, (2004). Drifter measurement in a laboratory rip current, *J. Geophys. Res.*, VOL. 109

Kennedy, A.B. and R.A. Dalrymple, (2001). Wave Group Forcing of Rip Currents, *Proc. Waves 2001*, ASCE, San Francisco

Lawson, N.J. and J. Wu, (1997). Three-dimensional particle image velocimetry: error analysis of stereoscopic techniques, *Meas. Sci. Technol.,* 8, 894-900

Lenz, R.K. and R. Y. Tsai, (1988). Techniques for calibration of scale factor and image center for high accuracy 3-d machine vision metrology, *IEEE Tans. Pattern Anal. Machine Intell.*, VOL. 10, pp. 713-720

McKenzie, P. (1958). Rip-current systems, *J. Geol.*, 66,103-113

MacMahan, J., A.J.H.M. Reniers, E.B. Thornton and T. Stanton, (2004). Surf zone eddies coupled with rip current morphology, *J. Geophys. Res.*, VOL. 109

MacMahan, J., A.J.H.M. Reniers, E.B. Thornton and T. Stanton, (2004). Infragravity rip current pulsations, *J. Geophys. Res*., 109, C01033, doi:10.1029/2003JC002068

MacMahan, J.H., E.B. Thornton and A.J.H.M. Reniers, (2005). Rip current review, Preprint submitted to Elsevier Science

Melling A., (1997). Tracer particles and seeding for particle image velocimetry*, Meas. Sci. Technol.*, 8., 1406-1416

Noda, E.K., (1974). Wave induced nearshore circulation, *J. Geophys. Res*., 79, 4097-4106

Nogueira, J., A. Lecuona, U. Ruiz-Rivas, P.A. Rodriguez, (2002). Analysis and alternatives in two-dimensional multigrid particle image velocimetry methods: application of a dedicated weighting function and symmetric direct correlation, *Meas. Sci. Technol.*, 13, 963-974

Prasad, A.K., (2000). Particle image velocimetry, *Current Sci.*, VOL. 79, No.1

Puleo, J.A., G. Farquharson, S.J. Frasier and K.T. Holland, (2003). Comparison of optical and radar measurements of surf and swash zone velocity fields*, J. Geophys. Res.*,VOL. 108, No. C3

Raffel, M., C. E. Willer, J. Kompenhaus, (1998). Particle Image Velocimetry: A practical Guide, *Springer*, New York, 253 pp.

Roth, G., D. Hart, J. Katz, (1995). Feasibility of using the L64720 video motion estimation processor to increase efficiency of velocity map generation for particle image velocimetry (PIV). *Fluids Eng. And Laser Anemometry Conf.*, ASME, pp 387-393

Scarano, F. and M.L. Riethmuller, (1999). Iterative multigrid approach in PIV image processing with discrete window offset, *Exp. Fluids*, 26, 513-523

Scarano, F., (2002). Iterative image deformation methods in PIV, *Meas. Sci. Technol.*, 13, R1-19

Schmidt, W.E., B.T. Woodward, K.S. Millikan, R.T. Guza, B. Raubenheimer and E. Elgar, (2003). A GPS-Tracked surf zone drifter, *J. Atmos. Oceanic Technol.*, VOL. 20, No. 7

Shepard, F.P., (1936). Undertow, rip tides, or "rip current", *Science*, 84

Shepard, F.P. and D.L. Inman., (1950). Nearshore circulation. *Proceedings of the 1st Conference on Coastal Engineering*, Council on Wave Research, Berkeley, CA., pp 50-59

Slinn, D.N., J.S. Allen and R.A. Holman, (2000). Alongshore currents over variable beach topography, *J. Geophys. Res.*, VOL. 105, No. C7

Stevens, C. and M. Coates, (1994). Application of a maximized cross-correlation technique for resolving velocity fields in laboratory experiments, *J. Hydraulic Res.*, VOL. 32, No.2

Sturm, P.F. and S.J. Maybank, (1999). On plane based camera calibration: A general algorithm, singularities and applications. In Proceedings of the *Conf. on Computer Vision and Pattern Recognition*, pp. 432-437

Weitbrecht, V., G. Kuhn and G.H. Jirka, (2002). Large scale PIV-measurements at the surface of shallow water flows, *Flow Mea. Instru*., 13, 237-245

Willert, C.E. and M. Gharib, (1991). Digital particle image velocimetry, *Exp. Fluids*, 10,181-193

Willson, R. G. and S. A. Shafter, (1994). What is the center of the image, *J. opt. Soc. Amer.*, vol. 11, pp. 2946-2955,1994

Yu, J. and D.N. Slinn, (2003). Effects of wave-current interaction on rip currents, *J. Geophys. Res.*, 108, C3, 3088, doi:10.1029/2001JC001105.